UNIVERSITY OF KWAZULU-NATAL ™

INYUVESI YAKWAZULU-NATALI

CHARACTERIZATION AND DEVELOPMENT OF OPTICAL COMPONENTS FOR THE CASSEGRAIN TELESCOPE AND LASER BEAM COUDÉ PATH OF THE LUNAR LASER RANGER OF HARTRAO

Nokwazi P. Nkosi

2015

CHARACTERIZATION AND DEVELOPMENT OF OPTICAL COMPONENTS FOR THE CASSEGRAIN TELESCOPE AND LASER BEAM COUDÉ PATH OF THE LUNAR LASER RANGER OF HARTRAO

by

Nokwazi P. Nkosi

Submitted in partial fulfilment of the requirements for the degree

MASTER OF SCIENCE IN LAND SURVEYING

In the College of Agriculture, Engineering and Science

University of KwaZulu-Natal, Durban

South Africa

2015

Under the supervision of

Supervisor: Prof Ludwig Combrinck Co-supervisor: Dr Mulemwa Akombelwa

COLLEGE OF AGRICULTURE, ENGINEERING AND SCIENCE

DECLARATION 1 - PLAGIARISM

I, …….……., declare that

1. The research reported in this thesis, except where otherwise indicated, is my original research.
2. This thesis has not been submitted for any degree or examination at any other university.
3. This thesis does not contain other persons' data, pictures, graphs or other information, unless specifically acknowledged as being sourced from other persons.
4. This thesis does not contain other persons' writing, unless specifically acknowledged as being sourced from other researchers. Where other written sources have been quoted, then:

a. Their words have been re-written but the general information attributed to them has been referenced

b. Where their exact words have been used, then their writing has been placed in italics and inside quotation marks, and referenced.

5. This thesis does not contain text, graphics or tables copied and pasted from the Internet, unless specifically acknowledged, and the source being detailed in the thesis and in the References sections

Signed:

……

"As the candidate's Supervisor I agree/do not agree to the submission of this thesis.

21 February 2016

Professor L. Combrinck

Date

Dr M. Akombelwa

Date

COLLEGE OF AGRICULTURE, ENGINEERING AND SCIENCE

DECLARATION 2 - PUBLICATIONS

DETAILS OF CONTRIBUTION TO PUBLICATIONS that form part and/or include research presented in this thesis (include publications in preparation, submitted, *in press* and published and give details of the contributions of each author to the experimental work and writing of each publication)

Publication 1

Nkosi, N.P., Combrinck, L and Akombelwa, M.A. (2015) Optical Configuration and Optical Tests of the HartRAO Lunar Laser Ranger. *South African Journal of Geology*. (In press).

Publication 2

Signed:

……

ACKNOWLEDGEMENTS

I would like to express my sincere gratitude to the following, for their assistance in fulfilling the requirements of this research:

- My supervisor, Prof Ludwig Combrinck for his assistance, guidance and provision of academic tools to accomplish the research.

- My co-supervisor, Dr Mulemwa Akombelwa for his assistance and motivation throughout the duration of the research.

- Roelf Botha for always going out of his way to provide me with whatever I needed, regardless of his busy work schedule.

- Kirsty Veale from the University of KwaZulu-Natal Mechanical Engineering department for assisting me with problems I encountered with ANSYS software.

- Lisa Crause from the South African Astronomical Observatory (SAAO) for her assistance and suggestions for optical testing.

- Jayren Kadamen from the University of Cape Town for his assistance in creating the CAD geometry of the primary used in the Finite element analysis.

- The National Research Foundation for sponsorship and funding of the project.

- Inkaba yeAfrica for the funding it provided and conferences I attended to gain more insight.

- My colleagues, Sphumelele Ndlovu and Cilence Munghemezulu for their on-going assistance with tasks I could not accomplish by myself.

- My parents, friends and significant other, Siphiwe Mphuthi for their constant support, patience and encouragement throughout the duration of my research.

ABSTRACT

The Observatoire de la Côte d'Azur (OCA) donated a 1-m Cassegrain telescope to be used for the dual satellite and lunar laser ranging system currently under development at the Hartebeesthoek Radio Astronomy in South Africa. As the very first of its kind in the Southern Hemisphere, the new system will be designed and developed as a permanent lunar laser ranging system with high precision laser and electronic equipment to achieve millimetre accuracy. Limited technical details of the telescope exist so tests were conducted to determine the optical characteristics and performance of the telescope and its mirrors. The optical performance of the telescope was validated through the analysis of transmission efficiency, structural efficiency and image quality. Spectroscopic measurements were conducted to determine the transmission efficiency of the telescope by taking into account all losses in light from the reflection of mirrors, transmission of lenses and the secondary spider central obstruction along the path of the proposed coudé optical path. A system transmission of ~90% was obtained if a coudé path with no central obstruction is used. The primary mirror and its support structure was validated using finite element analysis software (ANSYS) to model the amount of deformation the mirror will experience under gravitational and external loading. Taking into account the lightweight nature (honeycomb structure) of the mirror, its material properties and multiple support mechanism, ANSYS was used to compute the gravity deformations experienced by the mirror as the telescope tracks from the horizon to zenith. The deformations when gravity acts along the axial support were in the range of $1/6^{th}$ of the wavelength, which is below the maximum limit expected for such a structure at the given weight. In order to analyse the image quality of the system, an optical analysis software (OSLO) was used. Spot diagram analysis revealed coma as the dominant primary aberration in the system. The telescope is diffraction-limited for on-axis performance and yields a Strehl ratio of 0.78 for off-axis performance.

TABLE OF CONTENTS

LIST OF FIGURES

LIST OF TABLES

ACRONYMS

APOLLO – Apache Point Lunar Laser-ranging Operation

ATMOS - ATM Optical Design and Analysis Software

CCD – Charge-coupled device

CGH – Computer generated hologram

CTE – Coefficient of thermal expansion

ESO – European Southern Observatory

FEA – Finite element analysis

GMT – Giant Magellan Telescope

HartRAO – Hartebeesthoek Radio Astronomy Observatory

ILRS – International Laser Ranging Service

LLR – Lunar Laser Ranging

MLRS – McDonald Laser Ranging Station

MMT – Multiple Mirror Telescope

NASA – National Aeronautics and Space Administration

OCA - Observatoire de la Côte d'Azur

OSLO – Optics Software for Layout and Optimization

PSF – Point Spread Function

RMS – Root mean square

SALT – South African Large Telescope

SLR – Satellite Laser Ranging

WLRS – Wettzell Laser Ranging System

1
INTRODUCTION

1.1 Background

Since 1969, Lunar Laser Ranging (LLR) has strongly contributed to our understanding of the Moon's internal structure and the dynamics of the Earth-Moon system (Turyshev, et al., 2009). It is designed to obtain scientific information about the Moon, Earth, the lunar orbit and connected effects such as the nature of gravity. The LLR data are used for accurate determination of the Earth-Moon distance and to reveal information about the structure and dynamics of the Earth and Moon (Williams et al., 2007). However, the number of LLR stations is limited, with two stations located in the USA, one in France and recently the Satellite Laser Ranging (SLR) station in Matera, Italy also commenced with LLR. The German Fundamental Station located at Wettzell have also conducted tests recently (October 2015), using a 0.75 m aperture telescope and expect to have a functional LLR system in the near future.

All the active LLR ground stations are located in the Northern Hemisphere and do not cover a large range of latitudes, thereby weakening the geometric strength of observations. In order to strengthen the International Laser Ranging Service (ILRS) network and to limit biases caused by the under representation of the LLR network in the Southern Hemisphere, the Hartebeesthoek Radio Astronomy Observatory in collaboration with the Observatoire de la Côte d'Azur (OCA) and NASA is developing a dual system for lunar and satellite ranging utilizing a 1 metre Cassegrain telescope donated by OCA.

This new system is being designed and developed as a permanent LLR system with high precision laser and electronics equipment to achieve millimetre level accuracy ranging (Combrinck, 2005). The LLR system is being designed and built as a dual LLR/SLR system. The main mirror will be used for transmission when ranging to the Moon, and a refractor mounted on the side of the telescope for transmitting to satellites; both LLR and SLR will use the main mirror for reception. According to Combrinck (2012), the aim of HartRAO is to do laser ranging redesign rather than up-scaling of typical current designs. The basic subsystems of the system include the telescope, laser, photon-detection system; transmit/receive optics, timing and oscillator, ranging electronics, meteorological equipment, shelter and the pointing and steering software.

The telescope is a 1-m Cassegrain donated by the Observatoire de la Côte d'Azur (Figure 1-1). Due to the telescope having not been used in over a decade, all information and details of the telescope characteristics were not found. As a result, characterization of the optical system

forms the foundation of the overall project. Before refurbishments and optimization can be done, the telescope will have to be tested to determine the optical quality and thereafter, optimized to achieve millimetre accuracy to the Moon. Optical evaluation of the telescope forms the basis for this research.

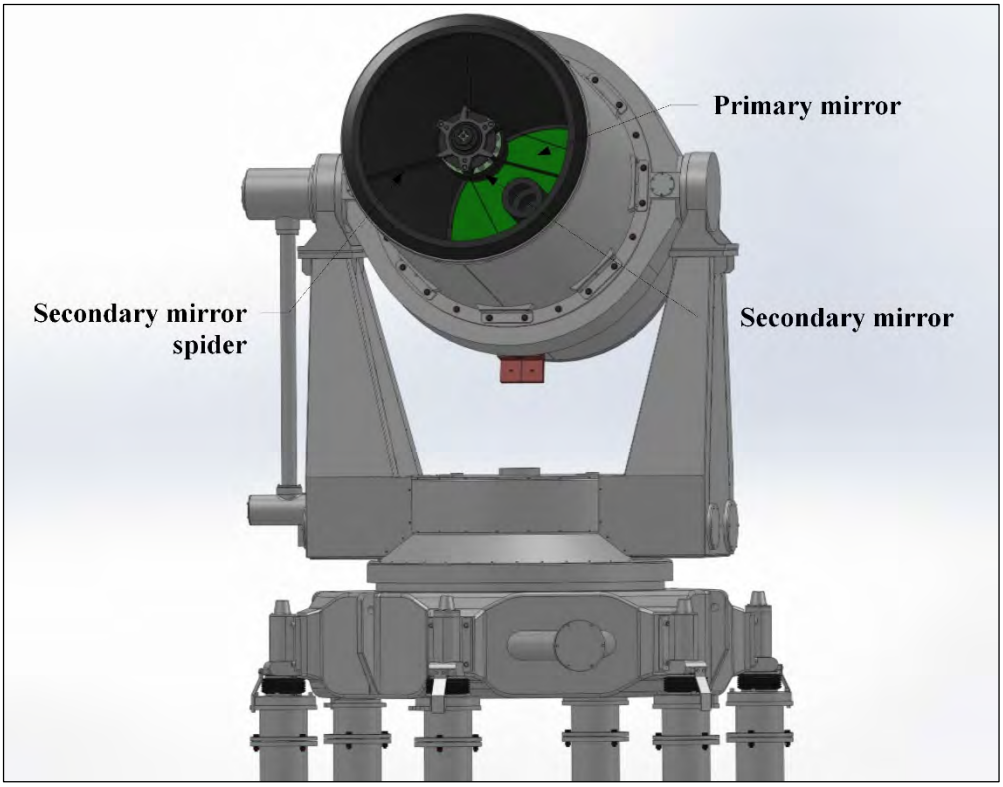

Figure 1-1: A model of the HartRAO telescope (courtesy of Wikus Combrinck).

1.2 Research problem

In order to achieve millimetre ranging accuracy to the Moon, the optical configuration of the system should be of a certain standard. The lack of knowledge about the optical characteristics presents a problem due to the fact that the optical performance of a telescope is dependent on these characteristics. Generally, an optical error budget comprises optical design imperfections and primary mirror wavefront errors due to mechanical and thermal effects (Bely, 1993). On that account, accurate testing and analyses of the optics are of paramount importance.

1.3 Research question

In order to conduct laser ranging to the Moon and satellites, the laser beam generated on a laser table must be propagated via a complex path from the laser generating point until it exits from the main tube of the telescope. This research therefore aims to answer the following question:

What is the optimal combination of existing and additional optics to enable determination of the characteristics of a laser beam path of the HartRAO Lunar Laser Ranger to the extent that it will allow optimum optical performance?

1.4 Aims and Objectives

The aims of this research are to determine the characteristics of the optical elements in the Cassegrain telescope through which a laser beam will be transmitted during laser ranging and to evaluate its performance through the analysis of image quality, transmission and structural efficiency. These aims will be achieved through the following research objectives:

1. Determination of the optical design parameters of the telescope such as the diameter of the mirrors, their focal lengths, focal ratio and reflection coefficients through measurements and calculations using Cassegrain equations.

2. Designing of a laser beam coudé system to transport the laser from the laser table to the telescope through a temperature and moisture controlled tube.

3. Evaluation of the image quality of the telescope through analyses of aberrations, spot diagrams and Point Spread Functions.

4. Determination of the transmission efficiency of the telescope through spectroscopic measurements of optical elements in the coudé path.

5. Evaluation of the structural efficiency of the telescope primary mirror under operational loads through Finite Element Analysis.

1.5 Delineations and limitations

The optical performance of a ground based telescope is usually limited by imperfect optics and atmospheric effects (Dierickx, 1992). This work only considers the contribution by the optics. Unlike atmospheric effects, the optics of a telescope can be optimized to meet desired standards by proper fabrication, alignment and the use of auxiliary optics to compensate for certain aberrations. Although the degradation of quality as a result of warped optics is usually smaller than that produced by the atmosphere, it becomes more significant as the aperture becomes larger (Brown, 1979). The optical performance is expressed in terms of transmission efficiency (influenced by coudé optics and effectiveness of mirror coatings), image quality and surface deformations of the primary mirror.

1.6 Research Motivation

An LLR system in the Southern Hemisphere will improve the geometry of the tracking network, its instrumental capability as well as research ability (Combrinck, 2011). Densification of the ILRS network will aid precise orbital determination projects. The LLR data will allow gauging relative acceleration of the Earth and Moon towards the Sun in order to test the Strong Equivalence Principle (SEP) of Einstein's General Relativity Theory. Merkowitz (2010)

mentions that improvements in the geometric coverage, both on Earth and on the Moon, will have a direct impact on the science gained through LLR. The addition of one or more ranging stations in the Southern Hemisphere would strengthen the geometric coverage and increase the sensitivity to lunar motion by as much as a factor of 4 in some degrees of freedom at the same level of ranging precision (Merkowitz, 2010).

Cheng (2009) has classified the primary mirror as the most important component of an astronomical telescope. This is due to the fact that the overall efficiency of the telescope is directly related to its size, the reflectivity of its coatings as well as its surface accuracy. Consequently, all characteristics of the primary mirror become of utmost importance. These include its shape, material, mount etc. This work serves to study and analyse terrestrial effects which can tend to interfere with the performance of the primary mirror.

1.7 Chapter overviews

The dissertation has 7 chapters. In Chapter 2, a review of the common tests used to evaluate the optical performance of telescope mirrors and of optical telescopes is provided. In Chapter 3 detailed information about the mirror design of the HartRAO telescope is provided. Some of the properties discussed include the mirror structure, material and support system. Chapter 4 contains a discussion of the theoretical background of primary aberrations in Cassegrain telescopes, including their effect on diffraction patterns. The different methods and techniques employed to achieve all the aims of the research are discussed in Chapter 5. In Chapter 6, calculated optical characteristics of the telescope are provided. Telescope transmission efficiency was calculated from spectroscopic measurements of coudé optics. Image quality analysis results of the optical system are provided and their implications discussed. The chapter is concluded by presenting deformation models of the primary mirror under gravitational effects. In Chapter 7, the ramifications of the obtained results are discussed and all the work undertaken in this research are tied together to give a reliable conclusion about the optical performance of the HartRAO telescope. Lastly, future work and recommendations regarding analysing the surface figure accuracy of the primary mirror are provided.

2
LITERATURE REVIEW

2.1 Introduction

A review of common tests usually used to test optical telescopes is conducted in this chapter. To begin with, a brief outline of the history of Lunar Laser Ranging is given, where all the optical and mechanical characteristics of each existing LLR systems are discussed. In addition, the ranging accuracy of each one of these systems are compared and contrasted with the target accuracy of the current LLR system under development in South Africa.

The optical testing methods discussed are grouped into tests conducted during manufacture and those conducted after manufacture (evaluation). Tests conducted during manufacture often require specialized equipment and more often than not, a reference optic larger than the sample under test. The results of such tests are often in visual representations, requiring a form of skill to analyse and interpret. Optical evaluation tests, on the other hand, are conducted on finished products, requiring little or no specialized equipment and/or reference optics (Suiter, 1994). Lastly, the tests are categorized into those specially designed to measure parabolic primary mirrors and convex secondary mirrors. The shortcomings of the individual tests are also discussed.

2.2 History of Lunar Laser Ranging

According to Bender (1973), lunar laser ranging became a reality in 1969 after the first deployment of a retro-reflector package on the Moon's surface by the Apollo 11 mission. The 3.1 m telescope at Lick Observatory was used to make the first lunar laser ranging observations of this retroreflector (Faller et al., 1969). The McDonald observatory in the USA built a lunar lasing system that currently contributes to continuous LLR data. This system was constructed in 1979 and consists of a 0.76 m aperture Cassegrain/Coudé reflecting telescope. The optical characteristics of the telescope are displayed in Table 2-1. The coudé system was designed such that a 3 cm diameter focal lens collimates the beam for a 2.74 m travel path to beam expanding and beam splitting optics before entering laser and photo multiplier housings. The coudé path optics components were coated to maximize transmission of green (wavelength of 532 nm) light. The beam splitter directs wavelengths of less than 555 nm to the coudé part of the system and wavelengths of greater than 555 nm to the Cassegrain. The MLRS was built around a frequency doubled neodymium-YAG laser and now produces LLR data approaching 1 cm normal point accuracy.

At about the same time, a new station began operating in the south of France, close to Grasse, at the Observatoire de la Côte d'Azur (OCA). Equipped with a telescope of 1.5 m

aperture and a laser which fires at 10 Hz with pulse power of 75 mJ, this station became the premier lunar ranging station in the world (Murphy et al., 2008). The telescope collimates the laser beam in the lunar direction. The transmit path is through the main optics of the Cassegrain, as illustrated in Figure 2-1, and the receive path is a common coudé as with the MLRS. The OCA system permits instrument calibration which allows the transit time of the light pulse between the corner cube on the Moon and the calibration corner cube to be accurately known (Semain et al., 1998).

Table 2-1: Optical Characteristics of MLRS lunar laser ranging telescope (adapted from: http://www.csr.utexas.edu).

Primary Mirror	
Diameter	76.2 cm (30") paraboloid
Focal length	228.6 cm (90")
F-ratio	3.0
Cassegrain System	
Secondary Mirror	20.0 cm (7.87") hyperboloid
Focal length	10.67 m (420")
F-ratio	14.0
Field angle	36 arcmin
Plate scale	19.33 arcsec/min

Although the MLRS and OCA systems managed to successfully carry out ranging to the Moon, it was development of the Apache Point Observatory Lunar Laser-ranging Operation (APOLLO) in USA, which changed Lunar Laser Ranging as we know it. The APOLLO system provided a major improvement in lunar ranging capability (Murphy et al., 2008). The system consists of a 3.5 m aperture telescope; the laser, optical system and detector and timing electronics, which are all affixed to the telescope. The coudé system is the same as the MLRS system. In the case of APOLLO, the optical train (Figure 2-2) was designed such that transmit and receive share the full aperture of the telescope. The laser pulse is arranged to strike the highly reflective patch on the transmit/receive optics so that it is sent to the telescope main mirror. Further, the transmit/receive optics present a clear path from the telescope to the receiver. APOLLO has achieved 1 mm range precision to the Moon, which should lead to

approximately 1 order-of-magnitude improvement in several tests of fundamental properties of gravity (Murphy et al., 2008).

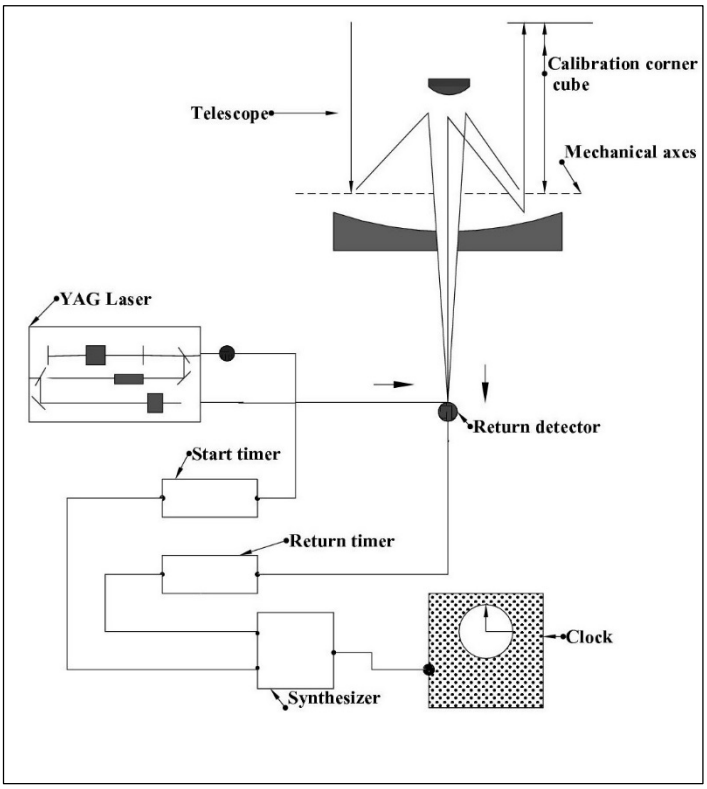

Figure 2-1: OCA Lunar Laser Ranging subsystems (Semain et al., 1996).

Furthermore, the Wettzell laser ranging system (WLRS) in Germany has dual capability of both satellite and lunar laser ranging. The system was designed and constructed in the period between 1986 and 1989. It uses a 0.75 m aperture telescope to transmit and receive the laser pulse and for guiding the target (Schleuter, et al., 1984). The laser is an Nd: YAG and has two colour capability for wavelengths of 532 nm and 1064 nm. Lunar tracking is however, not yet a routine procedure. This system is currently being upgraded and will be dedicated to LLR in the near future; a separate system is being developed using a telescope built by Zeiss for SLR purposes.

2.3 Performance evaluation and optical testing

The performance of an optical telescope depends on the image quality through assessment of aberrations. The star test has been described as the simplest test for assessing the optical quality of an image–forming telescope (Malacara, 2007). This technique is performed by observing a bright star inside and outside of focus and any difference in the two images will indicate the fault in the system. Morison (2009) mentioned how this test is used to test if a telescope is perfectly collimated, which is required in reflecting telescopes. With the use of freeware software such as Aberrator (http://aberrator.astronomy.net/index.html), star testing images can

be generated to show the effects of aberrations influencing the quality of the telescope performance. The test however presents two disadvantages, the first being that it is dependent on the observers personal judgement and secondly in the qualitative nature of the results, producing no numerical data.

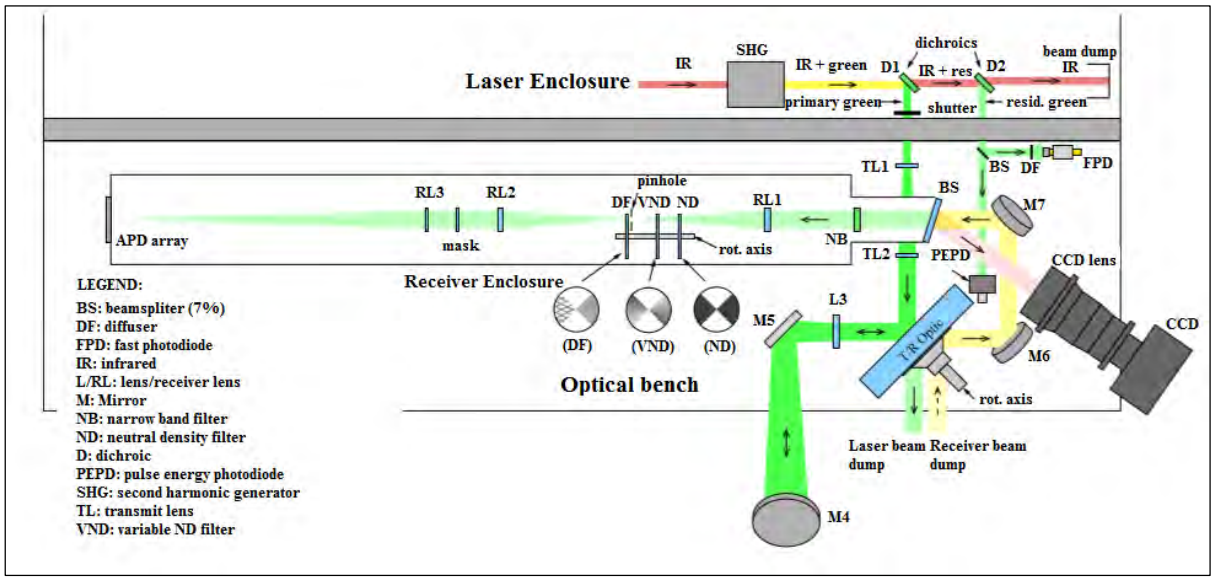

Figure 2-2: Components of the APOLLO system optical train (Murphy et al., 2006).

Some optical tests for testing the mirrors can also be used for testing telescope quality. One such test is the Hartmann test which was categorized by Merrill (2009) as scientifically the best way to determine the level of optical quality in a telescope. This test was applied in testing the Southern African Large Telescope (SALT) system (O'Donoghue, 2008), the ESO 3.6 m telescope (Wilson, 1974) as well as the performance of the Hobby-Eberly Telescope (Palunas, 2006). Software was developed to reduce data and compare the results to a perfect telescope model. The Santa Barbara Instrumentation Group (SBIG) developed Hartmann test software which can run an analysis of the inside and outside of focus images to give a Hartmann constant which indicates the level of quality of the telescope (Merrill, 2009). Suiter (1994) disregards this method due to the reason that the mathematical reduction of the Hartmann test results is advanced and extensive, which can be a tiresome chore.

Another mirror test which can be used for testing telescopes is the Foucault Knife-Edge test. The optical system is set up in a collimator having an equal aperture to or larger than the system under test. The image can be recorded on a photograph or a video. This test was used by Beckers et al. (1981) in the MMT system in testing for coma, astigmatism and stellar optical quality.

Roddier and Roddier (1993) used the closed-loop wavefront reconstruction technique to test the optical quality of ground telescopes. This algorithm involves using defocussed stellar images, recorded on a CCD camera, to reconstruct a wavefront. The reconstruction becomes inaccurate if large aberrations are present. The method is about as accurate as the Hartmann test but with higher spatial resolution of the wavefront map of errors.

Navarro and Moreno-Barriuso (1999) developed a laser tracing method to measure aberrations in optical systems. This method consists of tracing light rays through an optical system and measuring the centroid of the image in the image plane. The spot diagram from the centroids is used to estimate the wavefront aberrations from Zernike polynomials. A good match between aberrations was obtained by Navarro and Moreno-Barriuso (1999) when comparing this technique to a Hartmann-Shack sensor method as displayed in Figure 2-3, thereby confirming the validity of the laser tracing method.

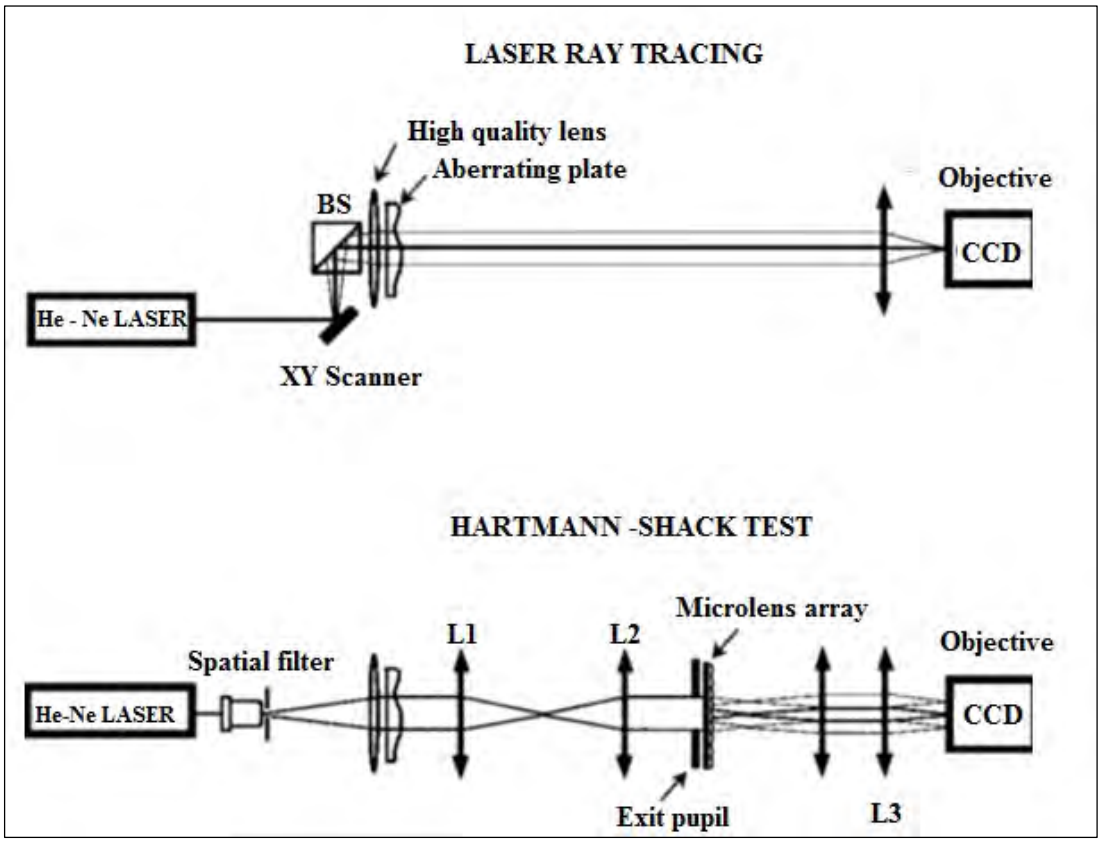

Figure 2-3: Laser Ray tracing and Hartmann-Shack tests used for testing aberrations in optical systems (Navarro and Moreno-Barriuso, 1999).

2.4 Optical testing of large aspheric mirrors

In simple terms, an aspheric surface is an optical surface which deviates from a spherical shape. The use of aspheric surfaces on optical systems is becoming advantageous since they improve

aberration correction, image forming quality and they require few elements in the system (Shannon, 1997). An aspherical surface with rotational symmetry can be defined by the sag z of the optical surface and the object height h from the optical axis. It is given by Malacara (2007) as:

$$z = \frac{ch^2}{1+\left[1-(K+1)c^2h^2\right]^{1/2}} + A^4h^4 + A^6h^6 + A^8h^8 + A^{10}h^{10}.... \quad (2.1)$$

Here c is the curvature at the optical axis, given by the inverse of the radius of the curvature, K is the conic constant, which is a measure of the conical shape of the surface and A_4, A_6, A_8, A_{10} are the aspheric deformation coefficients in the 4th, 6th, 8th and 10th order respectively. The conic constant is a function of the eccentricity of a conic surface and can be given as $K = -e^2$. If all the aspheric deformations constants A_i are zero, then the surface described is purely conical. Table 2-2 lists all conical surfaces with their respective conic constant relations. The HartRAO telescope mirrors fall under the category of conical aspheric surfaces. The tests described in this study are for these particular conical surfaces.

While aspheric surfaces have their advantages, they also present certain limitations. Unlike flats and spherical surfaces, aspheric surfaces have always proved to be most difficult to test due to the large slope of aspheric departure (Wyant and Bennett, 1972). The large slope causes the reflection from a convex surface to diverge, requiring auxiliary optics larger than the optic being tested. This makes optical testing of large aspherics to be vastly expensive. Literature in optical testing of parabolic and hyperbolic mirrors has reflected an improvement in accuracy, with the realisation of methods which do not require large auxiliary optics.

2.4.1 Testing large Parabolic mirrors

2.4.1.1 Interferometers with a Null corrector

Several authors recommend testing of large paraboloid mirrors at their centre of curvature. This was mostly done by use of a null corrector to compensate for the asphericity of the mirror and to allow accurate high resolution measurement of the entire surface. The null corrector can be in the form of lenses, mirrors or Computer Generated Holograms (CGH) (Yang et al., 2005). The configuration of this method is depicted in Figure 2-4. In many cases, the null corrector is used with interferometers as were done at the Steward Observatory Mirror Lab for the testing of the Multiple Mirror Telescope (MMT) and Giant Magellan Telescope (GMT) during testing of their primary mirrors. During the testing of the 6.5 m MMT primary mirror, a Twyman-Green interferometer with HeNe laser co-aligned with a BK7 null corrector was used together with an infrared interferometer with a germanium and ZnSe null corrector (Burge et al., 1999). These null lenses were verified by means of CGH, qualifying the optical design to a wavefront error of

4 nm rms and maximum mapping error of 5%. Failure to verify the null corrector was one of the reasons for the failure of the Hubble Space Telescope when testing its primary mirror (Allen et al., 1990).

Table 2-2: Values of conic constants for conic surfaces (Malacara, 2007).

Type of conic	Conic constant value
Hyperboloid	K < -1
Paraboloid	K = -1
Prolate spheroid or ellipsoid: (ellipse rotated about its major axis)	- 1 < K < 0
Sphere	K = 0
Oblate spheroid (ellipse rotated about its minor axis	K > 0

Another interferometer that can be used with a null corrector to test large aspheric mirrors is the Shack interferometer displayed in Figure 2-4 (Malacara, 2007). The type of null corrector to use often depends on the size of the mirror under test. In his vast experience in mirror testing, Ceravolo (2003) maintains that the use of the Roll null lens is best for testing large parabolic mirrors. The only drawback of this null lens is that it should be as big as the paraboloid which can become impractical for very large parabolic mirrors.

2.4.1.2 A tilted sphere as a null lens and Computer Generated Holograms (CGH)

Another optical test with a null corrector was used to test the New Solar Telescope primary mirror and the mirror segments of the GMT (Martin et al., 2004, Zhao et al., 2005, and Burge et al., 2006). The test arrangement is illustrated in Figure 2-5. A tilted fold sphere was used as a null lens, working together with a CGH to correct for all aberrations in the mirrors. A fold mirror rotates the mechanical reference axis by twice the angle between the entrance reference angle and the local reference axis direction. The CGH was also used to align the null corrector and the telescope. Burge (2006) estimated optical alignment tolerance for this test system to be 33.85 nm rms.

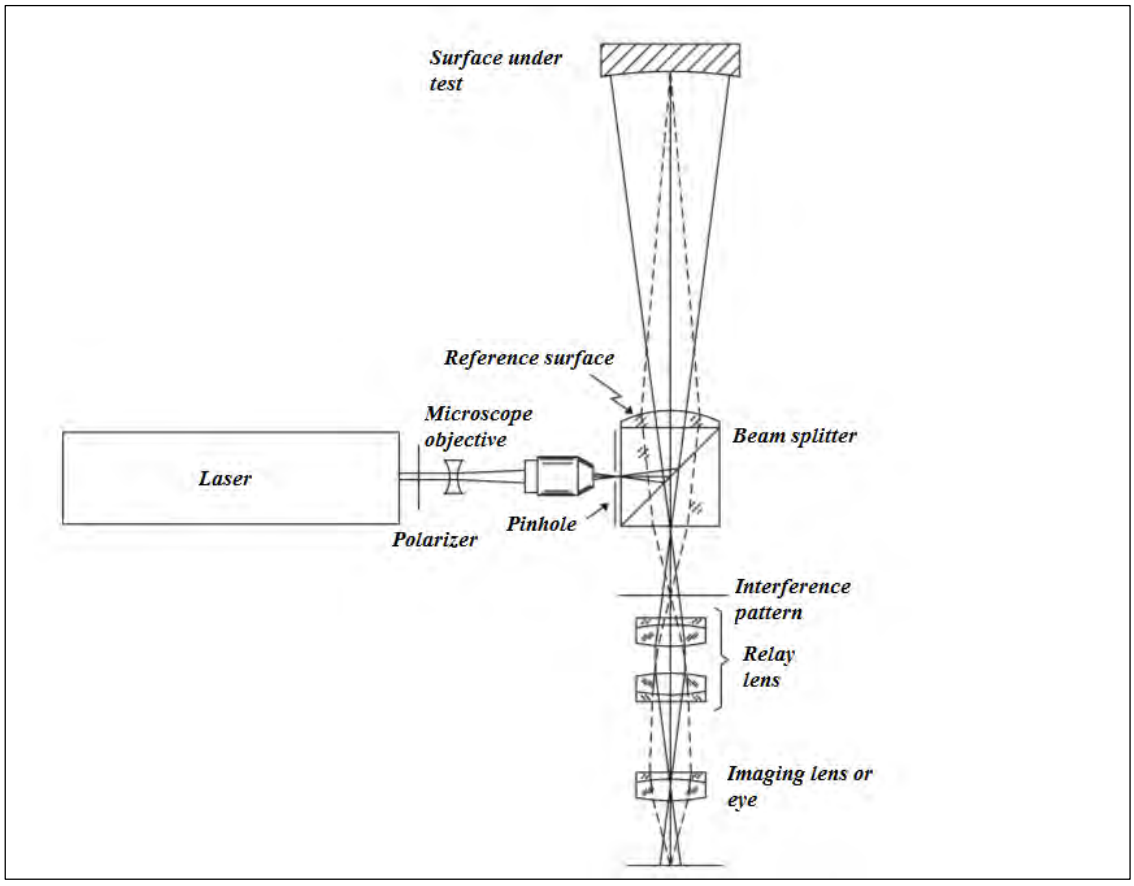

Figure 2-4: An example of an interferometric test with a null corrector for testing an aspheric mirror (Malacara, 2007).

2.4.1.3 Hartmann test

The Hartmann test, invented by J. Hartmann, was specifically developed for optical quality testing of large professional telescopes (Malacara, 2007). This was done by placing a screen with holes in it close to the entrance and exit pupil of the surface under test and analysing the residuals of the image spots formed on either side of focus. This was the test used testing the ESO 3.6 m parabolic mirror in 1976 (Wilson, 1974). The screen was 2 dimensional and a computer was used in the analysis, which revealed a serious error of astigmatism at about 0.75 λ at a wavelength of 500 nm. In 1990, Porter described how the Hartmann test was used to test aberrations in the Hale 5 m telescope primary (Porter, 1990). The Hartmann screen had 400 holes of 50 mm in a polar grid. The tests were first done with plates, then with a Tektronix device and these tests were run on CCD for analysis. The mirror's astigmatism was observed and no aberrations greater than 0.5 wavelengths were found.

Korhonen et al. (1991) used an interferometric modification of the Hartmann test together with a 0.63 m compensating mirror to test the 2.5 m Nordic Optical Telescope primary mirror. The interferometric images formed were detected on a CCD, showing a mean error of approximately 10 nm. This arrangement (Figure 2-6) is similar to that used to test the 1.5 m SiC

M1 mirror of the Atmospheric Laser Doppler Instrument (ALADIN) instrument on the ADM-Aeolus satellite of ESA. Instead of a compensating mirror, an Offner lens was used for wavefront correction (Korhonen, 2008). For redundancy, a pentaprism test was added in the optical test design, primarily to verify the correct conic constant of the mirror. The pentaprism test yielded a wavefront error of 148 nm while the interferometric test gave a wavefront error of 143 nm.

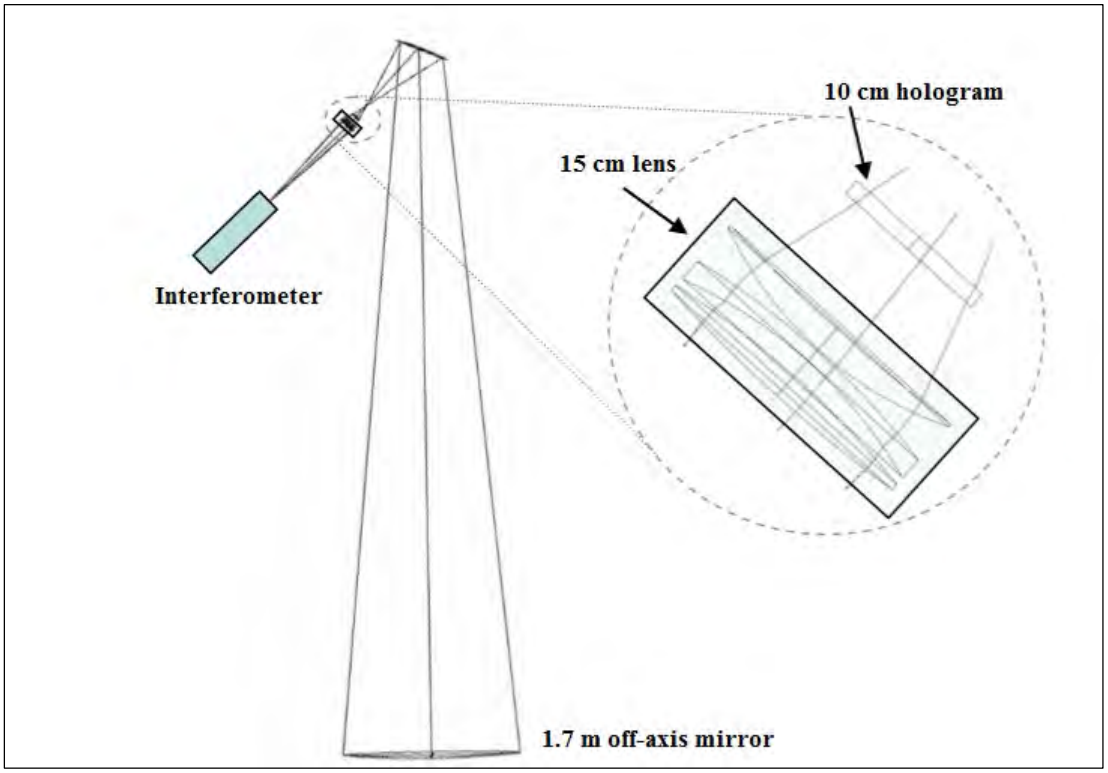

Figure 2-5: The test configuration of the GMT segment measured using a null corrector consisting of a tilted spherical mirror and a computer generated hologram (Burge at al., 2006).

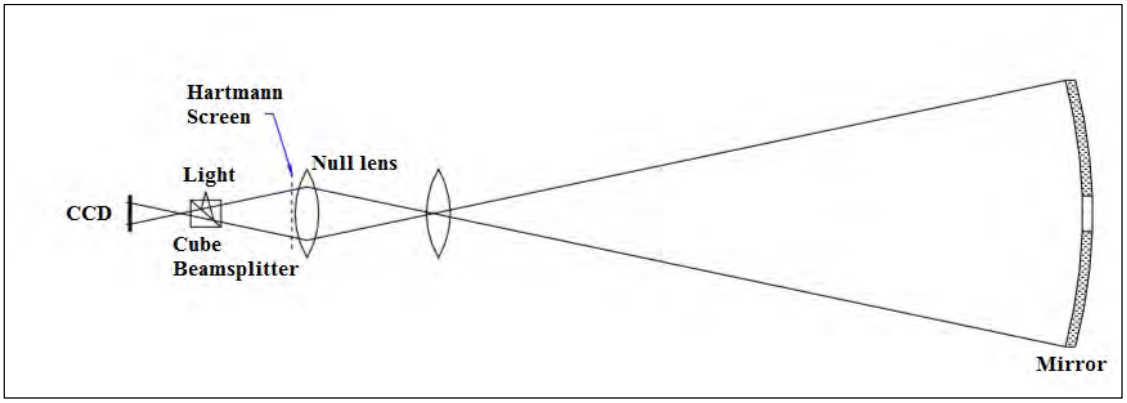

Figure 2-6: An optical layout of the Hartmann and Interferometric Hartmann tests (Korhonen et al., 2008).

2.4.1.4 Autocollimation test

The autocollimation test, also called the double pass test is considered as the best for parabolic mirrors among experienced telescope makers (Cervalo, 2003 and Malacara, 2007). This is due to the advantage that the light rays bounce off the surface twice thereby making it sensitive in the detection of figure errors. The drawback of this test is that it requires a flat mirror as large as the optic under test with high quality and these are difficult and expensive to manufacture. This test was used to figure the MMT primary mirror in 1981 (Berkers et al., 1981). The autocollimation test can also be used to test an entire optical system including optics installed in the telescope.

2.4.1.5 Foucault Knife-Edge test

Proposed by Leon Foucault in 1859, the Foucault test is well regarded in testing parabolic mirrors (Malacara, 2007). Young-Soo (2001) has described the Foucault test as one of the best methods for overcoming optical testing limitations of aspheric mirrors such as high cost, long lead times in the test design, difficulty in calibration and decrease in precision. In this test, a mirror with aberrations will cause a reflected ray from a light source to divert to another location instead of going back to a single point.

2.4.2 Testing large convex hyperbolic mirrors

2.4.2.1 Holographic test plate

Burge (1996) developed a method for testing large convex mirrors by using full-aperture test plates with computer generated holograms fabricated (CGH) onto spherical reference surfaces. Figure 2-7 illustrates the test design where the CGH fabricated reference mirror will be illuminated with laser light to form an interference pattern detected by the CCD camera. The test was designed to give surface measurement accuracy of 4 nm rms for secondaries up to 1.15 m in diameter. In addition to testing most of the secondary mirrors at the Mirror Lab at the University of Arizona, this technique was also used to test the 1.7 m secondary mirror of the MMT, yielding a surface measurement accuracy of 6 nm rms (Burge et al., 1994).

2.4.2.2 Hindle-Sphere test

Wilson (1974) described the Hindle-Sphere test as “undoubtedly the best method in existence” for testing Cassegrain secondary mirrors. This test was first suggested by Hindle (1931) and uses a concave sphere to produce a perfect spherical converging wavefront of the hyperboloid as illustrated in Figure 2-8. According to Parks and Shao (1988) the test is advantageous in its basic simplicity, perfect null and its double sensitivity to errors in the convex hyperbolic surface because of the double reflection from that surface. The drawback of this method is that the sphere has to be much larger than the hyperboloid under test which becomes impractical for secondaries of more than 1 m in diameter (Malacara, 2007). This technique was successful in

testing the M2 secondary mirror for the VISTA telescope project, giving an RMS wavefront of less than 40 nm (Abdulkadyrov et al., 2008). It was, however, not used to test the large ESO 3.6 m secondary mirror due to the large sphere requirement (Wilson, 1976).

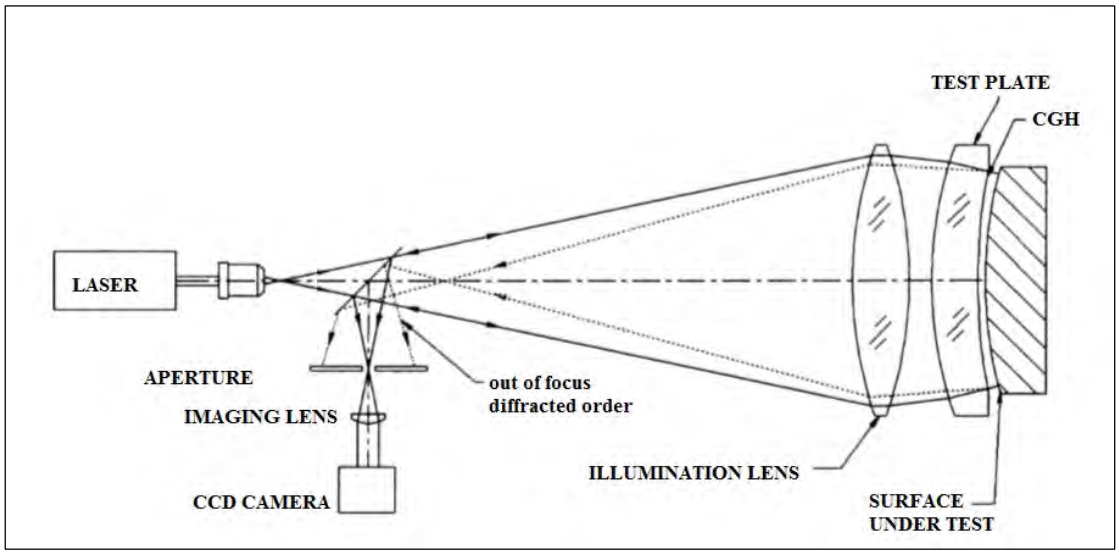

Figure 2-7: A Fizeau interferometer with CGH test plates for testing large convex mirrors (Burge, 1995).

Jiang et al. (2012) suggested use of the Hindle method (Figure 2-8) based on the stitching technology to test large diameter convex hyperboloids. This is done by testing sub-apertures of the surface and then stitch the sub-aperture results together to obtain the full surface. This method was however deemed by Wyant (1992) as inconvenient and unreliable.

2.4.2.3 Hindle-Simpson test

The central obscuration produced by the Hindle test can be avoided by using a method described by Simpson et al., (1974). In this test, a meniscus is used to serve as the Hindle sphere to refract light from the near focus of the hyperboloid. This test can be considered cheaper than the classic Hindle test since the meniscus does not have to be large but yet still be precisely figured. Studies done by Robbert (1979) and Howard et al., (1983) show how any significant aberration introduced by the meniscus can be subtracted from the measurement of the figure error of the hyperboloid (Malacara, 2007). The Hindle-Simpson test was successful in the testing of secondary mirrors for the Anglo-Australian 3.9 m telescope (Wilson, 1974).

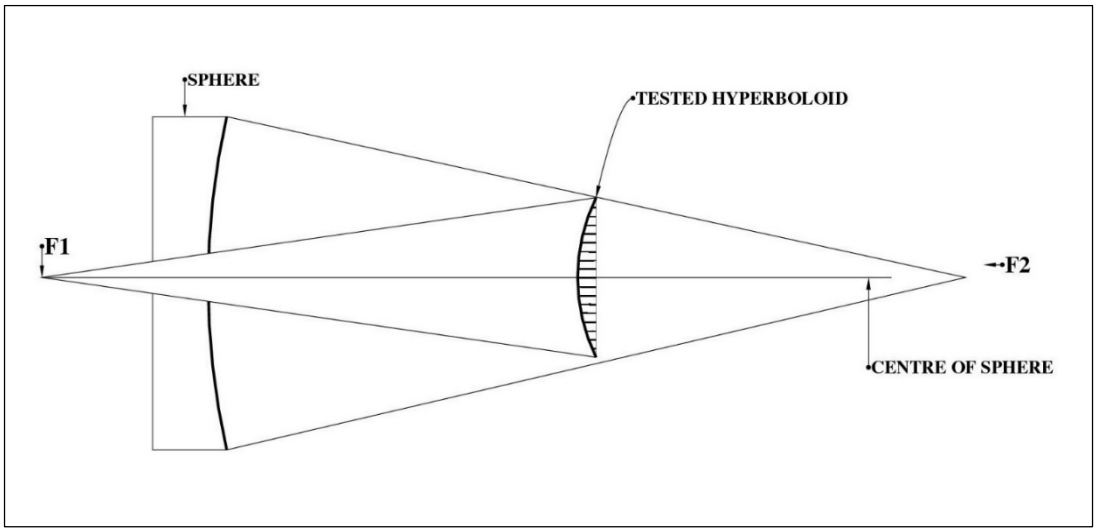

Figure 2-8: Hindle test (Li et al., 2012).

2.4.2.4 Lytle test

In their paper on testing large hyperbolic mirrors, Parks and Shao (1988) highlighted the use of the Lytle test for Cassegrain secondary mirrors. This procedure was suggested by Lytle in 1969 (Lytle, 1969). When placed at the centre of curvature of the primary mirror, together with a null lens, a null for the secondary is produced. The primary mirror should have an aperture larger than the secondary at its centre of curvature. Wilson (1976) classified this method as more universal in the testing of both the QRC secondary and coudé secondary of the ESO 3.6 m telescope.

2.4.2.5 Test Method

The test method, inverted by T.S McKechnie, offers an alternative to the Hindle - Sphere test (McKechnie, 2009). The test optic is polished to transform it into a lens and the mirror is tested as a lens using an interferometric null test. An ancillary lens, either flat or spherical, is used to cancel spherical aberration introduced by testing the mirror as a lens as illustrated in Figure 2-9. This technique was first implemented in 2009 to test the NASA 3 m telescope secondary mirror (Figure 2-9). It was also used to test the convex paraboloid of the Magdalena Ridge Observatory Interferometer, the 0.5 m HST secondary mirror and the larger 3.2 m TMT secondary (McKechnie, 2010).

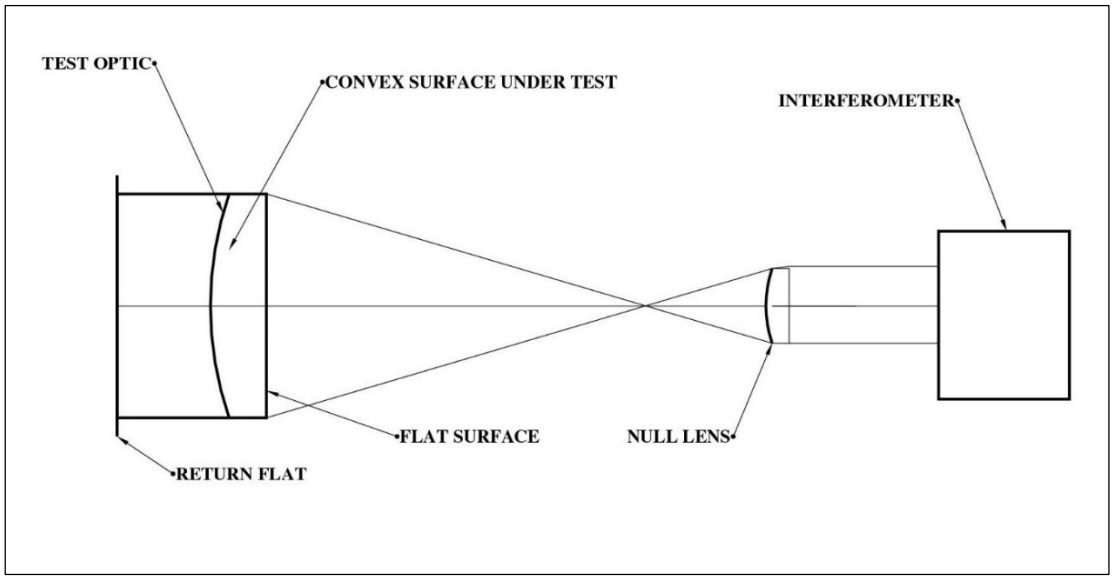

Figure 2-9: Optical testing configuration of the Test Method for testing the 244-mm secondary mirror of the NASA 3-m telescope (McKechnie, 2010).

2.5 Chapter Summary

The chapter began by providing an outline of the old and current stations responsible for Lunar Laser Ranging globally. The optical specifications of each system were discussed and all these measured against the expected accuracy of the LLR system currently under development in South Africa. It was seen that, up to date, the APOLLO system has been as the most efficient of all LLR systems due to, among other things, its large collection area of 3 m and good image quality. A second aspect of the literature involved common methods used to test the quality of Cassegrain telescopes. These were divided into two categories: those employed during and after manufacture. The type of tests employed during manufacture measure the accuracy of the shape and figure during polishing and fabrication. To do this, the mirrors would have to be removed from the telescope and measured individually in an optical shop. This is risky since the mirrors can easily be scratched or damaged. Further these types of tests require a reference optic larger than the mirror itself. It is for these reasons that such tests were disregarded as variable options for testing the HartRAO LLR telescope. The other category of tests discussed where those used to evaluate the overall telescope optical performance. The evaluation is done through an assessment of the image quality of the telescope. These tests have been seen to be the most favourable due to their high precision and accuracy. There is also no need for auxiliary optics when doing the tests.

3

HARTRAO LUNAR LASER RANGING TELESCOPE MIRROR DESIGN

3.1 Introduction

Among the components that make up an astronomical telescope, the mirror is the most important (Cheng, 2009). The overall performance of the optical system depends on its characteristics and properties. These properties include the mirror shape, aperture size, figure accuracy, coating, weight, material and support system. This chapter contains a detailed discussion of the properties of the HartRAO Lunar Laser Ranging telescope and the impact each property has on the quality of the system.

The telescope is a two mirror system consisting of a concave parabolic primary mirror and a convex hyperbolic secondary mirror. Both mirrors are annular, have the same design and are made of the same material. The mirror design falls under a category of lightweight mirrors called honeycomb sandwich mirrors made from Schott Zerodur glass ceramic material. Properties and drawbacks of this type of mirror design and material will be discussed in detail. The primary is held in place by a whiffle-tree cell. One of the most critical parts of a telescope is the mirror cell as it holds the mirror in place and allows for collimation adjustment as well as constitutes the support assembly for the secondary mirror. A three vane spider made of aluminium and steel supports the secondary assembly.

3.2 Mirror substrate

The development of large ground-based telescopes saw a growing need for lightweight mirrors to prevent gravitational deflections during operation. There are many techniques by which the weight of the mirror can be reduced. These include using thin mirrors, honeycomb mirrors, multiple mirror telescopes and segmented mirror telescopes. All these techniques provide a compromise between mirror cost and weight. Both the primary and secondary mirrors of the HartRAO lunar laser ranger are of a honeycomb sandwich mirror design. This type of light weight design has hexagonal pocket holes at the back of the mirror blank for support and ventilation as illustrated in Figure 3-1.

However, the honeycomb mirror design is not without its shortcomings. The two main challenges are complexity in design and fabrication as well as in mounting. The techniques commonly used to generate such mirrors include casting, fusion of individual components to a total structure or light weighting a massive block by various mechanical machining methods

(Hoeness et al., 1989). Each of these techniques has its own disadvantages. Fusion requires very high temperatures to fuse together silica sections to produce a lightweight sandwich mirror. Casting is often used on glasses which melt at relatively low temperatures. During this process, substantial hydrostatic pressure can cause the cores to break loose and the walls to deform, producing ribs of uneven thickness which reduces the flexural rigidity of the mirror (Bitzer, 1997).

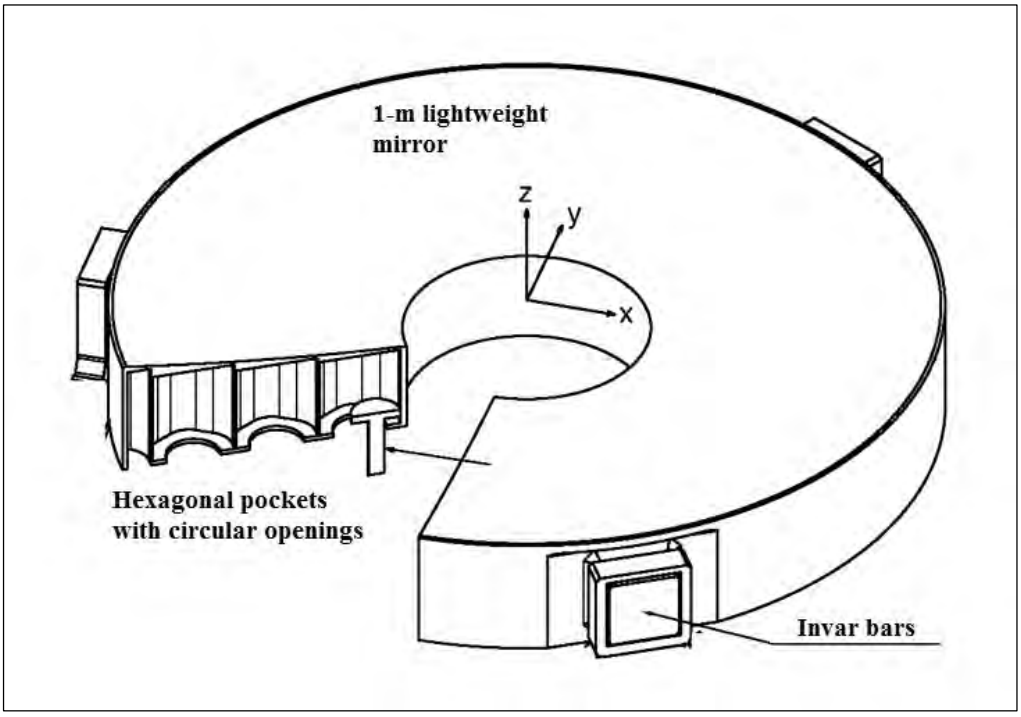

Figure 3-1: Sandwich honeycomb mirror designed from hexagonal pockets with circular openings (Kihm and Yang, 2013).

3.3 Properties of honeycomb sandwich mirrors

i. Low weight

Reduction of the mirror weight is very important in telescope design as the weight of the mirror is an indicator of the structure precision and complexity (Cheng, 2009). Honeycomb mirrors are manufactured through a process of fusing glass cores together at high temperatures or by removing mass from a solid block of glass in order to make it lighter. The mass of a sandwich mirror is usually about 20% - 40% the weight of an equivalent solid circular mirror (Vukobratovich, 1999).

ii. High stiffness

Sandwich honeycomb mirrors have the highest stiffness to weight ratio when compared to any other type of lightweight mirrors (Vukobratovich, 1999). The high strength and stiffness is very important to structural performance as the core carries the bulk of the shear loads. The high stiffness will minimize any shear deflections of the structure.

iii. Low thermal inertia

The ventilating effect of honeycomb mirrors caused by the holes on the interior provides reduced thermal equilibrium time for ground based telescopes. The core acts as insulation and heat transfer is kept to a minimum.

iv. High flexural rigidity

Sandwich mirrors combine high flexural rigidity and bending strength with low weight. This means the mirror will deflect less due to gravitational loading. The self-weight deflection is calculated through the use of flexural rigidity. The equivalent rigidity of a sandwich mirror is the flexural rigidity of a solid plate of equal thickness.

The flexural rigidity of a solid plate, given in metric units, without a light weight section is given by Equation (3.1), where D_{SOLID} = flexural rigidity of plate, E = elastic modulus of plate material, h = thickness of plate and v = Poisson's ratio of plate material,

$$D_{SOLID} = \frac{Eh^3}{12(1-v^2)}. \tag{3.1}$$

3.4 Mirror Material

According to Bely (2003), the mirror substrate material used in the design and construction of large telescopes should possess important qualities, such as high stability, low internal stress, high mechanical rigidity and strength as well as low coefficient of thermal expansion (CTE) to prevent deformation under temperature changes.

Zerodur glass ceramic has been a highly recommended material for making astronomical mirror blanks for more than 35 years due to its zero CTE at ambient temperature (Döhring, 2008). Zerodur shows remarkable properties which makes it a material of choice for use as a mirror substrate. These include the following:

i. Extremely low coefficient of thermal expansion

Changes in day and night temperatures will cause telescope mirrors to undergo thermal variations as it tries to reach equilibrium. The mirror material should be able to accommodate this change. Zerodur glass ceramic has an extremely low CTE over a wide range of temperatures. This property allows the mirrors to be used in observatories irrespective of surrounding environmental temperatures without any concern for thermally induced deformation. It also allows shipping and handling of the mirrors without any special thermal precautions.

ii. High material homogeneity

As the temperature changes, the thermal expansion of Zerodur will remain homogenous throughout the entire surface. This means that the material will remain uniform, without irregularities. Extreme temperature variations may cause the focal length of the mirror to change but the high homogeneity will prevent any effect on the figure. Figure 3-2 illustrates the homogeneity map of the HartRAO LLR's 300 mm secondary mirror tested with an interferometer at a wavelength of 546 nm. The homogeneity is much higher in smaller areas of the centre of the blank.

iii. Bending strength

It is important for a mirror substrate to have sufficient rigidity and strength to allow handling and mounting. Generally, Zerodur is stronger than glass. The strength of Zerodur is determined by the depth of micro-cracks in its surface and the smaller the micro-cracks, the higher the strength of the material. The material should be able to withstand mechanical loads beyond and in addition to the weight of the mirror. Zerodur can withstand loads up to 10 MPa on any undamaged surfaces. Higher loads should be analysed in detail to prevent degrading of surface quality.

iv. Chemical stability

Zerodur has excellent chemical stability. It can react with certain acids and salts at room temperature without leaving residual traces on the surface. An aluminium coating of a polished mirror substrate can be removed and recoated a number of times without affecting the characteristics of the mirror (Döhring, et al., 2006).

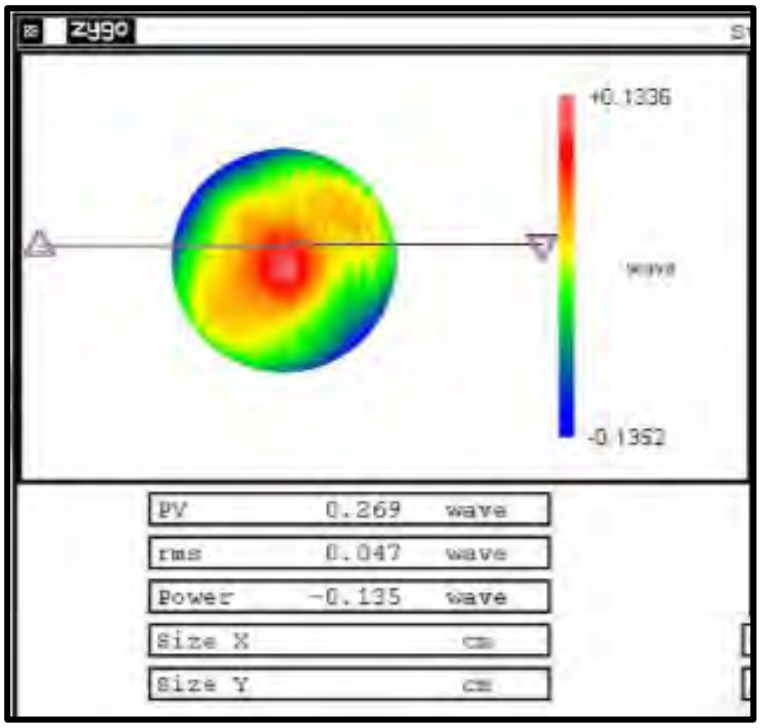

Figure 3-2: Homogeneity map of the 300 mm secondary blank of the HartRAO LLR system (courtesy of MIL-OP systems).

3.5 Mirror Support mechanism

Most ground based telescopes suffer from deflection due to its own weight under gravity and wind loading. These deflections affect the shape and position of surfaces in the optical system. The surface figure accuracy of the primary mirror has a direct effect on the performance of the whole optical system. To limit deflections, the mirror support should meet certain requirements such as maintaining the nominal figure accuracy under zenith and horizon operational angles; have adequate stiffness to control piston and tilt errors from the wind and maintain stresses within an acceptable precision elastic limit of the material (Cho, 2001).

3.5.1 Deflection due to self-weight

The structural efficiency of a support structure is determined by the fundamental frequency (Vukobratovich, 1999). The fundamental frequency of a structure is defined as a measure of the stiffness to weight ratio of a structure. Self-weight deflection in space optical systems is related to the change in optical figure upon gravity release in space and the fundamental frequency of the mirror. The relationship between self-weight deflection and fundamental frequency is given by Equation 3.2 as

$$f_n = \frac{1}{2\pi}\sqrt{\frac{g}{\delta}}. \tag{3.2}$$

In Equation 3.2, f_n = fundamental frequency (Hz), g = acceleration due to Earth's gravity, δ = self-weight deflection of the mirror.

During ranging, the angle changes continuously as the telescope tracks across the sky from horizon to zenith. The changing gravity vector direction causes self-weight deflections on the mirror, with the worst case deflections occurring along the axial direction. This is when the gravity vector is normal to the plane of the mirror and parallel to its optical axis. The least deflection often occurs along the radial direction. This is when the gravity vector is parallel to the plane of the mirror and normal to the optical axis.

If the mirror is subjected to a loading condition in which the gravity vector is at an angle to the axis of symmetry, as depicted in Figure 3-3, the resulting mirror surface deflections as defined by Vukobratovich (1999) are given by the vertical and horizontal components. If δ_A is the mirror self-weight deflection in axial deflection case and δ_R is mirror self-weight deflection in radial deflection case, the mirror self-weight deflection in units of the flexural rigidity when the gravity vector is at an angle θ to the mirror axis is given by Equation (3.3).

$$\delta_\theta = \sqrt{(\delta_A \cos\theta)^2 + (\delta_R \sin\theta)^2} \tag{3.3}$$

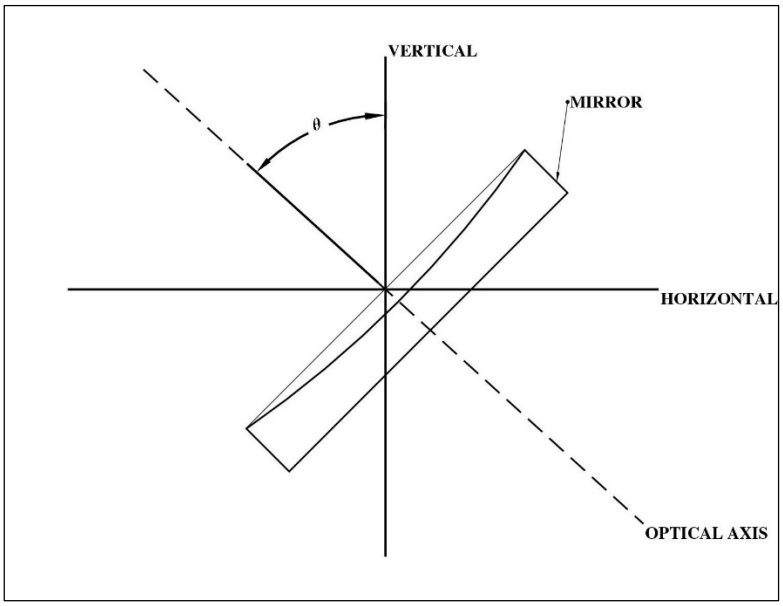

Figure 3-3: Mirror subjected to deflection at an arbitrary angle (Adapted from (Vukobratovich and Vukobratovich, 2008).

Axial deflection due to self-weight can be reduced by optimizing the mirror support in this direction with regard to the weight per unit area of the mirror. The lightweight of the mirror increases flexural rigidity of the mirror, thereby reducing axial deflections due to self-weight. The axial deflection is highly dependent on the mass of the mirror, the mechanical properties of the mirror as well as the support structure, through the following Equation(3.4):

$$\delta_A = C\left[\frac{\rho}{E}\right]V_o \Big/ I_o \, r^4(1-\nu^2) \tag{3.4}$$

Where δ_A represents the axial deflection due to self-weight in metric units, C is the support condition constant, ρ is mass density of mirror material, E is the elastic modulus of mirror material, V_0 being the unit volume of mirror, I_0 being the unit cross-sectional moment of inertia, r representing the mirror radius in metric units and v as the Poisson's ratio of mirror material.

3.6 Structural analysis of optics

An optical structure's performance is usually determined by distortions or displacements. The purpose of structural analysis is to predict the behaviour of optical structures to the level of their performance specifications (Genberg, 1999). Structural analysis is usually used in the early in the mirror design process in determining allowable conditions evaluate various mounting concepts and provide initial optical performance for assumed thermal environments. The analyses will serve to minimize weight mirror design to ensure that it is able to meet all its performance criteria and increase the overall performance of the optical system.

3.6.1 Finite element analysis

In order to predict reliable mirror performance characteristics, an accurate finite element model is essential. The purpose of Finite Element Analysis is to numerically analyse a complex system into small discrete variables whose performance can be modelled simply. The deformations experienced by mirrors under gravity are considered extremely small. Small deformations are modelled by linear static structural analysis. The system is modelled as Equation (3.5). Here $[K]$ = stiffness matrix, $\{x\}$ = displacements (of the nodes), $\{F\}$ = the forces (at the nodes).

$$[K]\{x\} = \{F\} \tag{3.5}$$

3.7 Modelling of sandwich honeycomb mirrors

3.7.1 Theory of modelling deformation in sandwich mirrors

Due to high stiffness of sandwich mirrors, it will tend to experience less deformations, not only more than solid mirrors, but also more than other lightweight mirror designs. This is due to the fact that a sandwich mirror places most of its mass on the face and back sheet, with as little mass as possible in the shear core, providing a very efficient structure in bending. Sandwich mirrors are analysed by substituting an equivalent flexural rigidity D into the normal deflection equations. Equation (3.6) gives the flexural rigidity of a lightweight mirror as defined by Vukobratovich (1999), where $D_{SANDWICH}$ given in metric units, represents flexural rigidity of sandwich plate, E being the elastic modulus of plate material , t_b being the equivalent bending thickness of lightweight mirror and v being the Poisson's ratio of plate material.

$$D_{SANDWICH} = \frac{E t_b^{\,3}}{2(1 - v^2)} \tag{3.6}$$

The equivalent bending thickness is given by Equation (3.7), where t_F is the face sheet thickness of the honeycomb structure, h_c being the rib height, and η being the rib solidity ratio given by Equation (3.8).

$$t_b^{\,3} = (2t_F + h_c)^3 - \left(1 - \frac{\eta}{2}\right) h_c^{\,3} \tag{3.7}$$

The rib solidity ratio is a function to the rib thickness t_w and the pocket size or inscribed circle diameter B given by:

$$\eta = \frac{(2B + t_w)t_w}{B + t_w} \tag{3.8}$$

The structural efficiency of a sandwich mirror is given by the ratio V_0/I_0 . This is the ratio of the unit volume of unit cross-sectional moment of inertia and for sandwich mirrors and is written as

$$\frac{V_0}{I_0} = \frac{12(2t_f + \eta h_c)}{t_b^3}. \tag{3.9}$$

The deflections of sandwich structures are made up from bending and shear components. The shear deflection is dependent on the shear modulus of the core. For a sandwich mirror on multiple supports such as the HartRAO LLR primary mirror, the deflection including shear efforts for self-weight deflection is given by Equation (3.10) as thus:

$$\delta = 0.0025\left(\frac{W}{A}\right)\left(\frac{r^4}{D}\right)\left(\frac{3}{n}\right)^2 + 0.65\left(\frac{W}{A}\right)\left(\frac{r^2}{S_C G A_o}\right)\left(\frac{3}{n}\right) \tag{3.10}$$

In this expression, δ represents the peak to peak surface deflection of mirror, W = mirror weight, A = area of mirror, r = radius of mirror, D = flexural rigidity of mirror, n = number of support points, S_c = shear coefficient, G = shear modulus and A_0 = cross-section/unit width. The central hole in the mirror changes the deflection by a factor of 1.67. Equation (3.11) represents the maximum deflection for a mirror with a central hole, where f_1 and f_2 are support constants.

$$\delta_{\max} = (f_1 + f_2)\left(\frac{W_{SANDWICH}}{\pi r_1^2}\right)\left(\frac{r_1^4}{64 D_{SANDWICH}}\right). \tag{3.11}$$

3.7.2 Computer modelling of sandwich mirrors

With the development of finite element software such as ANSYS, modelling sandwich structures has been made simple (Moaveni, 1999). To predict the extremely small deformations of a mirror, a linear static structural analysis is done, limited only to elastic, homogenous isotropic material properties. Choosing the element type is important in the accuracy of the model. A 3D plate model (Figure 3-4) can be chosen to predict the distortions of sandwich mirrors. While this model is more accurate, it is time consuming since it models the core geometry in detail. Extra detail is required around mounts to accurately model mount geometry, adding to the model generation time. The cells might introduce difficulties in meshing leading to inaccuracies. Curvature meshing methods should be applied to improve the mesh quality.

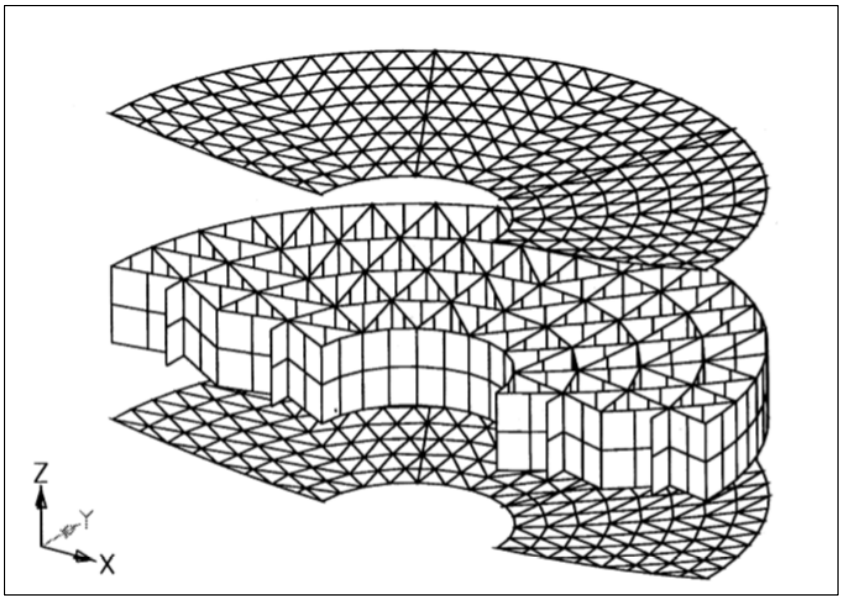

Figure 3-4: Finite element model of a sandwich mirror (Genberg, 1996).

3.8 Modelling of kinematic mounts and whiffle-tree mounts

The figure or surface error of a large mirror is highly dependent on its support system (Vukobratovich, 2008). To counter the gravity effect, the sandwich mirror is supported on a whiffle-tree kinematic mount. Analysis of sandwich mirrors requires careful modelling of the mounts. The mounts help to hold optical components in a way that is repeatable and low in stress. Sandwich mirrors are often difficult to model due to the complex cell geometry. Kinematic methods provide accurate and repeatable mounting of optical components in a low stress condition at much lower costs than conventional mechanical methods (Vukobratovich, 1999).

A whiffle-tree support system is designed to distribute the weight of the mirror across a series of points so that each point pushes on the mirror properly to minimize deformations. The kinematic mount is regarded as the best mount because it fixes six rigid body degrees of a mirror. Kinematic mounts are derived from the principle of constraint of a rigid body which possesses six degrees of freedom in translation and rotation about each of three mutually perpendicular axes. The mirror will still deform in the unsupported regions of the whiffle-tree mount, but by optimizing the number of support points and their position, the deformations can be minimized to less than the functional requirements to produce near theoretical performance (Kumar et al., 2013).

The performance of a whiffle-tree kinematic mount is determined by the number of supports, pivot friction and rocker stiffness. The optimum location for the support points is determined using complex structural analysis methods. In optical mirrors, the support points on

the whiffle-tree are equally spaced in concentric rings as illustrated in Figure 3-5. The RMS of deflection of a mirror supported on N multiple support points can be estimated by Equation (3.12),

$$\delta = (\gamma_n)\left(\frac{\rho h}{D}\right)\left(\frac{\pi r^2}{N}\right)^2\left[1+2\left(\frac{h}{\mu}\right)^2\right], \tag{3.12}$$

where γ is a constant depending on support configurations, ρ = mass density of material, D = flexural rigidity of mirror, r = mirror radius, h = mirror thickness, E = elastic modulus of material and μ = support effective length given by $\mu = r/\sqrt{N}$.

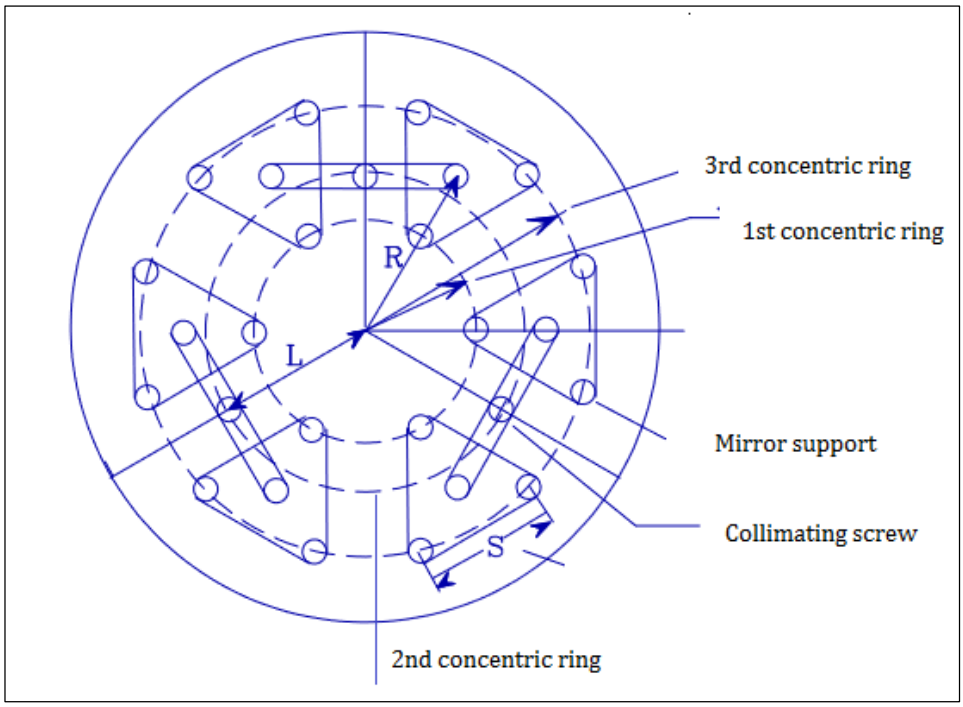

Figure 3-5: Eighteen point whiffle-tree support system.

3.9 Chapter Summary

In this chapter, the properties of the type of mirror design for the HartRAO LLR telescope were discussed. The mirrors fall under a category of lightweight mirrors. This type of mirror design is advantageous in that it reduces the mass of the mirror, thereby minimizing effects of gravitational deformations during ranging. The type of mirror material is equally important in the fundamental requirements for optical mirrors. Both mirror substrates are made from Zerodur glass ceramic. This type of glass is supreme among mirror materials as far as thermal expansion is concerned. In addition, it is highly homogenous and therefore is able to maintain a stable, high precision surface shape. Another aspect which can greatly affect the mirror quality is its support mechanism. The mirrors are mounted on a whiffle-tree kinematic system. Kinematic

mounts are able to assist the mirror in maintaining its surface figure during observations. The chapter also provides some scaling laws used to determine how much deformation is acceptable on a mirror without inducing a change in surface figure. Lastly, the methods on how these deformations can be simulated with computer programs are discussed. Computer programs take the tedious chore of calculating these deformations by manual closed-form techniques.

4

ABERRATIONS AND DIFFRACTION IN REFLECTING TELESCOPES

4.1 Introduction

The quality of an image-forming system is often limited by the presence of aberrations in the optics of the system. Even perfectly designed systems contain aberrations. Optical aberrations are formally defined as the departure of the performance of an optical system from the predictions of paraxial optics causing blurring of the image produced (Schroeder, 2000; Born and Wolf, 1999; Smith, 2000 and Hecht, 2002). This occurs when all the rays from an object fail to converge to a single point. Generally, aberrations are classified into two types i.e. monochromatic and chromatic. For the purposes of this research, only the former will be discussed since they are more prevalent in reflecting telescopes. An aberration-free image serves as reference for perfect image formation and any deviation from this will indicate the presence of aberrations. This chapter contains a discussion of aberrations most present in optical telescopes, laying much emphasis on Cassegrain telescopes. Furthermore, the effect these aberrations have on the image quality of the telescope will be outlined with respect to the concept of diffraction.

4.2 First-order optics

A rotationally symmetric optical system forms a perfect image when all the rays originating from an object point converge to a region called the paraxial region (Schroeder, 2000). The rays in this region make small angles (θ) with respect to the optical axis as shown in Figure 4-1, leading to a paraxial approximation assuming that:

$$\sin\theta \approx \theta$$

$$\tan\theta \approx \theta$$

$$\cos\theta \approx 1$$

This paraxial approximation characterizes an ideal imaging quality of the optical system. Any deviation from this approximation gives rise to aberrations. This system is known as first-order, paraxial or Gaussian optics.

4.3 Third order monochromatic aberrations

By virtue of its name, monochromatic aberrations are present in a single wavelength of light. These aberrations arise due to geometrical deviations from paraxial expectations. In optical

system analysis, only third order monochromatic aberrations are considered. These are, namely: tilt, defocus, spherical aberration, coma, astigmatism, field curvature and distortion. The last five of these aberrations are often called primary or Seidel aberrations after L. Seidel who derived formulae for calculating them in 1856 (Wyant, 1992).

Smith (2000) described primary monochromatic aberrations by specifying the shape of the wavefront emerging from the exit pupil of an optical system. Consider the situation depicted in Figure 4-1 where a ray originates from an object point at $-h$ on the x-axis, passes through the system's aperture stop at position (s, θ) and intercepts the image plane at point (x',y'). The dimensionless radial coordinate s is taken to be unity at the outer boundary of a circular pupil. Using a power series, the wavefront can be expanded to find a solution for position (x',y') as:

$$x' = A_1 s\cos\theta + A_2 h + B_1 s^3\cos\theta + B_2 s^2 h(2+\cos 2\theta) + (3B_3 + B_4)s h^2\cos\theta + B_5 h^3 + \ldots$$
$$y' = A_1 s\sin\theta + B_1 s^3\sin\theta + B_2 s^2 h\sin 2\theta + (B_3 + B_4)s h^2\sin\theta + \ldots$$

Here, A represents the first order terms corresponding to paraxial approximation while B terms represents the primary aberrations. The wavefront expansion can be written in terms of aberration coefficients W_{kmn} :

$$\begin{aligned} W(\mathrm{h},\mathrm{s},\theta) &= \sum_{k,m,n} W_{knm} h^k s^n \cos^m\theta \\ &= W_{200}h^2 + W_{111}hs\cos\theta + W_{020}s^2 + W_{040}s^4 + W_{131}hs^3\cos\theta + W_{222}h^2s^2\cos^2\theta + \\ &\quad W_{220}h^2s^2 + W_{311}h^3 s\cos\theta \end{aligned} \qquad (4.1)$$

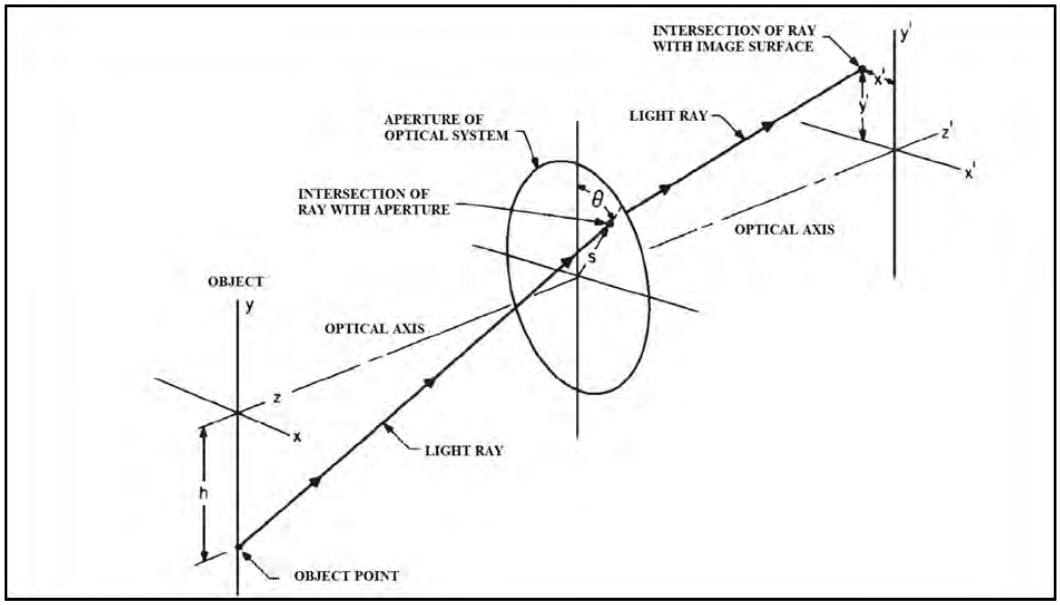

Figure 4-1: A ray from the point, $y = h,\ (x = 0)$ in the object passes through the optical system aperture at a point defined by its polar coordinates (s, θ), and intersects the image surface at (x', y') (Smith, 2000)

4.3.1 Spherical Aberration

Spherical aberration can be defined as the variation of focus with aperture (Fischer, Tadic-Galeb and Yoder, 2008, Smith, 2000). This occurs when the wavefront fails to conform to a sphere resulting in incident light rays not focusing at the same point. The magnitude of spherical aberration in mirrors depends on the height of the ray h. Rays closest to the optical axis focus near the paraxial focus position as depicted in Figure 4-2. The deviation of spherical surfaces from the ideal sphere increases with aperture radius r.

Spherical aberration can be measured either along the optical axis or along the vertical direction. These are referred to as longitudinal and transverse or lateral spherical aberration respectively. The latter is a commonly used measure as it represents the image blur radius of the optical system. Spherical aberration tends to affect the whole field of an optical system, including the vicinity of the optical axis. This makes this aberration the most important of all primary aberrations (Malacara and Malacara, 2004).

Table 4-1: A summary of monochromatic aberrations with their wavefront aberration coefficients (Wyant and Creath, 1992).

Wavefront Aberration Coefficients (W_{knm})	**Functional form**	**Name**
W_{200}	h^2	Piston
W_{111}	$hr\cos\theta$	Tilt
W_{020}	r^2	Focus
W_{040}	r^4	Spherical
W_{131}	$hr^3\cos\theta$	Coma
W_{222}	$h^2r^2\cos^2\theta$	Astigmatism
W_{220}	h^2r^2	Field Curvature
W_{311}	$h^3r\cos\theta$	Distortion

4.3.2 Coma

An optical system with coma causes incident oblique rays passing through the edges to be imaged at different heights. Coma is defined as the variation of magnification with aperture

(Fischer, Tadic-Galeb and Yoder, 2008, Smith, 2000). Each pair of the incident rays converges to small circles which in turn form a comet shaped flare on the image plane as seen in Figure 4-3. The diameters of the circles are proportional to the square of the diameters in the aperture. The height of the comet is defined by the position of the ray that goes through the centre of the aperture stop called the principal or chief ray in the image plane. The linear dependence on object height implies that coma will be small at small field angles.

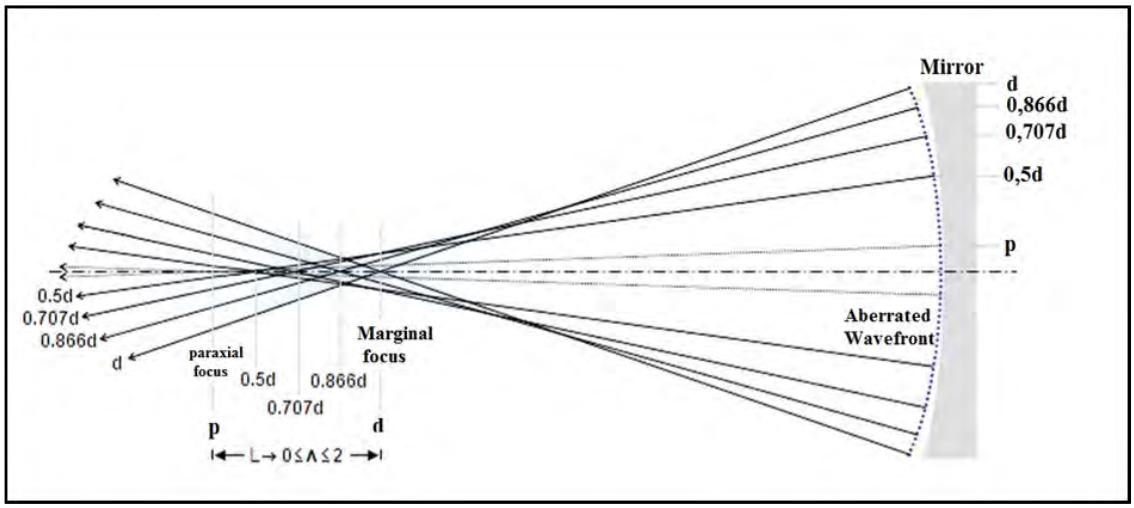

Figure 4-2 **:** Spherical aberration in an optical mirror displaying rays close to the optical axis, in factors of d, focusing close to the paraxial focus p. The distance from the paraxial focus p to the marginal focus d is the longitudinal spherical aberration Λ, normalized to 2 (Sacek, 2006).

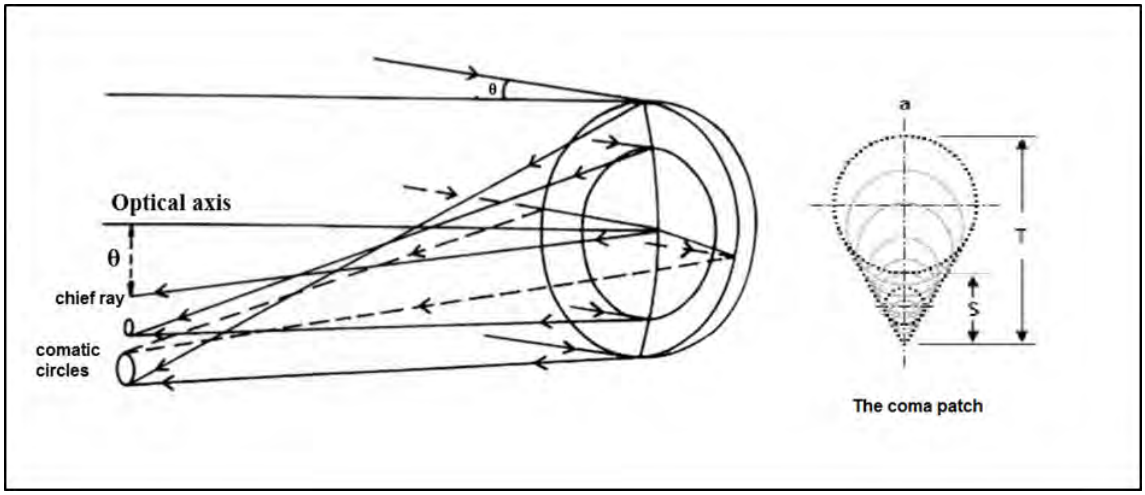

Figure 4-3: Comatic aberration in an optical mirror. Outer edge rays incident on the mirror forms small circles on the image plane which make up at coma patch. The coma in the patch can be measured as sagittal (S) or as tangential (T). (Source: Geary, 1993).

The marginal rays form the largest circle with its centre furthest from the optical axis and chief ray. The reverse is true for the paraxial rays (Geary, 1993). The distance from the chief

ray to the furthest point on the marginal circle is called tangential coma as seen on the right of Figure 4-3. The radius of this circle is the sagittal coma. The sagittal coma is one third as large as the tangential coma. The sagittal coma is a better measure of coma since nearly half of all the energy in the coma patch is contained in this region (Smith, 2000).

4.3.3 Astigmatism

Astigmatism occurs as a result of the tangential and sagittal images not focusing at the same plane. The tangential plane is the plane containing the optical axis, while the sagittal plane is the plane perpendicular to the tangential plane where the principal plane lies. Rays along the tangential plane will focus along a line that lies in the sagittal plane and rays along the sagittal plane will focus along the line that lies in the tangential plane, as depicted in Figure 4-4. Between the astigmatic foci, the image formed is a circular or elliptical blur. There is generally no astigmatism along the optical axis. It will however become more significant the further an image point moves away from the optical axis. Astigmatism is proportional to the square of the object height h as seen in Equation (4.1).

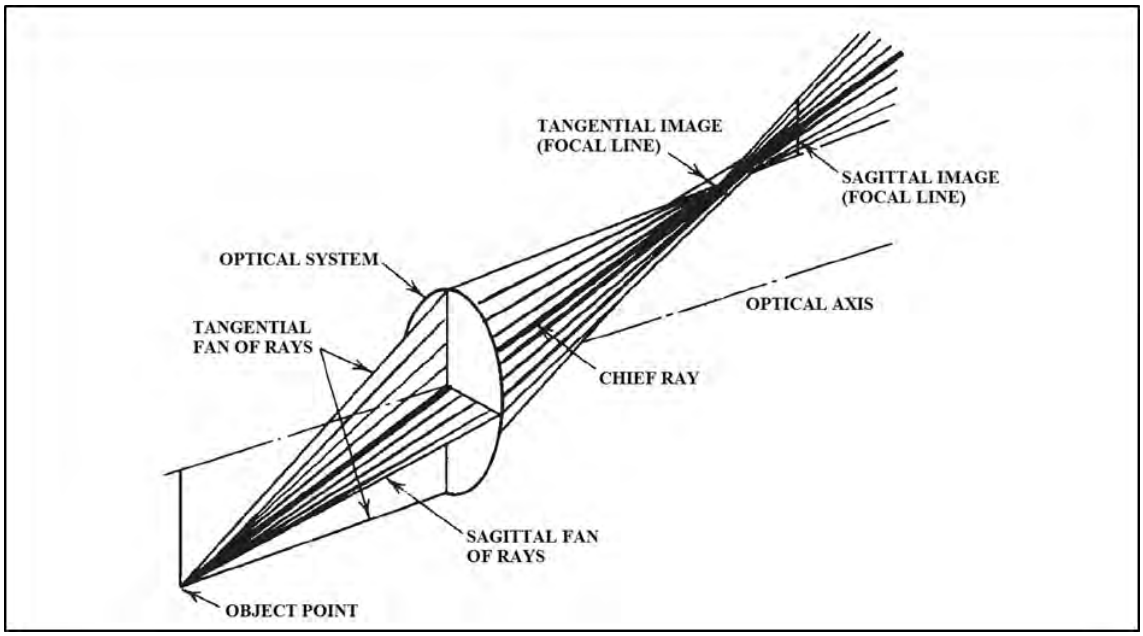

Figure 4-4: Astigmatism in an optical surface. Incident tangential and sagittal rays focus on different planes. The tangential rays come to focus along the sagittal focal line and vice-versa (Smith, 2000).

4.3.4 Field curvature

Field curvature is often grouped with astigmatism because they have the same functional form. Smith (2000) defines field curvature as the longitudinal departure of focal surfaces from the ideal. Where there is no astigmatism present, the sagittal and tangential image surfaces lie on the Petzval surface (Figure 4-5). If astigmatism is present, these images lie on a curved surface,

which is paraboloid in shape. In the latter case, the tangential image surface lies three times as far from the Petzval surface as the sagittal image surface as illustrated in Figure 4-5. The result is a flat object surface being imaged into a curved surface rather than a plane.

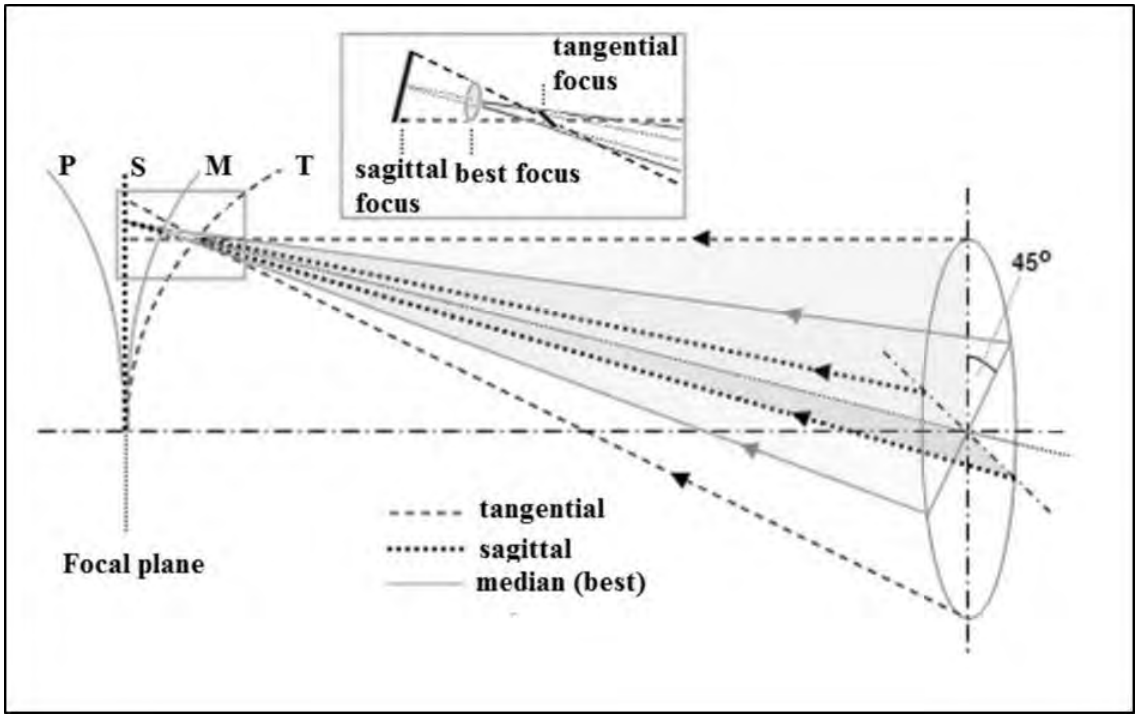

Figure 4-5: An illustration of field curvature in an optical system with no astigmatism. The sagittal (S) and tangential (T) images coincide with each other and they coincide with the Petzval (P) surface and astigmatic foci or best focus (M) (Sacek, 2006).

4.3.5 Distortion

The image of an off axis point is said to be distorted when it is formed either farther or closer to the axis than the image height given by the paraxial expression. An optical system with no other aberrations except distortion will result in a perfect image displaced from its paraxial position (Fischer, Tadic-Galeb and Yoder, 2008). Distortion is the only aberration that does not result in blurring of the image. The amount of distortion is directly proportional to the image size.

Two types of distortions generally exist. There are illustrated in Figure 4-6. When the distortion is such that the perimeter of the image is magnified more than the centre of the image, the distortion is referred to as positive or pincushion distortion. The opposite distortion where the centre of the image is magnified more than the perimeter, the distortion is referred to as negative or barrel distortion (Smith, 2000). The amount of distortion is the measure of the displacement of the image from the paraxial position. It is expressed either directly or as a percentage of the ideal image height, which for an object located at infinity, can be given by $y = f \tan\theta$.

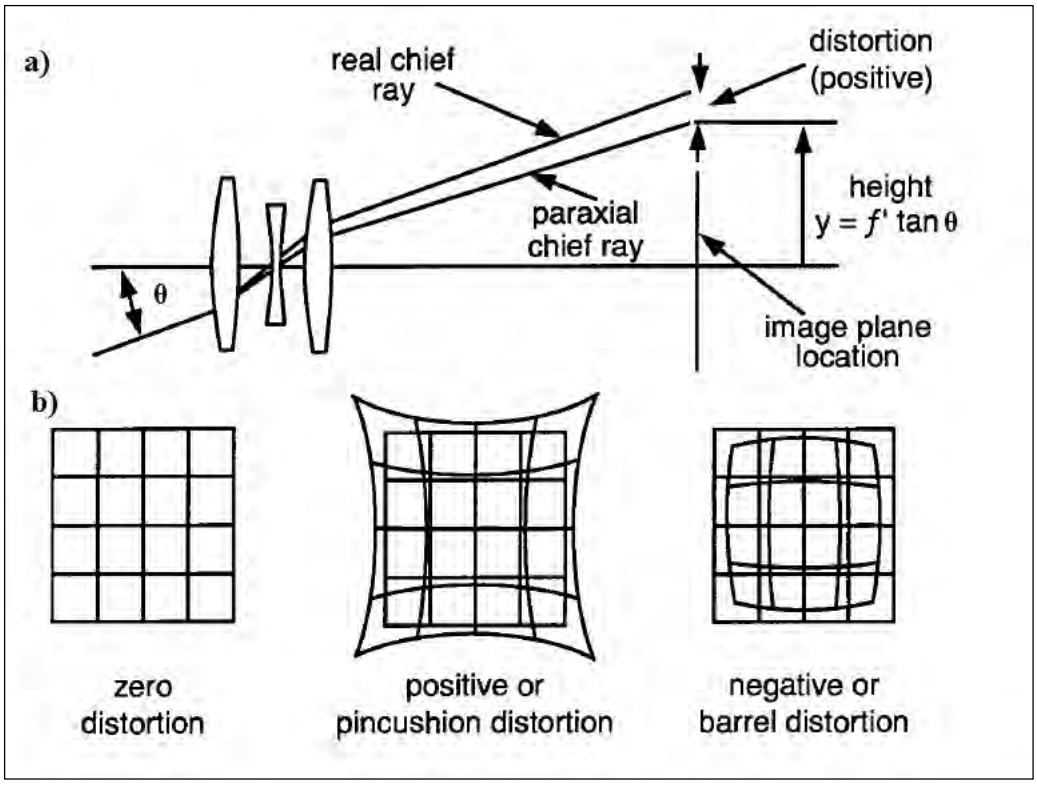

Figure 4-6: Illustration of distortion in an optical system; a) The distortion or displacement of image from its paraxial position is expressed as a percentage of the ideal image height, b) An illustration of pincushion and barrel distortion (Fischer, Tadic-Galeb and Yoder, 2008).

4.4 Diffraction in Optical Systems

In the previous section, it was discussed how geometrical aberrations affect the image quality of a telescope. Aberrations, however, are not the only factor which has an effect on the overall performance of an optical system. In addition to atmospheric turbulence, diffraction can cause the images of a telescope to be blurred. Ideally, in the absence of atmospheric turbulence and aberrations, light from a point source converges to the minimum spot size called the Airy disk. The Airy disk has a Gaussian intensity function profile surrounded by low intensity distribution circles. When this is the case, the telescope is said to be diffraction limited (Fischer, Tadic-Galeb and Yoder, 2008). Diffraction is caused when light is restricted in the entrance aperture of the telescope. The Airy disk represents the maximum of the diffraction pattern and is the smallest point to which a light beam can be focussed. Nearly 84% of the light is concentrated at the Airy disk.

4.4.1 Diffraction images with aberrations and other telescope defects

Aberrations cause the image of the point source to be rather a pattern of energy distribution causing the central spot to spread out and surrounded by concentric rings instead of a point. The resulting aberrated image of the point source will have a unique characteristic structure in the pattern intensity distribution. The brightness of the pattern is dependent on the sizes of the light

source and the aperture. Figure 4-8 is an illustration of diffraction images resulting from primary aberrations.

In addition to aberrations, certain imperfections and obstructions in the optics of the telescope have an effect on its diffraction pattern. Error sources most common in telescope optics include central obstruction, zones, and rough optical surfaces, turned down edges, pinched optics, tube currents and turbulence. The presence of these errors is indicated as such:

i. Central obstructions

Any obstruction placed in the light path of a telescope prevents some portion of light from reaching the focal point. Its effect on the diffraction pattern depends on the size of the obstruction as illustrated in Figure 4-7. Though the presence of a secondary mirror degrades the optical quality to some small extent, the appearance of an image with no aberrations is the same as for good optics (Suiter, 1994). An obstruction of less than 20% can be deemed negligible as its effect on the diffraction pattern is not noticeable to the human eye. At 30% obstruction, the diffraction pattern will result in fewer dips in intensity across the disk.

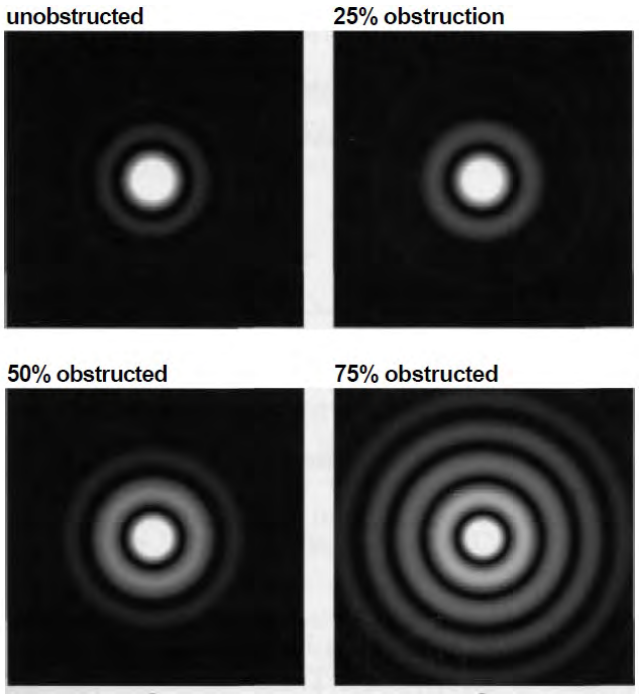

Figure 4-7: Diffraction patterns resulting from different obstruction sizes. The central energy becomes distributed on other rings as obstruction size increases.

ii. Rough Optical Surfaces

This defect lessens contrast between the rings on the diffraction pattern. In this case, light from the central spot looks scattered towards the outer rings, thereby producing spiky appendages to the rings. Rough surfaces are a result of rapid polishing materials and/or in Figure 4-9 sufficient

contact between the pitch polishing lap and the optical surface. A smooth surface should produce an image such as that shown on the right of figure 4-9.

Primary aberration	Energy distribution pattern		
	Inside of focus	In focus	Outside of focus
a) Aberration-free			
b) Spherical aberration	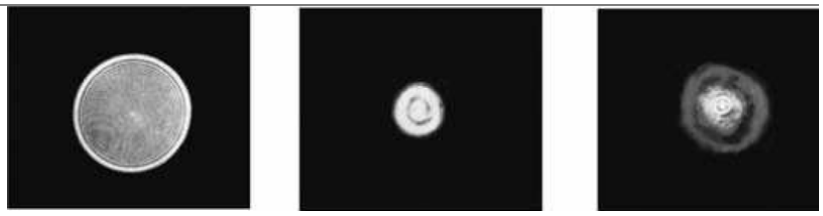		
c) Coma	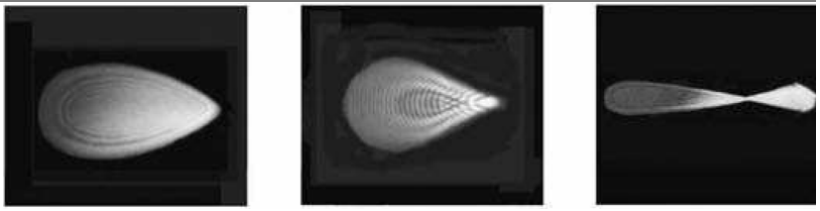		
d) Astigmatism	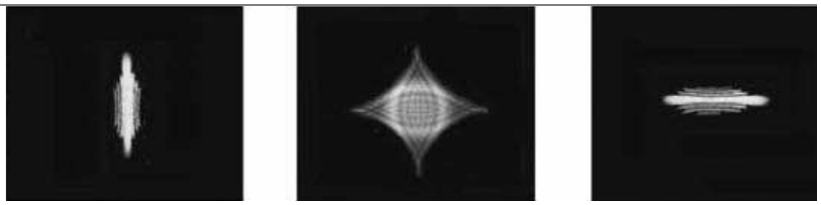		

Figure 4-8: Pattern intensity distribution of primary aberrations in a telescope with images taken inside, outside and in focus. a) An aberration- free (diffraction-limited) telescope produces images with fairly uniformly illuminated disks which appear the same at similar distances inside and outside of focus. b) Spherical aberration results in the pattern of the image to look fuzzy on side of focus and defined on the other. c) The comet shaped image resulting from coma aberration. d) The images taken inside and outside of focus illustrate how the images appear on and along the sagittal and tangential planes respectively when astigmatism is present (Malacara, 2007 and Suiter, 1994).

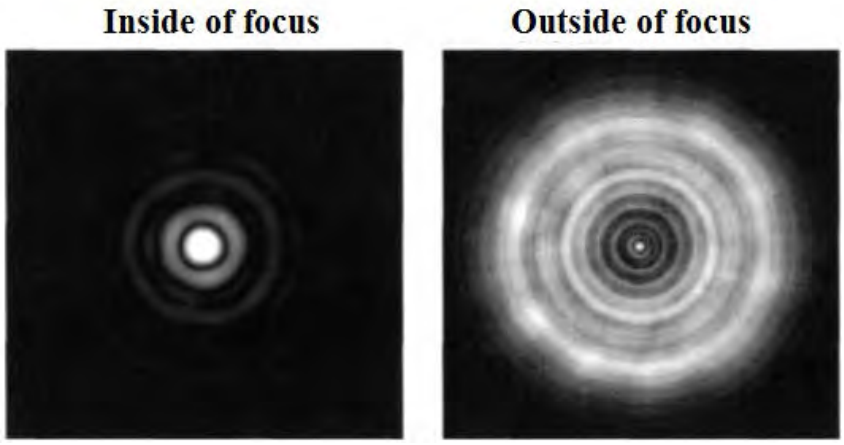

Figure 4-9: Rough optical surfaces images in and out of focus. The pattern will depend on the scale of roughness, as well as its graininess and periodicity (Suiter, 1994).

iii. Turned down edges

During mirror manufacturing, it is possible to place too much pressure when polishing the telescope mirror, which can result in the mirror edges to bend. This effect causes the image pattern to appear as a diffuse glow which spreads out over the field of view inside focus. Less contrast can be seen between the rings. When outside of focus, however, the contrast between the rings is increased as observed in Figure 4-10. Turned down edges can be minimized by blackening of the edges so that there is no reflection from that portion of the mirror.

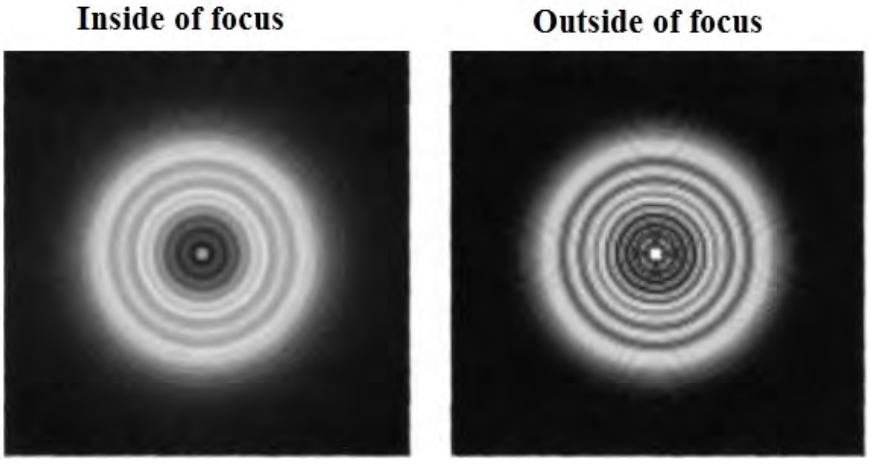

Figure 4-10: Diffraction image from a telescope with a turned down edge. The contrast is less on the inside of focus pattern and is increased on the out of focus pattern (Suiter, 1994).

iv. Pinched optics

Any mechanical stress on the optical elements may lead to deformation of the optics. This occurs when either the clips are fastened too tight or the mirror is inadequately supported, thereby subjecting it to gravitational effects. Diffraction images inside and outside of focus will have near perfect 3 sided symmetry as portrayed in Figure 4-11.

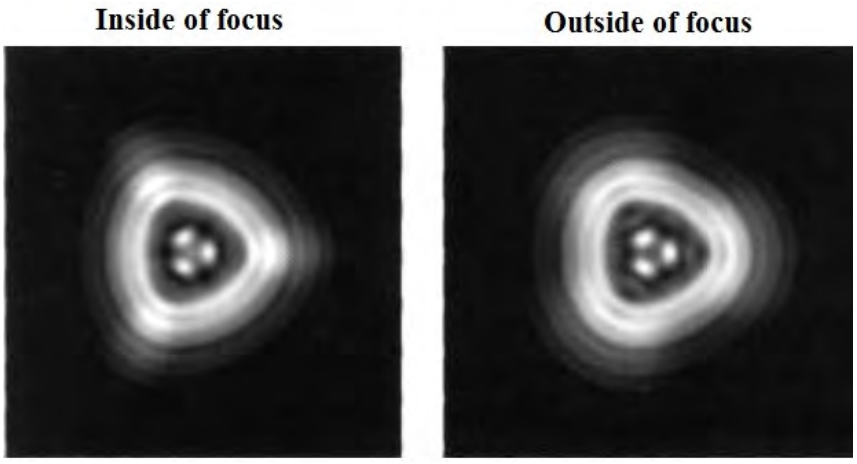

Figure 4-11: Diffraction pattern of a telescope with deformed optics showing a three lobed pattern as a result of clips being too tight taken inside and outside of focus (Suiter, 1994).

v. Tube currents

Changes in temperature inside the telescope tube can cause thermal inertia leading to tube currents. During tracking, the tube tilts up from horizon to zenith. Since hot air is less dense than cold air, it will accumulate at the top of the tube while cold denser air will descend towards the bottom of the tube. Figure 4-12 shows evidence of these temperature differentials on the diffraction pattern. The intensity inside of focus is higher, with partial brightening of the rings.

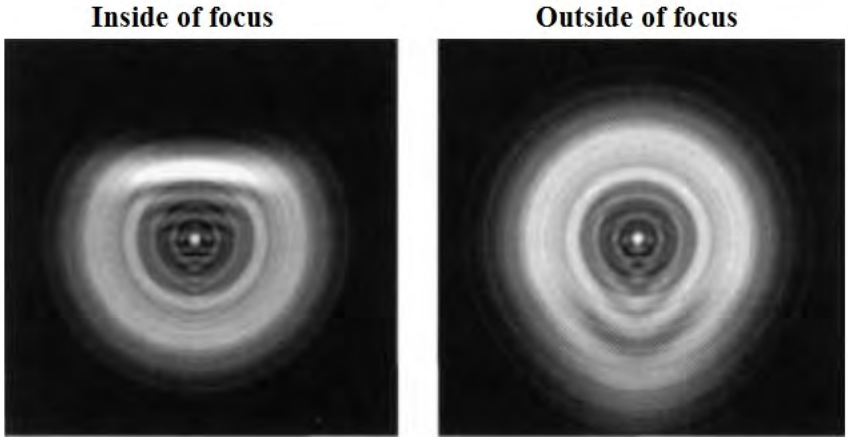

Figure 4-12: Image degradation as a result of different currents inside the telescope tube. The intensity seems to increase in the direction of air flow when observing inside of focus (Suiter, 1994).

vi. Atmospheric turbulence

Atmospheric turbulence is not a direct consequence of the telescope optics, but has a significant effect on the image quality. Large inhomogeneities of the atmosphere cause the index of refraction to vary and produce wavefront distortions in the light coming from the stars. This

leads to a blurring of images. Images taken inside and outside of focus show a slight spreading of the light, which appears like a twinkle as seen in Figure 4-13.

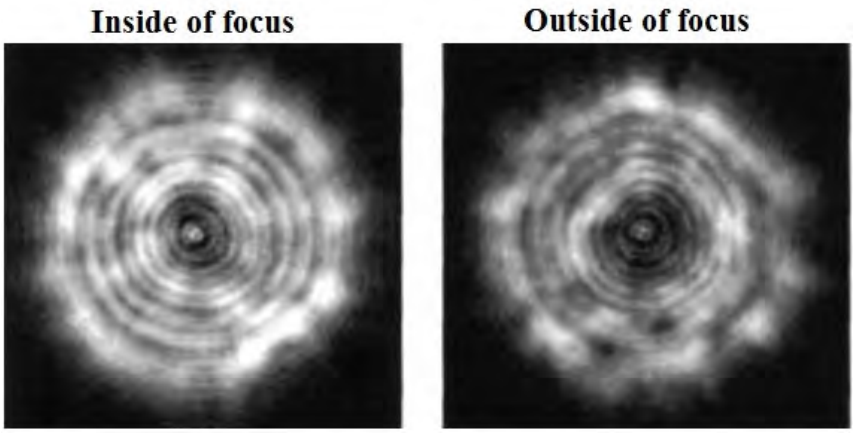

Figure 4-13: Star images taken when there is turbulence in the atmosphere. The diffraction pattern is degraded by the changing inhomogeneities of the atmosphere. This causes the images to 'twinkle' (Suiter, 1994).

4.5 Chapter Summary

The image quality of optical telescopes is often reduced by the presence of geometrical and diffraction effects. This chapter provided a detailed explanation on what aberrations are and how they affect image quality of a telescope. To begin with, the types of aberrations commonly present in Cassegrain systems are discussed. Furthermore, it was shown how these aberrations can be identified on intensity distribution patterns. Other common defects which cause diffraction in telescopic images are also discussed, with atmospheric turbulence being the most prevalent of these.

5
METHODS

5.1 Introduction

One of the refurbishment stages of the LLR telescope subsystem would be to define its optical characteristics and to supplement the complete optical train with additional optical components to facilitate transmission of the laser beam. No details of the optical characteristics of the telescope exist so some tests will have to be done in order to determine the characteristics of the system, the quality of the optics and the optical path of the laser beam. The telescope is a 1 m Cassegrain with parabolic primary mirror and a hyperbolic secondary mirror with a convex surface. In this kind of system, light is reflected back through a hole in the primary mirror onto the detector package. This requires determination of the exact focal point and optics required to produce a flat field image.

The following experimental procedures will be explained in detail:

- The procedures followed in the mirror cleaning process.
- A design of the coudé optical path and choice of coudé components.
- Calculations and characterization of the specifications of the optical system
- Measurement and calculation of transmission efficiency with a spectrometer.
- Image quality analysis of the telescope by studying its aberrations, spot diagram and Point Spread Function with OSLO optical analysis software.
- Finite Element Analysis of the primary mirror and its support structure with ANSYS software to determine distortions due to gravitational effects. Taking into account the mirror weight, thickness and glass type, we can determine the deformation error of the mirrors and see how that affects the image quality of the telescope.

5.2 Mirror cleaning

The 1 m Cassegrain telescope previously operated by OCA for SLR was donated to HartRAO for conversion into an S/LLR system in South Africa. During laser ranging, the telescope is pointed towards the sky thereby exposing it to dust and other particles, reducing the reflectivity of the mirrors, limiting the efficiency of observations. In his study of optical performance of large ground-based telescopes, Dierickx (1992) revealed a direct relationship between the detection capabilities of a telescope and the cleanliness and efficiency of the coatings. In order to restore the reflectivity, mirror surfaces have to be cleaned and aluminized from time to time. The process of mirror cleaning is a delicate one since the mirror is vulnerable to damage which cannot be repaired. Care must be taken to ensure that the optical surfaces are not over cleaned.

Several techniques were employed during the attempt to remove the mirror's aluminium coating from the mirror substrate. With no knowledge of whether the coating was protected and if so, with what elements, it was then assumed that the mirror was coated with just bare aluminium. Under this assumption, potassium hydroxide was first used with distilled water. When this method failed, ferric chloride was used which removed only a small part of the coating. Lastly, hydrochloric acid with copper sulphate ('Green river') solution was used.

5.2.1 Condition of Mirror before cleaning and re-aluminising

The telescope had not been used in over a decade which has led to the mirror accumulating a thick layer of dust and dirt. This was cleaned and the state of the mirror assessed. In addition to dirt, the mirror aluminium coating has peeled off, mostly towards the centre of the mirror and a little on one edge of the mirror as can be seen in Figure 5-1.

Figure 5-1: Condition of 1-m primary mirror prior to cleaning.

The first step was to determine whether it was necessary to recoat the mirror. Optical experts do not recommend cleaning and recoating of large optical mirrors as this is risky and exposes them to damage during handling. A visual inspection of the coating was done by illuminating the mirror from behind with an LED light source. Figure 5-2 is a representation of the images taken during the inspection illustrating the extent of coat degradation. The coating dismally failed this test as the amount of degradation on the coating was large and therefore would reduce the quality of images of the optical system. The coating had to be stripped and the mirror recoated.

Figure 5-2: Degraded coating on primary mirror.

5.2.2 Cleaning and removing old coat

The mirror was placed on firm supporting stands in a low temperature and dust-free room to await cleaning and stripping. The cleaner wore protective gloves and removed any jewellery which could cause damage to the mirror surface. The process to clean and remove coating is as follows:

Figure 5-3: Primary mirror rinsing.

Remove all dust and solid particles from the surface with a water hose under moderate water pressure as illustrated in Figure 5-3. The whole surface was rinsed for a period of 20 -25 minutes. The mirror should not be touched during this process.

The first attempt to remove the aluminium coating was with a solution of caustic soda made by dissolving 10 -15 % of caustic soda pellets to 5 litres distilled water. The mirror was fully covered with pure cotton wool to keep the solution from running off. The solution was poured on the cotton covered mirror and left for 20 minutes. Due to the protective coating over the aluminium, the solution was unsuccessful in removing the coating.

Following the failure of the potassium hydroxide, an acidic ferric chloride chemical reagent was used. Ferric chloride has an exothermic reaction to aluminium without causing any damage to the glass substrate of the mirror. The entire mirror was saturated with the acid and left for a couple of hours to react as seen in Figure 5-4. Although the process was slow, the ferric chloride is the only solution which managed to remove the aluminium coating.

Figure 5-4: Ferric chloride being poured on mirror surface.

5.3 Coudé Path design

The word ‘coudé’ is French for elbow, commonly used to describe a system of bending light via transport optics to a stationary location. In the words of Kuglar (2009), “The most powerful laser in the world cannot work without an effective, finely tuned beam delivery system”. The

type of design is contingent on the application. In Lunar Laser Ranging, for a high transmission efficiency to be achieved, the optical components chosen for the coudé path should be of the correct specification and highest precision. Components (Figure 5-6) were chosen to ensure minimal loss of light for the integrated system.

The optical path will consist of a set of connecting tubes and relay mirrors to direct the laser beam from the laser table into and through the telescope as illustrated in Figure 5-5. The design should be a good compromise between efficiency, image quality and cost. Reflection and transmission losses will affect the throughput of the mirrors and hence should be carefully monitored. Furthermore, the coating on the mirrors should have a reflective efficiency of 98 - 99% at a wavelength of 532 nm with an energy handling capacity of at least 100 mJ and a flatness of about $1/10^{th}$ of a wavelength. In addition, sensors will be installed throughout the path to monitor parameters such as temperature, pressure and humidity. The properties and specifications of all components chosen are listed in Table 5-1.

5.3.1 Optical path layout

Two configurations are considered for transmitting the laser for Lunar Laser Ranging. The paths are illustrated in Figure 5-7. The first option would be to transmit the laser through the beam expander. While this option can be suitable for SLR, it might not be ideal for LLR due to the divergence of the laser beam. The second option will be to transmit through the full aperture of the telescope. Transmitting through a larger aperture will minimize divergence and maximize the number of photons returned.

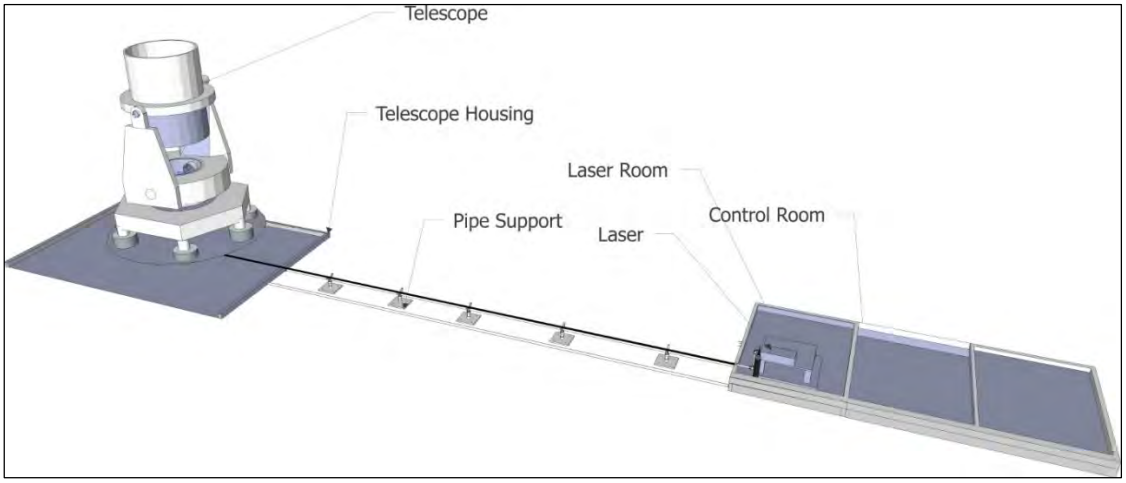

Figure 5-5: Optical coudé path components for transmitting laser signal.

In the first case, relay mirrors and connecting aluminium tubes will be used to direct the laser light from the laser table, into and through the beam expander. The coudé mirrors supplied by Thorlabs Inc., were polished to a flatness of λ/10 and reflects approximately 99% at 532 nm.

One of the mirrors is highly reflective in the near infrared region of the spectrum and high transmission at our operation wavelength of 532 nm.

In the second option, the laser light will be reflected from M_4, towards a coudé mirror which will be installed inside the telescope tube to reflect light to the secondary mirror. The secondary mirror will then reflect the light towards the primary mirror, where it will further be reflected towards the exit of the tube as illustrated by path B. The choice of the optical path to be used will depend on many factors, such as photon return rate, system efficiency and cost.

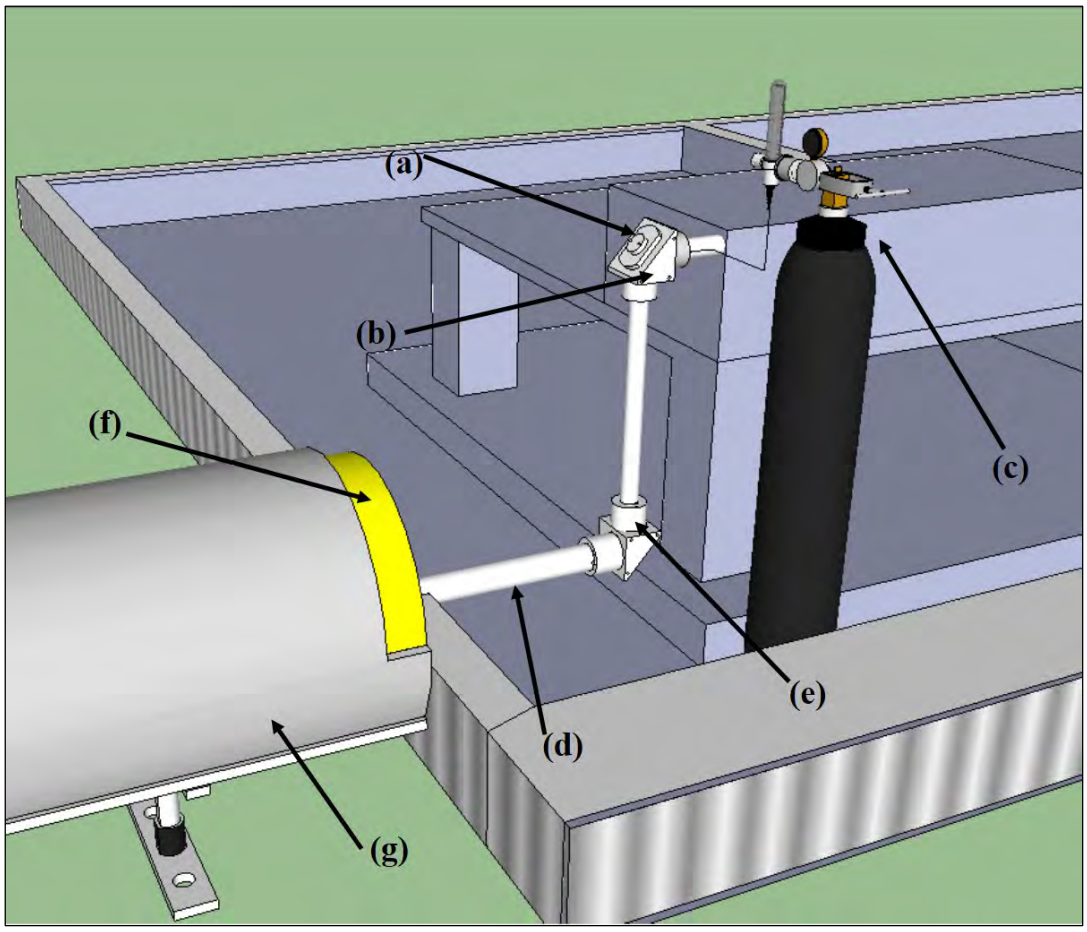

Figure 5-6: Coudé components from laser side of optical path. The component specifications are listed in Table 5-1.

5.3.2 Coudé transmission efficiency

The telescope transmission efficiency is a measure of the amount of light which reaches the final focus, compared to the light that leaves the laser. However, several factors can lead to losses in light as the light travels through its optical path. These factors include reflection efficiency of mirrors, obstructions and light absorption by certain coudé optics.

Losses due to reflections occur on a mirror surface. The amount of light lost in each reflection depends on the type and cleanliness of the coating. The primary and secondary mirrors are coated with aluminium and protected with magnesium fluoride. According to optical coating experts (Sacek, 2006), fresh aluminium coatings leads to losses of approximately 10% in the visible spectrum. More advanced MgF_2 coatings are anti-reflective, thereby eliminating any loss possibilities. The dielectric reflective coatings on the coudé relay mirrors are expected to result in losses of ~ 1% or less for the wavelength of 532 nm.

Table 5-1: Coudé components specifications.

Component	**Specifications**
(a) Dielectric coudé mirrors	Diameter = 50 mm Flatness = λ/10 Reflectivity = 99% @ 532 nm(λ) Peak Power Capability ≥ 1. 25 GW
(b) Mirror Mounts	High precision Kinematic Black anodized aluminium
(c) Dry Nitrogen gas	Purity: 99.5%
(d) Beam delivery tube	Diameter = 65 mm
	Anodized aluminium
(e) Path purge adapters	Diameter = 65 mm
(f) Pipe insulation	Polyethylene Operating temp. Limits: -40 degrees C to +90 degrees C
(g) Protective cover	Galvanized steel

Reflection, together with absorption losses can be expected on the lens elements inside the beam expander. A loss of ~15% due to reflections from the lens surfaces and ~1% due to absorption by the glass are expected.

If transmitting through path B (See figure 5-7), losses due to central obstructions can be expected. This loss is estimated by the surface of the obstruction with respect to the total surface area of the mirror. The 1 m diameter mirror has a total surface area of 0.78 m^2, with an obstructed surface area of 0.71 m^2. Dividing the area of the obstruction by the total area gives a loss of 9%. This is the total expected loss experienced by the mirror due to obscuration.

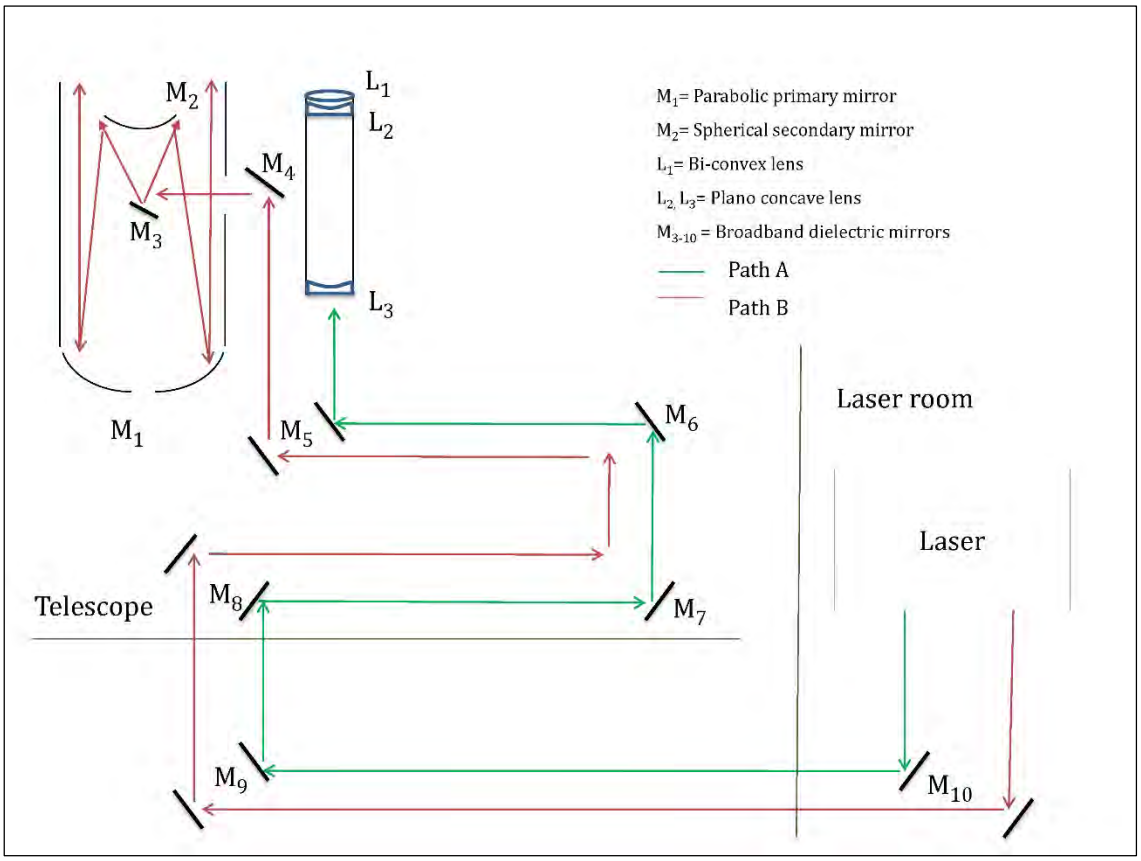

Figure 5-7: Schematic diagram of optical coudé paths where M represents dielectric mirrors and L represents lenses.

5.3.3 Instrumentation and experimental procedure

To obtain reflection and transmission measurements, an Ocean Optics HB4000 fibre optic spectrometer, together with an HL-2000 HPSA high power tungsten halogen light source were used. The spectrometer was configured with a custom grating with best efficiency and resolution of ±0.2 nm in the spectral range between 350 nm and 850 nm. It is equipped with standard SMA-905 connectors drilled for fibre core sizes between 200 µm and 600 µm. The optical bench entrance aperture has a 5 micron width slit installed to achieve the best optical resolution. The spectrometer was connected to a computer utilising Spectrasuite software.

a) Reflection measurements

In order to evaluate the optical coating materials of the mirrors, their reflectance in the visible spectrum range, with special attention applied at 532 nm, were measured. There are generally two techniques used to measure the reflectance of coated optical surfaces with a spectrometer; these being relative and absolute reflectance measurements. The choice of which technique to use depends on the type of coating material and the texture of the surface. Relative reflectance measurements require the use of a reference standard of known reflectance, while absolute reflectance measurements use a device called an integrating sphere which is able to establish a baseline within itself without the use of a standard. Here the former technique was applied. The reflectance of the standard was taken to be 100% and the reflectance of the sample with respect to this reference was determined. Figure 5-8 and Figure 5-9 illustrate the reference standard and sample respectively, together with their respective specifications. Using a tungsten halogen light source and a premium 400 µm reflection probe for illumination, the reference and dark or background spectra were first recorded. The reflectances of the mirrors were then taken with respect to the reference. The complete measurement setup is illustrated in Figure 5-10.

Specifications:

Reflectance material - Front surface-protected aluminium mirror on fused silica substrate

Reflectivity - 200 – 1000 nm: ~87 – 93%

1000 – 2500 nm: ~93 – 98%

Figure 5-8: STAN-SSH reflection standard (source: http://oceanoptics.com/)

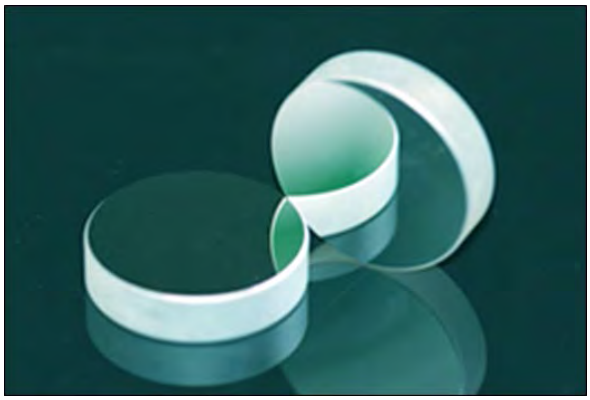

Specifications:

Reflectance material – Broadband HR, dielectric on fused silica substrate

Reflectivity – 400 – 750 nm: ~99%

Figure 5-9: Dielectric mirrors in optical coudé path

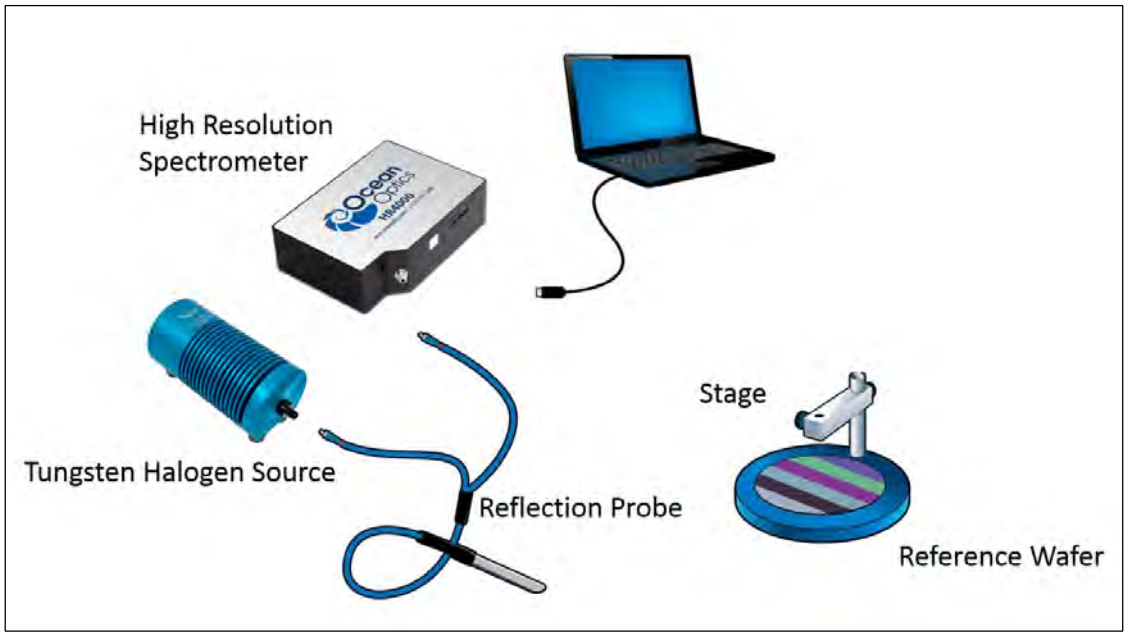

Figure 5-10: Pictorial representation of test setup for reflection measurements (Source: Ocean Optics, 2009)

b) Transmission measurements

As with reflectance measurements, relative transmission was used to measure the transmission of light in the beam expander. In this case, air was used as a reference since it transmits 100% light. Input and output optical fibres with silica core diameters of 200 µm and 600 µm were used for transmission measurements of the lens elements. Collimating lenses were used along with the optical fibres to prevent the light from dispersing, thereby ensuring efficient transmission and collection of signal. The collimating lenses had to be properly aligned before measurements to ensure that the light is properly collimated. Transmittance of the 200 mm doublet (bi-convex + plano-concave) and 76 mm plano-concave lenses were obtained. These lenses are displayed in Figure 5-11 and Figure 5-12 respectively. The whole setup for conducting transmission measurements is displayed in Figure 5-13. The Spectrasuite software computes the transmission measurements of the lenses using the following formula:

$$\%T = \left[\left(S_\lambda - D_\lambda \right) / \left(R_\lambda - D_\lambda \right) \right] \times 100\% \quad (5.1)$$

Where:

S_λ = Sample intensity at wavelength λ

D_λ = Background intensity at wavelength λ

R_λ = Reference intensity at wavelength λ

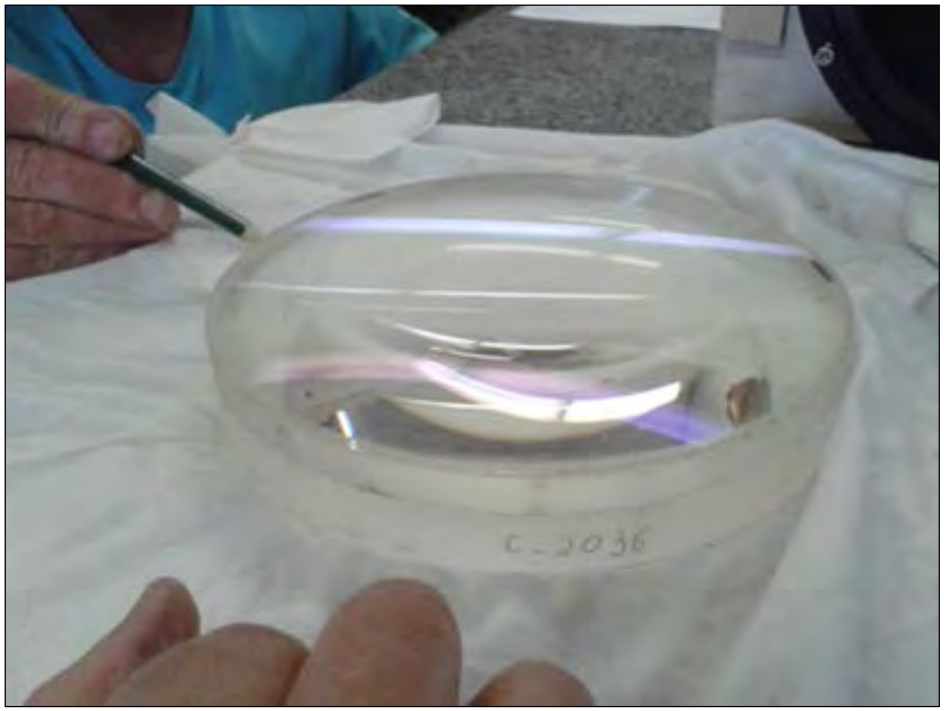

Figure 5-11: Achromatic doublet of HartRAO LLR's beam expander.

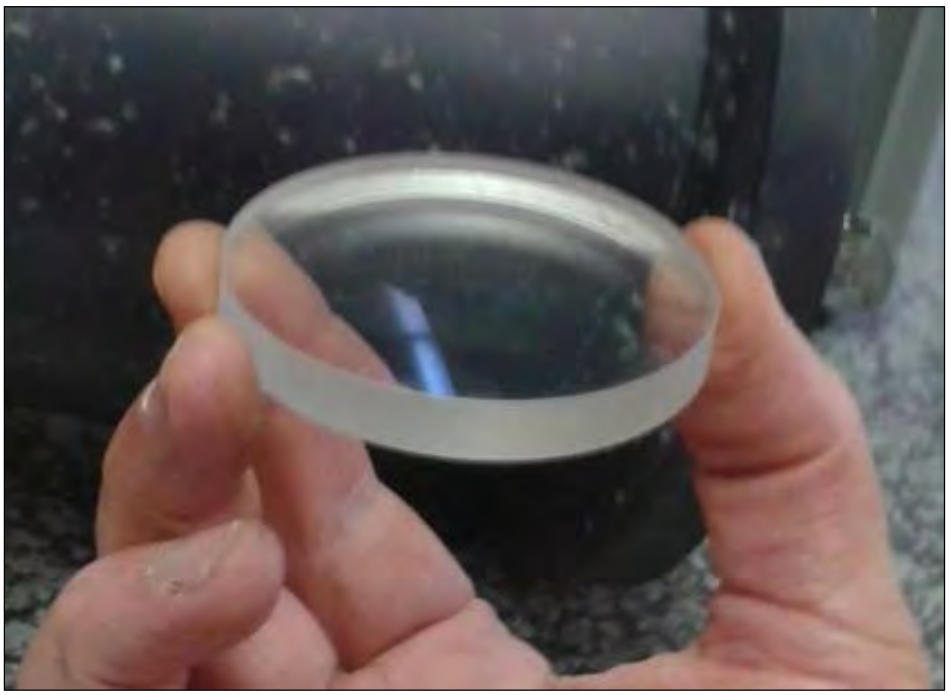

Figure 5-12 Plano-concave objective lens for HartRAO LLR's beam expander.

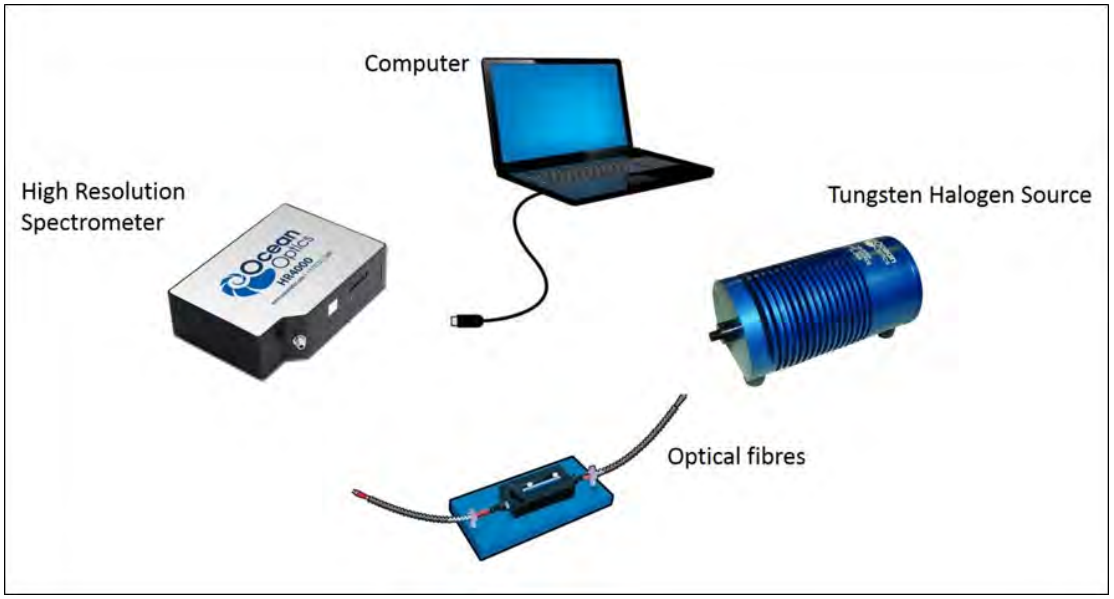

Figure 5-13: Illustration of test setup for transmission measurements (Source: Ocean Optics, 2009).

5.4 Determination of Cassegrain telescope parameters

The first step in evaluating the performance of a telescope is determining its optical design parameters. Basic parameters such as the primary mirror diameter and its focal ratio can easily be measured. From thereon, using standard Cassegrain equations, all other parameters can be calculated. Figure 5-14 illustrates the configuration of a Cassegrain design. All equations are based on paraxial approximation. As explained in section 4.2, paraxial approximation explains how light propagates along an optical system when rays are close to the optical axis.

The signs of the focal lengths, radii of curvature, distances from the principal planes to both objects and images are determined by a local Cartesian coordinate system where the z axis is along the direction of the optical axis which is positive in the direction of incident light.

The most important parameters are the following:

Diameter of the primary D_1

Diameter of secondary D_2

Focal length of the primary f_1

Primary-secondary separation s

System focal point to secondary distance i'

Primary mirror surface to focal plane distance e

Back focal distance B

The distance from the secondary surface to the focal point of the primary i

Magnification m

System focal length F

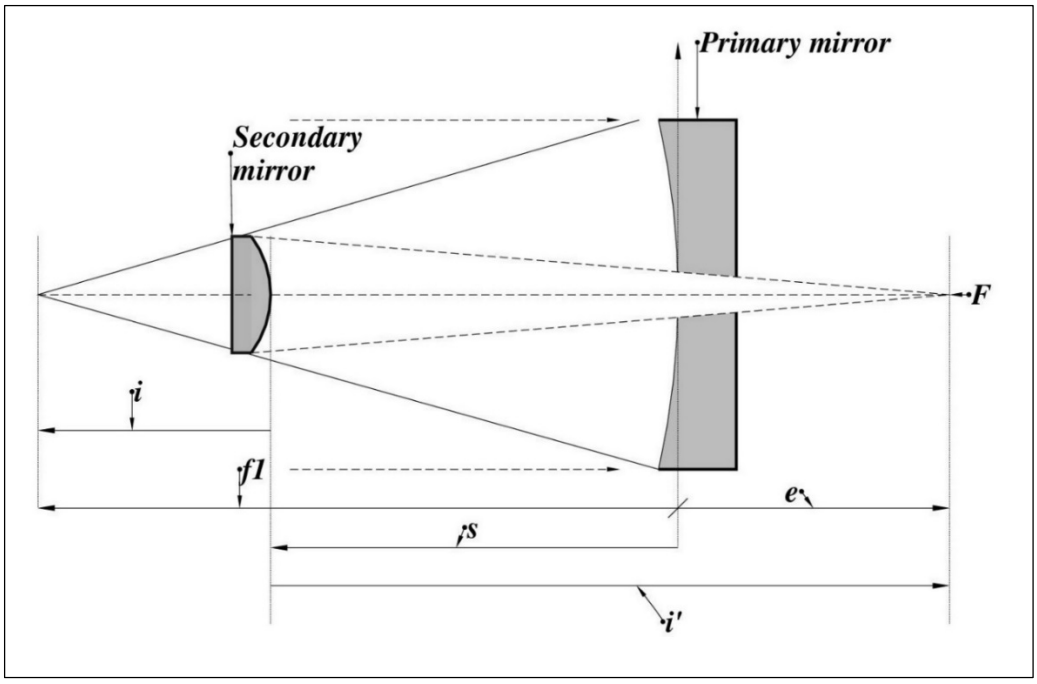

Figure 5-14: Main parameters of a Cassegrain telescope. The sign of the parameters are determined by their direction, which is positive in direction of incoming light and upward from the axis.

The Cassegrain equations used to calculate the parameters were referenced from Texereau (1957) and Andersen and Enmark (2011). The secondary mirror serves to magnify the image formed by the primary mirror. This magnification is given by Equation (5.2):

$$m = \frac{i'}{i} \tag{5.2}$$

Where i' and i are easily measured with classic distance measurement methods. The secondary mirror focal length for the minimum secondary size can then be derived from the magnification and the primary focal length resulting in the relationship:

$$f_2 = \frac{f_1}{\left(1 - 1/m\right)} \tag{5.3}$$

The focal length of the entire system is given by:

$$F = f_1 \times m. \tag{5.4}$$

If the separation between the primary and secondary mirror is known, the final system length can also be determined by Equation (5.5):

$$F = \frac{f_1 f_2}{f_1 - f_2 - s} \tag{5.5}$$

Where f_2 = the focal length of the secondary mirror. The diameter of the secondary mirror can be calculated from:

$$D_2 = D_1 \times i / f_1 \tag{5.6}$$

The radius of curvature of the secondary mirror is given by:

$$R_2 = \frac{2mi}{m-1} \tag{5.7}$$

The radii of curvature of the primary and secondary mirror R_1 and R_2 respectively and their corresponding focal lengths f_1 and f_2 are related by Equation (5.8) and Equation (5.9). They are all negative for a classical Cassegrain telescope.

$$f_1 = \frac{R_1}{2} \tag{5.8}$$

$$f_2 = \frac{R_2}{2} \tag{5.9}$$

5.5 Modelling of aberrations in a Cassegrain telescope

The Cassegrain telescope was first mentioned in 1672 by Laurent Cassegrain (King, 1955). It consists of a concave parabolic primary mirror and a convex hyperbolic secondary mirror. This combination of aspheric curves is important for excellent correction and control of off- axis aberrations in visual and photographic astronomy. The type of aberrations specific to any telescope is dependent on the type of conical surfaces it is made of. Paraboloid and hyperboloid surfaces have rotational symmetry and their form can be defined by the constant K , called the Schwarzschild (conic) constant. The conic constant determines the degree of aspherisation of surfaces, needed to avoid excessive aberrations (Andersen and Enmark 2011). The primary mirror is a concave parabolic mirror with conic constant given by

$$K_1 = -1. \tag{5.10}$$

Before aberrations can be modelled, their aberration coefficients S first have to be determined. In this section, the aberration coefficients of the five Seidel aberrations in respect to the classical Cassegrain telescope, will be discussed (Sacek,2006; Schroeder,2000). The general expression for the aberration coefficient for spherical aberration of a mirror surface is given by

$$S = \frac{n\left[K + \left(\frac{m+1}{m-1}\right)^2\right]}{4R^3}. \tag{5.11}$$

Where n represents the index of refraction of the incident medium, K being the mirror conic, m is the magnification and R represents the radius of curvature. This expression was derived from the general surface coefficient for spherical aberration which was first derived by Focke in 1965 (Focke, 1965). For objects at infinity such as stars, the magnification becomes zero and the coefficient then reduces to

$$S_\infty = \frac{n(K+1)}{4R^3}. \tag{5.12}$$

For a general optical surface, the coma aberration coefficient is given in Equation (5.13). This expression is derived based on optical magnification, which is defined as the ratio of image-to-object size. The parameters I and O are the image and object distance respectively, n and n' are the index of incidence and reflection respectively.

$$c = 0.5n^2\left[(1/O) - (1/R)\right]\left[(1/n'I) - (1/nO)\right] \tag{5.13}$$

When the object is located at infinity, the coma aberration coefficient for either a refractive or reflective surface is given by Equation (5.14), where f is the focal length, n is the index of incidence, and n' is the index of reflection/refraction.

$$c = -\frac{n^2}{2n'Rf} \tag{5.14}$$

For a mirror surface, the coma aberration coefficient is no longer a function of the radius of curvature but rather of the magnification. For any object distance, including objects at infinity, the coma coefficient is given as thus:

$$c = -n\frac{m+1}{4(m-1)f^2} \tag{5.15}$$

The parameter m represents transverse image magnification. For distant objects where m = 0, n = 1, the expression reduces to:

$$c = \frac{1}{4f^2} = \frac{1}{R^2}. \tag{5.16}$$

As with all the other aberration coefficients, the coefficient for astigmatism is derived from the aberration coefficient for a general surface given by Equation (5.17), where I and O

are the image and object distances respectively, n and n' are index of incidence and reflection respectively.

$$a = -0.5n^2\left[\left(1/n'I\right)-\left(1/nO\right)\right] \tag{5.17}$$

For a concave mirror such as the HartRAO LLR primary mirror, $n' = -n$, $I = Of/(O - f)$ and, $f = R/2$ the coefficient is then given by Equation (5.18), where R represents the radius of curvature.

$$a_m = n/R \tag{5.18}$$

All Cassegrain telescopes have no distortion, hence the concave mirror has an aberration coefficient equal to zero. Any surface with no astigmatism on the paraxial region will result in a Petzval curvature given by Equation (5.19), where n is the index of incidence is, n' the index of reflection and R is the radius of curvature of the surface.

$$\frac{1}{R_p} = \left(\frac{1}{n'} - \frac{1}{n}\right)\frac{1}{R} \tag{5.19}$$

This radius is independent of object and image distance. A two- mirror telescope has a Petzval curvature given by Equation (5.20), where R_1 and R_2 are the surface radius of curvature for the first and second mirror, respectively.

$$\frac{1}{R_P} = \frac{2}{R_2} - \frac{2}{R_1} \tag{5.20}$$

From these aberration coefficients, the aberrations specific to a Cassegrain telescope can be modelled. The two aberrations most problematic in classical Cassegrain telescopes are coma and astigmatism. Spherical aberration is corrected by the hyperbolic secondary mirror while distortion is negligible. Some classical Cassegrain telescopes may indicate traces of field curvature.

In these calculations, a new parameter is introduced, referred to as the relative back focal distance η. This parameter is defined as the primary to final focus separation in units of the focal length. It is given by Equation (5.21), where B is the back focal length, f_1 is the focal length of the primary mirror, m is the magnification and k is the height of the marginal ray at the secondary given by $k = 1 - s/f_1$.

$$\eta = B/f_1 \tag{5.21}$$

There is generally no spherical aberration in classical Cassegrain telescopes. The conics needed to cancel spherical aberrations are determined from the radii of

curvature (Equation (5.8) and Equation (5.9)) and separations between the two mirrors. The relation by which this is possible is given by Equation (5.22). The parameters K_1 and K_2 are the primary and secondary mirror conic constants respectively. This expression was derived by setting the sum of spherical aberration coefficients given by Equation (5.11) equal to zero, for both the primary and secondary mirror.

$$K_2 = -\left(\frac{m+1}{m-1}\right)^2 + \frac{(K_1+1)m^3}{k(m-1)^3} = -\left(\frac{m+1}{m-1}\right)^2 + \frac{K_1+1}{k\left(1-1/m\right)^3} \tag{5.22}$$

All Cassegrain telescopes have a parabolic mirror, therefore their conic constants are given by Equation (5.11) In order to correct for the spherical aberration in a classical Cassegrain, the primary conic has be appropriately combined with a secondary mirror conic. This secondary mirror would be given by

$$K_2 = -\left(\frac{m+1}{m-1}\right)^2. \tag{5.23}$$

In this expression, m represents the lateral magnification. The secondary mirror is hyperbolic. The spherical aberration is corrected by introducing an aspherical contribution that cancels spherical aberration.

Coma is known as the most problematic aberration in all Classical Cassegrain telescopes. Coma can be calculated by adding the spherical and aspherical contributions to the coma aberration for both mirrors expressed by their aberration coefficients as seen in Equation (5.15) When each mirror is corrected for spherical aberration, the coma of the whole telescope becomes equal to the coma of the paraboloid with the same effective focal length (F) or F-number (Malacara and Malacara, 2004). The coma aberration can then be expressed as Equation (5.24),

$$Coma = \frac{\left(1+\frac{(K_1+1)(m-\eta)m^2}{2(1+\eta)}\right)}{4F^2}. \tag{5.24}$$

In the same way, the astigmatism for the whole Cassegrain is given calculated from the sum of the aberration coefficients of each mirror. Given that the spherical aberration is zero, the sagittal astigmatism can be given by

$$Astigmatism = \frac{\frac{m^2+\eta}{m(1+\eta)} - \frac{m(K_1+1)(m-\eta)^2}{4(1+\eta)^2}}{2F}. \tag{5.25}$$

The Petzval curvature and the astigmatism produce a convex focal surface which increases with the magnification of the secondary mirror (Malacara and Malacara, 2004). The

field size will therefore decrease to compensate for this curvature increase. This image curvature is given by:

$$R_{Petzval} = -\frac{(1+\eta)F}{m(m-\eta)-m-1} = \frac{R_1 R_2}{2(R_1 - R_2)} \tag{5.26}$$

The convex focal surface is (of best definition) given by:

$$R_{best} = -f\frac{1+\eta}{m^2+m-1-(K_1+1)m^3/2} \tag{5.27}$$

The amount of distortion in a classical Cassegrain is extremely small, smaller than seeing size so that it can be considered negligible in classical Cassegrain systems. The effects are not of great importance because they can be calibrated out (Malacara and Malacara, 2004).

5.6 Aberration effects on telescope optical performance

Once the numerical values of Seidel aberrations are determined, the analysis will not be complete without examining the effect these aberrations will have on the image quality of the telescope. There are many procedures used to predict the performance of optical systems. For this analysis, ray plots, a spot diagram and Point spread function (PSF) were chosen due to the fact that they estimate the quality as a direct result of geometrical aberrations present on the system. The analysis was done using optical design software OSLO (http://www.lambdares.com/), which allows the user to first design, then analyse the telescope to evaluate its overall quality.

5.6.1 OSLO

OSLO, which stands for Optics Software for Layout and Optimization, is a commercial optical system design software package that uses the technique of ray tracing to simulate the path and behaviour of light in a specified optical system from object to space. The optical system is represented as a collection of optical surfaces in space instead of a collection of optical elements. This allows the user to precisely define the type of surface and its properties. These properties include reflective/refraction indices, conical shapes, materials, surface curvatures etc. Any geometrical surface can be represented. The assigned properties help the software to recognize the true surface representation (mirrors, lenses, prisms) and how they affect the trajectory of light passing through them.

5.6.1.1 Aberration analysis

OSLO presents aberrations in both graphic and text format. There are two ways to graphically display aberrations in an optical system: either as transverse ray plots or as field plots. Ray plots, also known as ray intercept curves, are curves which plot either the transverse or longitudinal error of a particular ray relative to the chief ray as a function of the ray height in

the entrance pupil. For a perfect image with no ray error, the curve would be a straight line coincident with the abscissa of the plot. The aberration is usually plotted along the vertical axis. The type of plot usually depends on the aberration. The common aberrations usually displayed as ray plots are spherical aberration and coma. Spherical aberration is indicated by a cubic or S-curve ray intercept plot, while coma is indicated by a parabolic or U-curve. These are often combined as a single graph as illustrated in Figure 5-15.

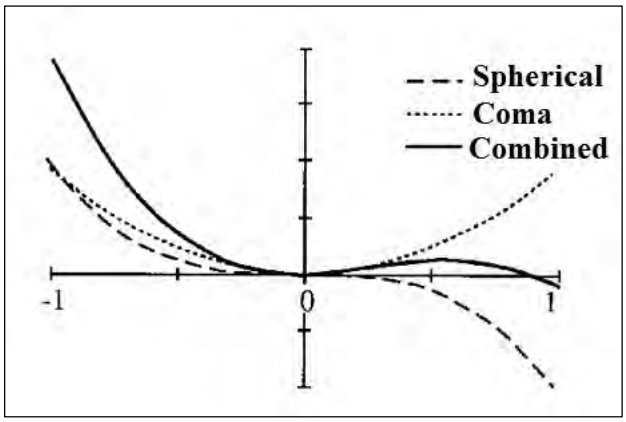

Figure 5-15: Ray plot showing coma combined with spherical aberration. The cubic ray intercept curve represents spherical aberration while the parabolic curve indicates coma (O'Shea and Harrigan, 1995).

It is, however, sometimes more appropriate to plot the longitudinal aberration as a function of field angle. These are referred to as field plots. Commonly used to plot astigmatism, field curvature and distortion, field plots present information about these aberrations across the entire field. The field angle is usually the independent variable and is plotted vertically, while the aberration is plotted horizontally. The plots for these aberrations are displayed in Figure 5-16.

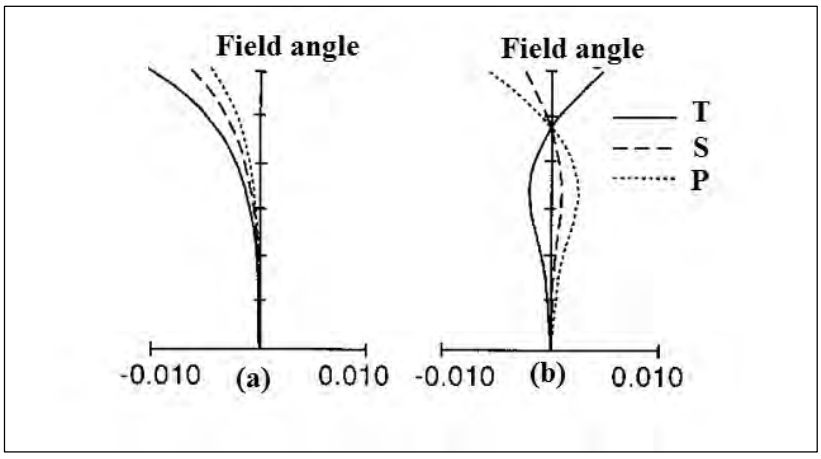

Figure 5-16: Field plots illustrating image field curvature aberration. The tangential T, sagittal S and Petzval surface P are plotted over the field. The system in (a) has not been corrected for field curvature while (b) has been corrected (O'Shea and Harrigan, 1995).

5.6.1.2 Spot diagram analysis

A spot diagram is a representation of a geometrical image blur produced by an optical system with aberrations (Greivenkamp, 2004, Fischer, Tadic-Galeb and Yoder, 2008). It is obtained by dividing the entrance pupil of the optical system into a large number of equal areas (either rectangular or polar) and tracing a ray from the object point through the centre of each of the small areas (Smith, 2000). The intersection of these rays with the focal plane is given by the spot diagram, which gives a visual representation of the energy distribution in the image of the point object. The shape of the spot diagram is indicative of the dominant aberrations in the system. Figure 5-18 portrays spot diagrams of a system infected by different aberrations.

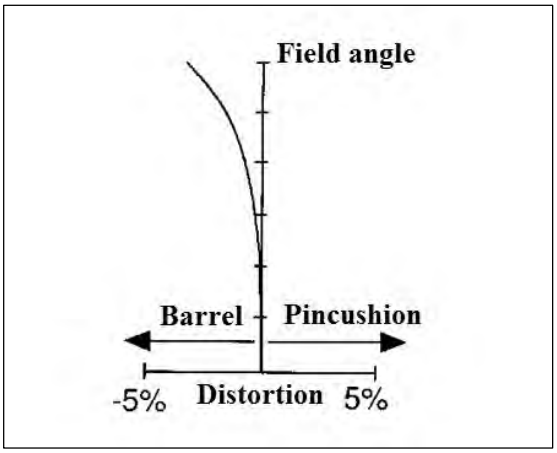

Figure 5-17: Field plot illustrating distortion in an optical system. The distortion aberration is calculated a percentage (O'Shea and Harrigan, 1995).

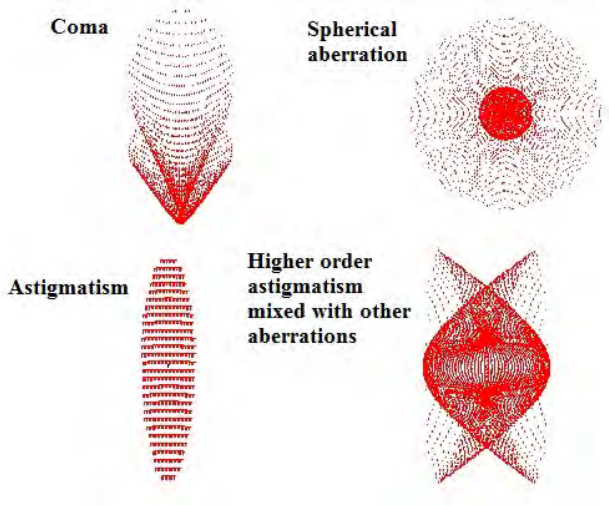

Figure 5-18: Spot diagrams indicating the presence of aberrations. Coma aberration appears like a comet shape, while spherical aberration is a circular shape. The shape of astigmatism depends on which plane it was measured. If measured from the sagittal plane, it appears stretched in the vertical direction (optics.synopsys.com).

The general output of the spot diagram is the RMS spot radius or diameter. This is the diameter of the circle containing approximately 68% of the energy (Fischer, Tadic-Galeb and Yoder, 2008). For N number of rays of a spot diagram, with transverse aberration given by (ε_x, ε_y), its centroid relative to the reference image location is determined by averaging the ray errors as such (Greivenkamp, 2004):

$$\overline{\varepsilon_y} = \frac{1}{N}\sum_{i=1}^{N}\varepsilon_{yi}, \tag{5.28}$$

$$\overline{\varepsilon_y} = \frac{1}{N}\sum_{i=1}^{N}\varepsilon_{xi}. \tag{5.29}$$

The minimum to maximum spot size is found by sorting through the transverse ray errors to find the total range in *x* and *y*. In order to obtain the RMS spot sizes in the x and y, the ray errors are integrated (infinite number of rays) or summed over the pupil as shown in Equation (5.30) and Equation_(5.31).

$$RMS_x = \left[\frac{1}{\pi}\int_0^{2\pi}\int_0^{1}\left(\varepsilon_x - \overline{\varepsilon_x}\right)^2 \rho d\rho d\theta\right]^{1/2} = \left[\frac{1}{N}\sum_{i=1}^{N}\left(\varepsilon_x - \overline{\varepsilon_{xi}}\right)^2\right]^{1/2} \tag{5.30}$$

$$RMS_y = \left[\frac{1}{\pi}\int_0^{2\pi}\int_0^{1}\left(\varepsilon_y - \overline{\varepsilon_y}\right)^2 \rho d\rho d\theta\right]^{1/2} = \left[\frac{1}{N}\sum_{i=1}^{N}\left(\varepsilon_y - \overline{\varepsilon_{yi}}\right)^2\right]^{1/2} \tag{5.31}$$

5.6.1.3 Point Spread Function (PSF)

For perfect optics filtered only by a finite circular aperture, the incoming radiation from a point source is described by the Airy function. However, no telescope produces perfectly circular images. The Airy function is broadened by aberrations and atmospheric turbulence. This broadening is described by the Point Spread Function (PSF). The PSF provides the overall shape of the distribution of light which originates from a point source. The degree of spreading of the point object is a measure for the quality of an imaging system.

The size of the Airy disk and the amount of spacing between the diffraction rings will depend on the wavelength of the point source, the aperture of the telescope and the size of the object. Shorter wavelengths of light will result in a small image of a sub-resolution point source with closer spacing of the diffraction rings while longer wavelengths will result in larger Airy disk with greater spacing between diffraction rings. The degree of spreading of the point source is a measure of the quality of the optical system. Ideally, the PSF should be as small as possible.

OSLO calculates the PSF, also referred to as the irradiance distribution, from the geometric wavefront available from the spot diagram rays. If an incoherent light source of wavelength λ is used on an optical system of aperture area *A*, the PSF is given as (Born and Wolf, 1999):

$$I(x,y)=\left|\frac{i}{\lambda}\iint_{A}P(x,y)\frac{\exp\left(-ikR'\right)}{R'}dA\right|^{2}. \tag{5.32}$$

In this expression, *P(x, y)* is the pupil function given by:

$$P(x,y)=A(x,y)\exp\left[ikW(x,y)\right]. \tag{5.33}$$

Here, $k=2\pi/\lambda$, λ is the wavelength, *W(x, y)* is the wavefront shape in the presence of aberrations and *A (x, y)* is the amplitude distribution in the exit pupil. Equation (5.33) is valid for points inside the pupil. For points outside the pupil, the function is zero.

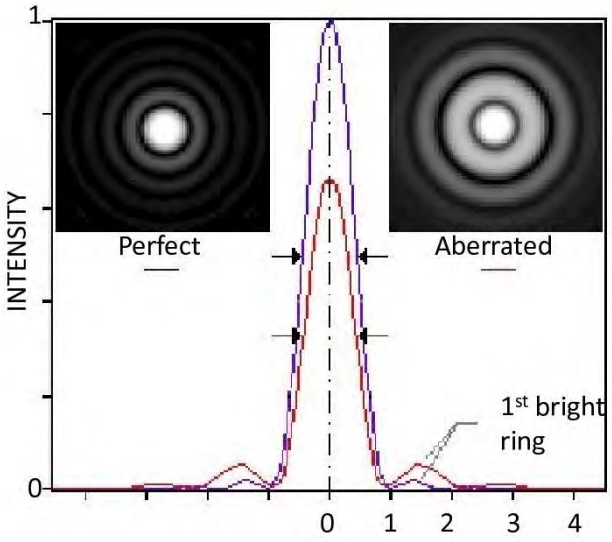

Figure 5-19: Diffraction patterns and PSF's for both perfect and aberrated optics (Source: http://www.telescope-optics.net/).

Since our telescope is a Cassegrain, the Fraunhofer diffraction theory for an annular aperture is used to describe the intensity distribution of a point source at infinity such as stars. In this case, the irradiance distribution, according to Malacara and Malacara (2004), is given by the Airy function

$$I(\theta)=\frac{4I_{0}}{\left(1-\varepsilon^{2}\right)^{2}}\left[\frac{J_{1}ka\sin\theta-\varepsilon J_{1}\left(\varepsilon ka\sin\theta\right)}{ka\sin\theta}\right]^{2}, \tag{5.34}$$

where $I(\theta)$ = intensity distribution at an angular semi-diameter θ, I_0= central intensity of the Airy pattern. Here J_1= first order Bessel function, $(k=2\pi/\lambda)$ is the wave number, a the semi-diameter of the circular aperture, and ε is the ratio of the radius of the central obstruction to the aperture. For a circular aperture, ε = 0, the irradiance distribution can be simplified to:

$$I(\theta)=I_{0}\left[\frac{2J_{1}\left(ka\sin\theta\right)}{ka\sin\theta}\right]^{2}=I_{0}\left[\frac{2J_{1}(b)}{b}\right]^{2}. \tag{5.35}$$

Here $b = ka\sin\theta$. This value can also be expressed in terms of the airy radius and the numerical aperture ($NA = n\sin\theta$). The value of b then becomes:

$$b = kNAr. \tag{5.36}$$

For telescopes with larger apertures, the Airy disk diameter decreases linearly and increases with longer wavelengths. The radius of the Airy disk with aperture diameter D and focal length F is given by

$$r = 1.22\frac{\lambda F}{D} \tag{5.37}$$

The factor of 1.22 is derived from calculating the position of the first dark ring surrounding the Airy disk (Napier-Munn, 2008). The diffraction limit can then be expressed as:

$$r = \frac{0.61\lambda}{NA} \tag{5.38}$$

5.6.1.4 Strehl Ratio

From the PSF, the Strehl ratio of the optical system can be determined. In 1896, Karl Strehl proposed a criterion for quality assessment of optical systems by deriving a ratio of the maximum intensity of the PSF of an optical imaging system (Ridpath, 1997). Its theoretical value in the absence of aberrations is given by the Airy function. The Strehl ratio presents the simplest method of wavefront aberrations on image quality. It is simply the ratio of peak diffraction intensities of an aberrated and perfect wavefront presented in terms of the RMS wavefront error as displayed in Figure 5-20 (Mahajan, 1983):

$$S \sim \frac{1}{\exp(2\pi\omega)^2}. \tag{5.39}$$

Here ω is the RMS wavefront error in units of the wavelength. A ratio of 1 indicates perfect optics and anything less than 1 indicates less than perfect optics.

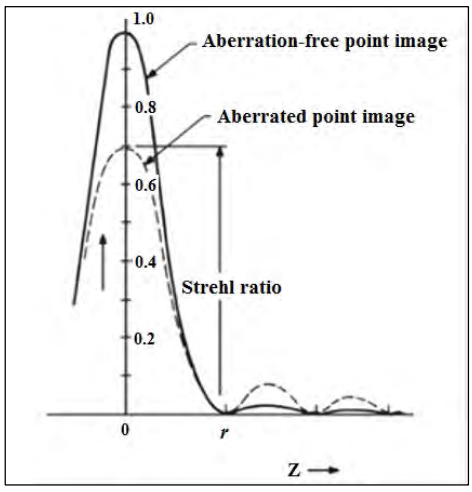

Figure 5-20: The Strehl ratio measured from the Point Spread Function (source: http://ned.ipac.caltech.edu/level5/Glossary/Figures/strehl.jpg).

5.7 Modelling and structural analysis of primary mirror

Diffraction-limited performance of a large telescope requires accurate simulation of both the optical and structural systems it is composed of (Angeli et al. 2004). The previous section was based on optical analysis through image quality evaluation. However, the surface figure of the primary mirror has a great impact on the optical performance. Most large ground-based telescopes suffer from deformations due to their own weight under gravity (Bely, 2003). These deformations tend to significantly degrade the performance of the primary mirror. Structural analysis can be used as a tool to assess the optical performance to ensure that the mirror can still achieve its optical and structural goals. This section will focus on opto-mechanical analysis of the primary mirror and its support system.

The purpose of the mirror support is to support the mirror weight and maintain nominal surface figure over operational zenith angles and environmental conditions. The mirror is supported both axially and radially to prevent the mirror deformation due to forces of gravity, wind and telescope acceleration. Validation of the primary mirror support system can be done by a deformation analysis of the mirror under its own weight. In order to analyze any deflections on the mirror due to gravity, a deformation model was created through a technique of Finite Element Analysis (FEA) with the ANSYS engineering software. This technique is described in detail in section 3.6.

ANSYS is one of the many FEA software packages available on the market. ANSYS is a structural engineering software package designed to perform structural analysis including linear, non-linear and dynamic analyses. It is regarded as a "powerful engineering tool" applied in aerospace, automotive, and nuclear industries (Moaveni, 1999 and Keel, 2009).

ANSYS was chosen over other FEA software packages due to the following reasons:

1. The complex geometry of the honeycomb structure of the mirror can easily be modelled in ANSYS by using layered definitions or adhesive bonding of the cores, depending on how the mirror was fabricated.
2. The degrees of freedom of the kinematic whiffle-tree support can be modelled with spherical joints.
3. It allows modelling of bonded structures with different stiffness behavior, i.e. the deformable mirror with a rigid support.
4. ANSYS incorporates many methods for meshing depending on the geometry. These methods can take into account the curvature of the cellular core of the mirror.
5. In addition, the modeling can be done by simply following a wizard guide detailing all the steps required for a specific analysis type.

5.7.1 Experimental method

The validation of the primary mirror support system can be done by a deformation analysis of the mirror under its own weight. In order to analyze any deflections on the mirror due to gravity, a deformation model was created using the finite analysis technique in ANSYS structural engineering software. The software does the analysis in three stages, namely; pre-processing, solution and post-processing as illustrated in the conceptual model in Figure 5-21.

5.7.2 Pre-processing stage

The first step when doing a finite element analysis is to determine the relevant type of analysis for the problem at hand. For this simulation, a linear static structural analysis was chosen. This is due to the fact that the deformations experienced by the optical mirror under its own weight are relatively small when compared to its size. Generally, a linear structural analysis is used under the following conditions:

- To determine the deformations and stresses of structures that do not induce significant inertia and mass damping effects.
- The loads and structures are assumed to vary very slowly with respect to time; no varying forces are considered.
- The material experiences elastic behaviour, meaning that the material will return to its original shape under deformation.

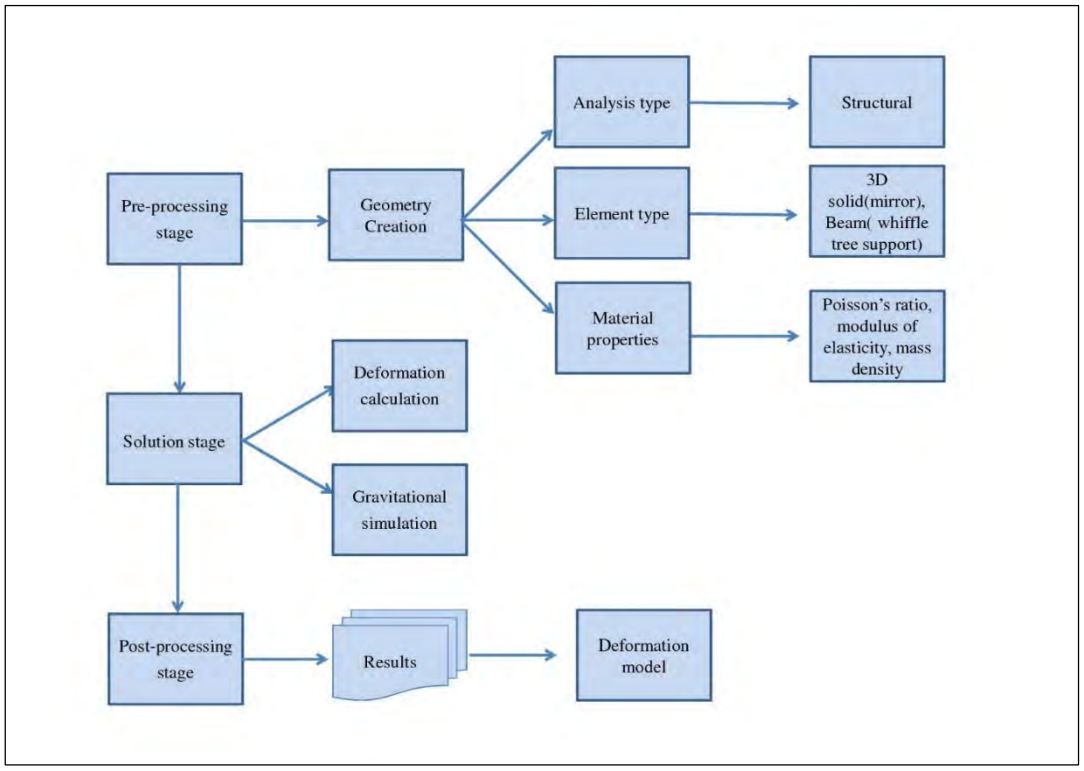

Figure 5-21: Conceptual model illustrating the process of determining the deflection of the primary mirror in ANSYS.

Geometry

In the pre-processing stage, a 3D element was chosen to represent the mirror surface and beam elements to represent the support structure. In this research, a CAD geometry drawn in SolidWorks was exported into ANSYS Workbench. The software assigns elements to the exported geometry. The accuracy of the results highly hinges on the choice of elements. The stiffness behavior of the mirror is specified as flexible while the whiffle-tree specified as rigid.

Material properties

The second step at this stage was to insert the properties of the geometry. The mirror is made of Zerodur glass ceramic, which is a lithium aluminosilicate glass-ceramic produced by Schott AG (www.schott.com). Since the form of analysis is linear, isotropic properties of the material were required.These properties are:

Young's Modulus $E = 90,3$ GPa

Poisson's ratio $v = 0,243$

Mass density $\rho = 2530$ kg/m^3

Shear Modulus $G = \frac{E}{[2(1+v)]} = 36,3$ GPa

Connections

The whiffle-tree support is connected to the mirror surface to prevent rigid body motion. The triangular plates are connected to the 18 supports pads by spherical joints. The support locations are important as they highly determine the amount of deflection the mirror will experience.

Boundary conditions

The deflection of axial supports is usually greater than the deflection of the radial supports, hence only axial surface deflections are considered for this research. A gravity load vector was applied in the direction normal to the optical axis of the mirror. In order to prevent rigid body motion, the 18 support pads were constrained to the mirror surface and the 6 pivot joints constrained to the mirror cell. The mirror is also constrained on three radial supports located 120° from each other around the cylindrical edge of the mirror. These supports are important in order to limit shear deformations.

5.7.3 Solution stage

To determine the solution, a mesh of the geometry was generated. This assists the programme to solve the model in small discrete parts to determine a more accurate solution. Resultant total

and directional deformations experienced by the mirror under the specified boundary conditions were computed. The deformations of honeycomb structures are composed of bending and shear components. As the thickness/diameter ratio of the mirror increases, shear deformations become significant. That is: Total deformation = Bending deformation + shear deformations. For a diameter/thickness ratio of 10, the shear deformation is approximately 10% of the bending deformation.

5.7.4 Post-processing stage

The post processing stage allowed display and analysis of the resultant displacement distributions derived from the computed solution. The solutions revealed how the applied loads affected the surface of the mirror surface. High quality telescopes usually require that the surface deformation be limited to a small fraction of the wavelength of light that the telescope is designed to use. The general rule of thumb for judging the adequacy of the support system is if the mirror deforms less than quarter the wavelength of light. The results can be presented in graphical format or exported into Excel for further post-processing if necessary.

5.8 Structural efficiency of primary mirror

Honeycomb mirrors are extremely structural efficient compared to other lightweight mirror designs. The LLR primary mirror weighs 84 kg, hence the expected maximum mechanical deformations from sandwich mirrors should be within the 400 nm range as illustrated in Figure 5-22.

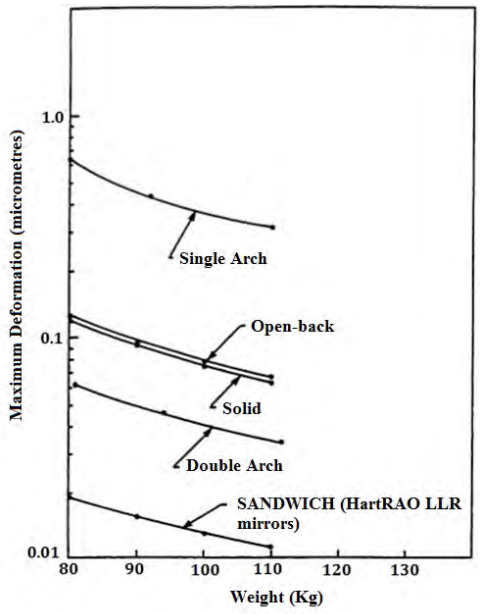

Figure 5-22: Expected mechanical deformation of different types of mirror designs (Vukobratovich, 1999).

5.9 Chapter Summary

The methods and experimental procedures for achieving the objective listed in the first chapter were discussed in this chapter. It began by explaining the processes followed when cleaning the LLR telescope primary mirror. The design of the optical path to transport the last, was firstly discussed. This included a list of the chosen components as well as their specifications. The relay mirrors chosen for the path were tested using a spectrometer to determine their reflectivity. These measurements, together with transmission measurements from the lenses in the beam expander were used to estimate the throughput of the system along two possible optical paths. The procedure followed when conducting image quality analysis of the system was discussed in the fourth section of the chapter. Ray tracing software called OSLO was used for this purpose to analyse all aberrations expected in the system. The theory on how this is carried out by the software was also explained. Lastly, the procedure for conducting a structural analysis of the system through monitoring of gravitational deformation on the primary mirror during ranging was discussed. ANSYS Finite Element Analysis software was chosen for this task and the experimental method to be followed for carrying out the simulation was discussed.

6

RESULTS AND DISCUSSIONS

6.1 Introduction

The HartRAO telescope optical performance was validated through the analysis of three key aspects: Image quality (aberrations), transmission and structural efficiency. Optical design and analysis software packages were used to determine the basic system parameters as well as provide a detailed analysis of the image quality through the assessment of aberrations. Spot diagram and Point Spread Function results are presented to quantify the results obtained from ray intercept curves. The total efficiency of any optical system is dependent on the primary mirror's aperture, surface quality and system throughput. The second section of this chapter presents the results of the spectroscopic measurements taken to determine the total throughput of the telescope. The reflectivity and transmission measurements are presented and used in the calculation of the overall throughput of the optical system. The throughput is calculated for the two proposed optical paths. Finally, the structural analysis results of the primary mirror will be presented and discussed.

6.2 Telescope optical design and characteristics

The telescope is a Cassegrain design. It has a parabolic primary and a convex secondary mirror. Using measurements and Cassegrain equations, the optical characteristics of the telescope were calculated. Basic system parameters such as the entrance pupil diameter D_1, system focal length F, primary focal length f_1 and primary to focal plane e distance were easily measured manually. These are the main parameters of the Cassegrain system. All other parameters were derived from these using Cassegrain equations. Manual calculations were validated through the use of ATMOS, an optical design and analysis software. The software then computes all the other parameters as shown in Figure 6-1.

The focal ratio categorizes this system as moderate. It is neither fast nor slow in photographic speed. This means that it is suitable for observing just about every object in the sky, from high power objects such as the Moon and planets to low power objects such as star clusters and galaxies. Moderate optical systems tend to be easier to collimate than faster ones and are also less prone to aberrations.

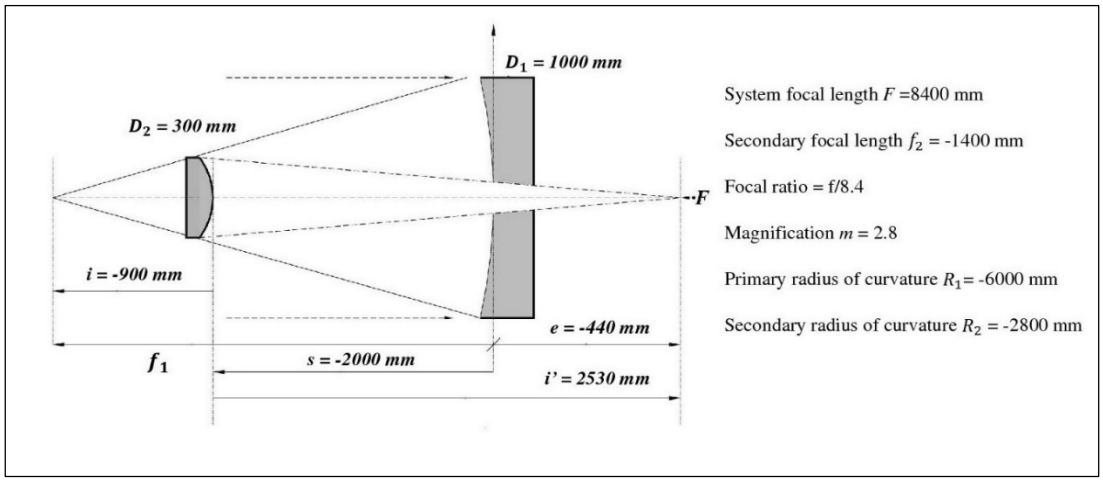

Figure 6-1: Optical parameters of the HartRAO LLR telescope on a right handed Cartesian coordinate system. The sign of the parameters are positive in the direction of incoming light (left to right) and negative for the opposite direction.

6.3 Aberration analysis

The HartRAO LLR telescope is a Cassegrain variant with a parabolic primary and hyperbolic secondary mirror. The conical combination of the system is supposed to correct for any spherical aberration in the system. Such a system is expected to have traces of coma, astigmatism and field curvature. Image distortion is often very small to be of significance in the image quality. No aberrations are expected on the optical system for on-axis measurements. The sizes of aberrations increase with field angle.

6.3.1 Telescope field angle

In this analysis, the aberrations will be assessed in terms of the usable field of view of the optical system. Since the field size is a direct measure of the amount of information delivered by the system, it holds as a key parameter for rating its performance. The field of view for the HartRAO telescope was estimated from a CCD camera which can possibly be used with the telescope. The choice of camera is dependent on the type of specifications required for Lunar Laser Ranging application. Nickola (2012) provided a list of CCD cameras which closely meet the consideration of ideal match between CCD pixel size and telescope focal length. One of these is the Point Grey GRAS-20S4M CCD camera with a pixel size of 4.4 μm and 1624 × 1124 pixels in array. More information on the additional specifications considered in choosing in CCD camera can be found in Nickola's work (Nickola, 2012).

Using the New Astronomy CCD calculator, the image scale and field of view of both telescope and camera combination were computed. The image scale describes the amount of sky coverage which can be seen by a single pixel of the CCD camera. It is dependent on the

pixel size of the camera and the focal length of the telescope, given by Equation (6.1) (Wodaski, 2002).

$$\text{Image scale} = \frac{205\times \text{ CCD pixel size } (\mu\text{m})}{\text{Telescope focal length (mm)}} \tag{6.1}$$

The image scale is measured in arc-seconds per pixel. A longer focal length with smaller pixel sizes mean less sky coverage but at a higher resolution. This image scale is then multiplied by the number of pixels in the array to determine the horizontal and vertical field of view in arc-minutes. Figure 6-2 is a screenshot of the field of view calculated by the CCD calculator. This is the field angle which was used to analyse the image quality of the system in OSLO. At 1/22nd of a degree, this can be regarded as an acceptable field of view on condition that collimation is kept as accurately as possible.

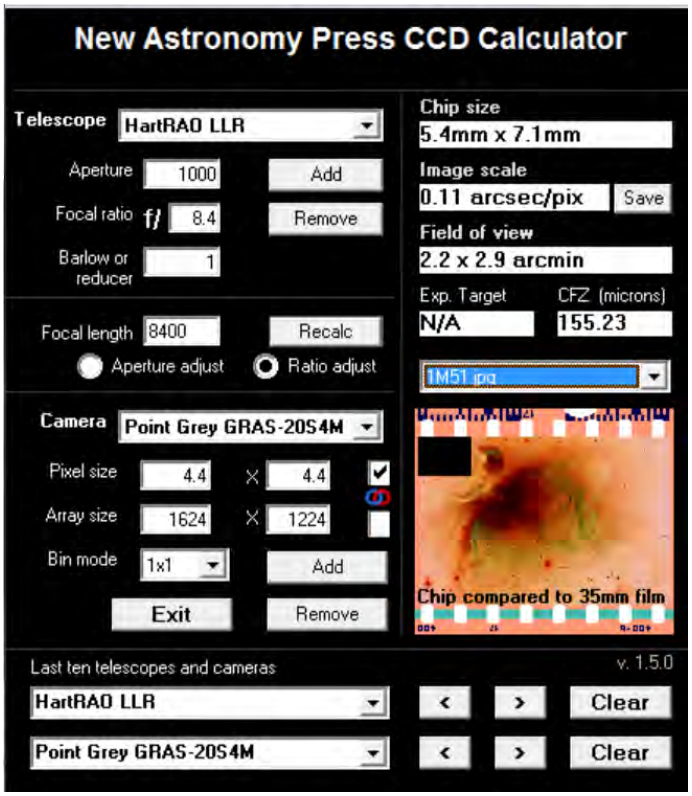

Figure 6-2: Screenshot of CCD calculator used to compute image scale and field of view of the HartRAO telescope with compatible CCD camera.

6.3.2 OSLO model

All the calculated parameters of the telescope were inserted into OSLO in the form of surfaces. The optical system is made up of 5 surfaces. Listed in the sequence followed by impinging light, these are: entrance pupil, secondary spider, primary mirror, secondary mirror and image focal plane. The individual parameters of each surface should be specified, such as the radius of curvature, aperture radius, thickness or distance to the next surface, conic

constants, medium with its index of reflection/refraction and in the case of the spider, the width and number of vanes. The linear sign of each parameter has to be taken into consideration. They are positive in the direction of incoming light (left to right) and negative in the opposite direction. Curvatures with the convex side to the left are signed positive; otherwise, they are negative. Before analysis can be done, key parameters such as field angle and wavelength should be stated. The analysis was done for a wavelength of 532 nm and field angle of 1/22nd of a degree. The optical design model is shown in Figure 6-3.

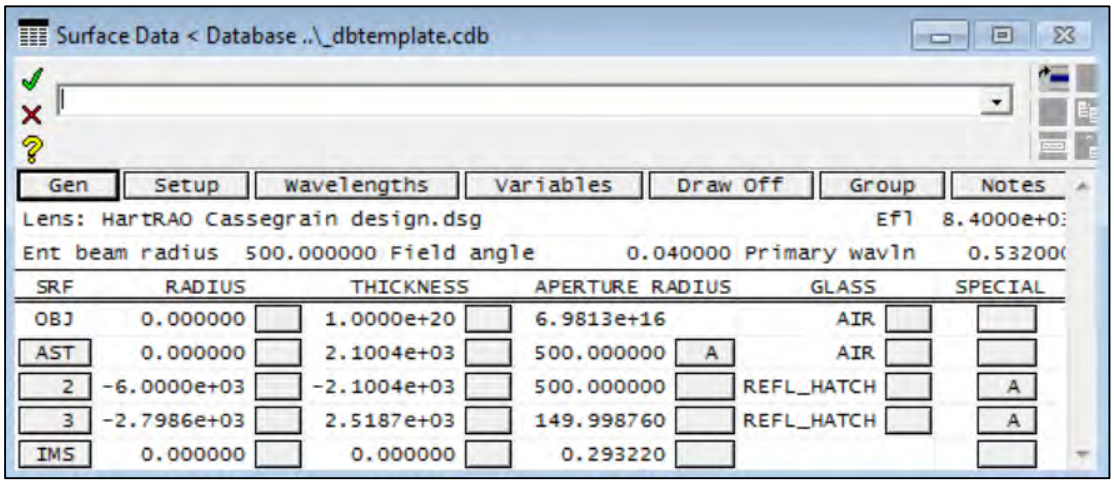

Figure 6-3: OSLO optical design model for the 1000 mm, f/8.4 HartRAO lunar laser ranger. It is composed of 5 surfaces including the object and image surfaces.

6.3.3 Ray intercept curves

A first glance of the ray intercept curves (left of Figure 6-4) reveals that coma is the dominant aberration in the optical system. This is indicated by the parabolic shape of the curve and no visible indication of spherical aberration. To ensure the cancellation of spherical aberration, Equation (5.23) was used to calculate the conic constant of the secondary mirror. All the plots displayed are not to scale and are merely used to illustrate the type of aberrations present in the system. The amount of aberration can be read on the vertical axis of the curve.

Using Equation (5.24), the amount of coma in the telescope was calculated to a value of 0.003367 mm. Telescope makers recommend a threshold 0.003 mm, before coma can be regarded as widely degrading of image quality. This value can further be reduced by proper alignment of the telescope optics. The long focal length of the system proves to be an advantage in this case, since it provides a higher resolution in the system even in the presence of excessive coma. Coma is positive for all Cassegrain telescopes; this is indicated by the upward shift in the curve. There is no coma for on-axis measurements. Coma is seen to have a linear dependence with image height as proved by the wavefront expansion in Equation (4.1). In addition to image

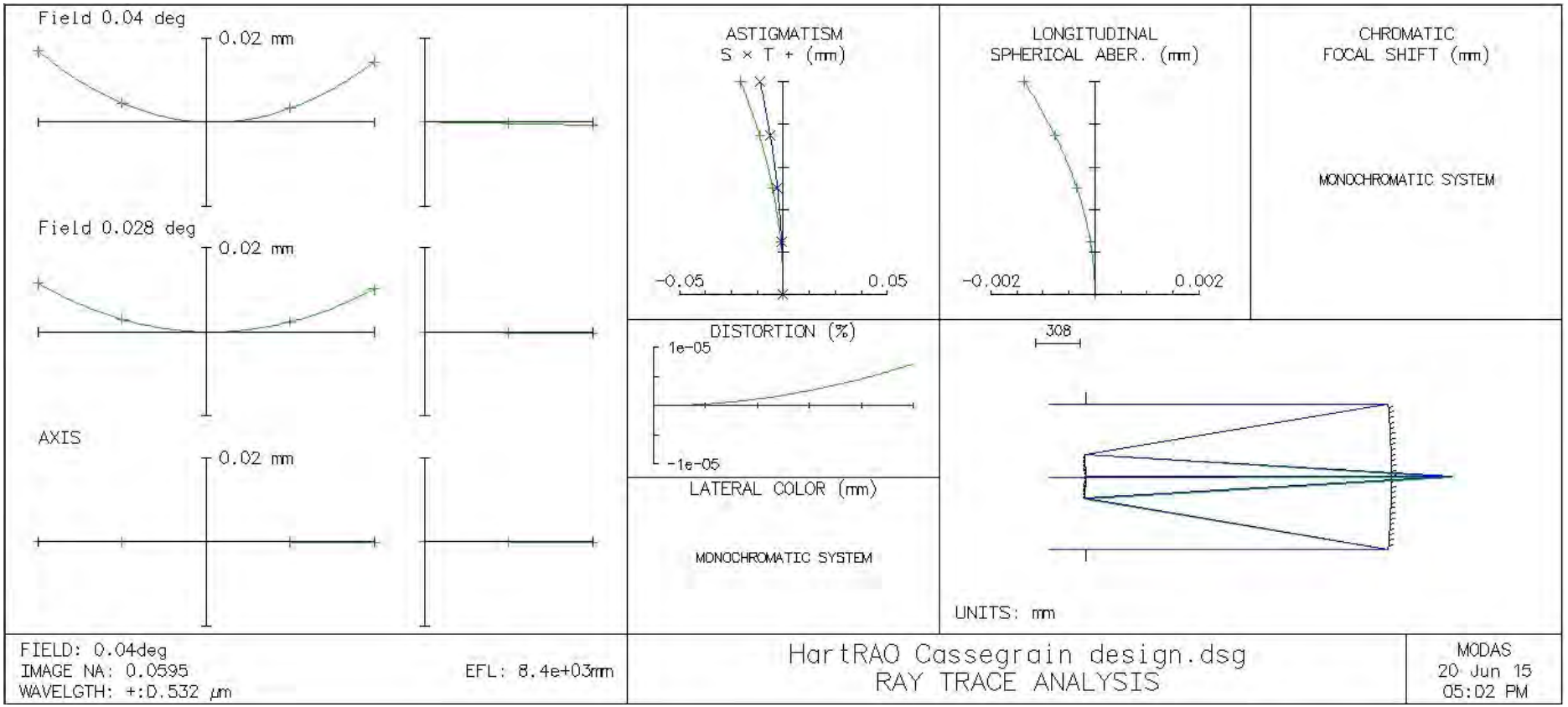

Figure 6-4: Ray trace analysis for the HartRAO telescope generated by OSLO. The section on the left of the diagram represents tangential (left) and sagittal (right) aberration curves. Also illustrated are astigmatism, longitudinal spherical aberration and distortion curves. The system has no chromatic and lateral colour aberrations since it is a reflector. The lower right box indicates how rays are traced through the optical system.

height, the excessive coma is also due to the large aperture of the telescope since coma is known to increase with aperture.

The ray intercept curves represent both tangential (left) and sagittal (right) aberrations. Only one side of the sagittal curve is usually plotted because skew ray fans are symmetrical across the tangential plane. A comparison between the tangential and sagittal fans reveals the amount of astigmatism in the image for that field point. The different slopes at the origin of the curves indicate the presence of astigmatism. While evidence of astigmatism is seen, the actual amount can be determined by a field plot. Astigmatism becomes less significant at small field angles such as those used in LLR observations. The second most dominant of all aberrations is field curvature with a value of -0.000390 mm for a field range of field angles. Field curvature is however not of great concern for Lunar/Planetary observations. It is problematic on telescopes designed mainly for photographic purposes. At a percentage of 1.24×10^{-7}, this amount of distortion is evidently too small to cause significant effect on the image quality on an F/8.4 telescope with a CCD camera with 4 .4 µm pixel size.

6.3.4 Spot diagram analysis

The generated spot diagrams correspond to the three aberration curves for the on-axis, 0.7 and full field positions in the aperture of the systems. The aberration curves were generated on a flat field. Due to apprehension of the presence of field curvature in the system, it is recommended that the shape of the spot diagram be shifted to compensate for it. The radius of curvature of the best focal surface, given by Equation (5.27) was calculated to be approximately 942 mm. This radius serves to balance the sagittal and tangential astigmatism in the system. This value is added in the image surface field as highlighted in Figure 6-5.

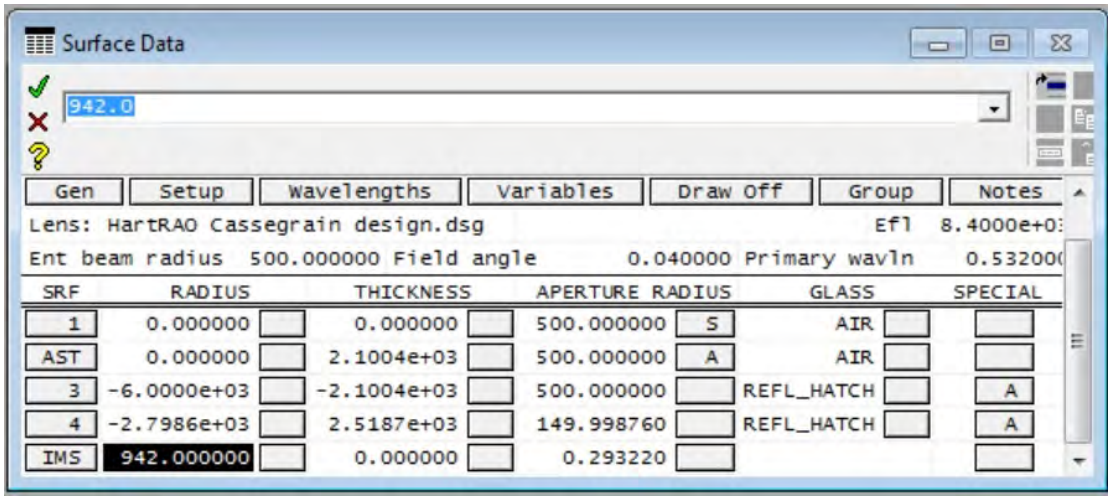

Figure 6-5: Surface data illustrating how to generate spot diagram on best focal surface. The best focal surface has a radius of curvature of 942 mm.

Figure 6-7 represents spot diagrams corresponding to the aberration curves in Figure 6-4. Also illustrated is the sensitivity of the image quality with focus shift. The comet shape substituents the earlier claim of coma as being the dominant aberration in the system.

The system is seen to be diffraction-limited for on-axis performance since all the energy is contained within the Airy disk. As the off-axis field angle increases, so does the image blur spot radius. The intensity of the spots are also seen to weaken when the focus is shifted more than 0.1 mm inside or outside of focus. After this, the image seems to appear highly degraded. The properties of the blur spot radius are shown in Figure 6-6. The scale of the diagram is selected by the programme to fill the space allowed. It should be noted that the spot size was calculated due to the effects of geometric effects only. It does not take the effects of diffraction into effect. However, diffraction effects are always present, even in the most perfectly collimated of optical systems; therefore they should be taken into consideration. Ignoring these effects could greatly discredit all conclusions drawn from aberration and spot diagram analyses. Based on diffraction theory, the Rayleigh criterion gives the resolution limit of the telescope as determined by the radius of the Airy function first null, and is given by Equation (5.37) as 0.005456 mm. From this, it can observed that the geometrical spot size is incomparably smaller than the diffraction limit of the telescope.

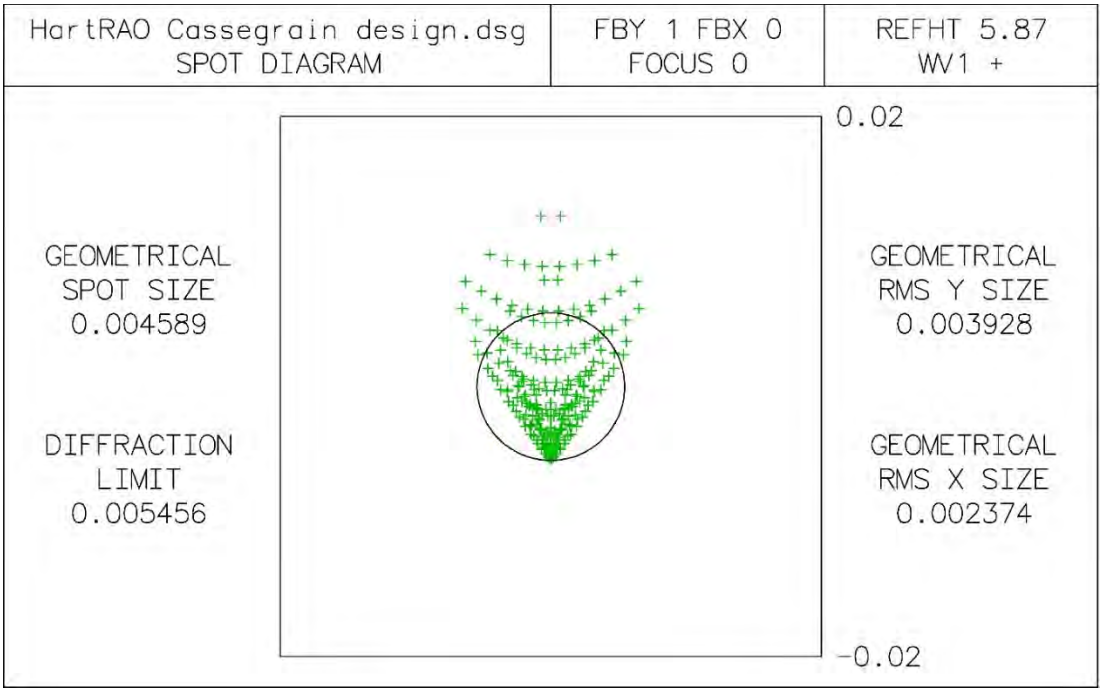

Figure 6-6: Single spot diagram of the HartRAO LLR telescope generated in OSLO. The geometrical spot size is significantly smaller in comparison to the theoretical resolution limit of the telescope.

Figure 6-7: Spot diagrams of the HartRAO LLR telescope generated in OSLO. The diagrams correspond to the aberration curves at different field angles, under varying focus shifts. The system is diffraction limited for on-axis performance, while image quality degrades with an increase in field angle.

6.3.5 Point Spread Function

As already established from the spot diagram, on axis performance of the HartRAO LLR telescope is diffraction-limited as seen in Figure 6-8. The PSF at this field is expected to produce the highest number of photons. Figure 6-9 depicts the variation of the PSF with field angle. The broadening is due to aberrations only. The atmospheric effects on the PSF have been studied separately by Nickola (2012). It can be seen from the fractional energy graphs (far right of Figure 6-9), that about 75% of all the energy is contained within the geometric spot radius.

The spreading out is mostly caused by the coma in the system, resulting in the observed asymmetry of the PSF graphs. The on-axis image size can cover up to 9 pixels for every 4.4 µm square pixel size of the CCD camera yielding a Strehl ratio of 0.99 as seen in Figure 6-8. This ensures high resolution imaging by the optical system. Off-axis performance yields a much lower Strehl ratio of 0.78 (Figure 6-10), which is considered a good measure of quality in visual systems. The light distribution is expected to change when atmospheric effects are considered, resulting in further spreading of the image. This will most likely cause smearing out of the star image without a pronounced peak, leading to errors in determining the star's position.

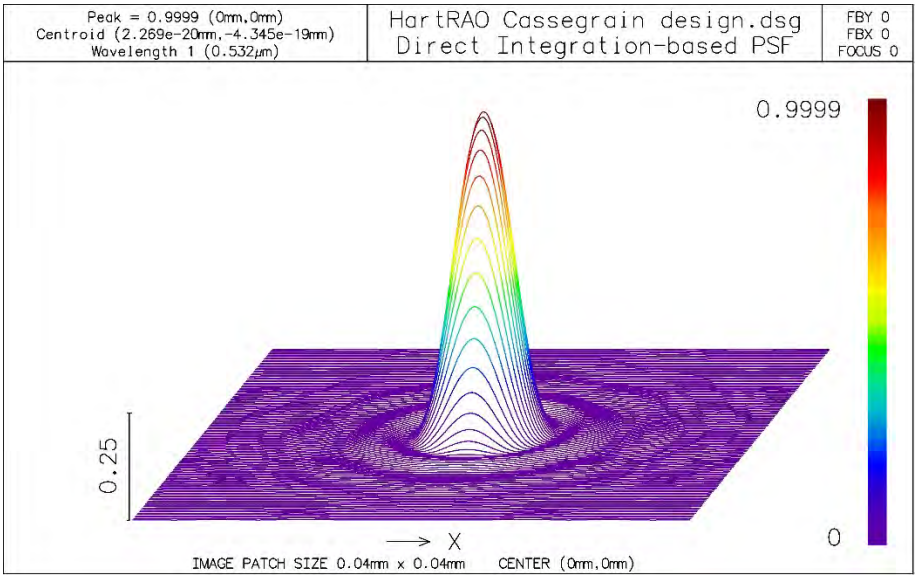

Figure 6-8: Point Spread Function for HartRAO LLR telescope for on-axis imaging. The Strehl ratio is 0.99.

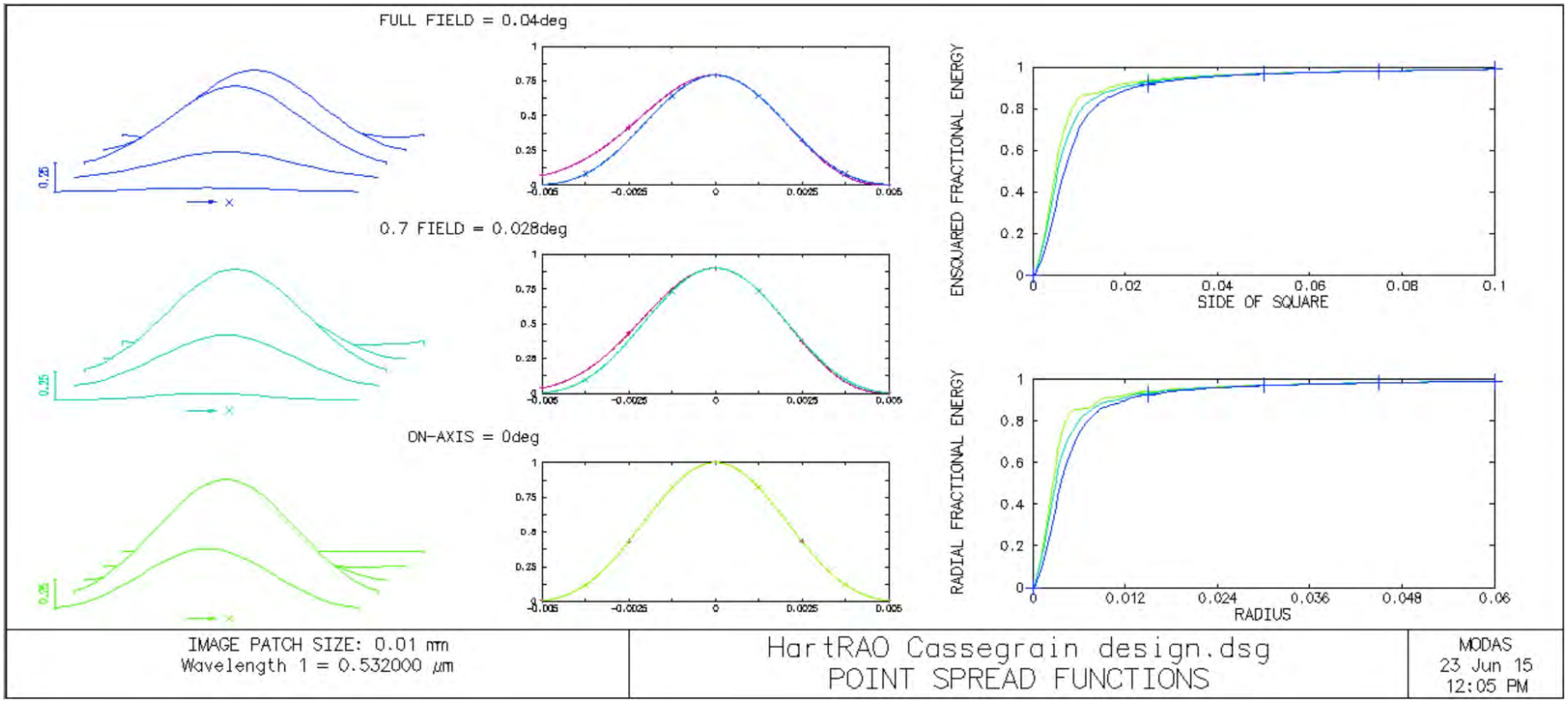

Figure 6-9: Point Spread Functions of the HartRAO LLR telescope generated in OSLO. The telescope is diffraction-limited for on axis performance, while about 70 -75 % of the energy is seen to be contained inside the geometric spot radius as the image field position moves further way from the optical axis.

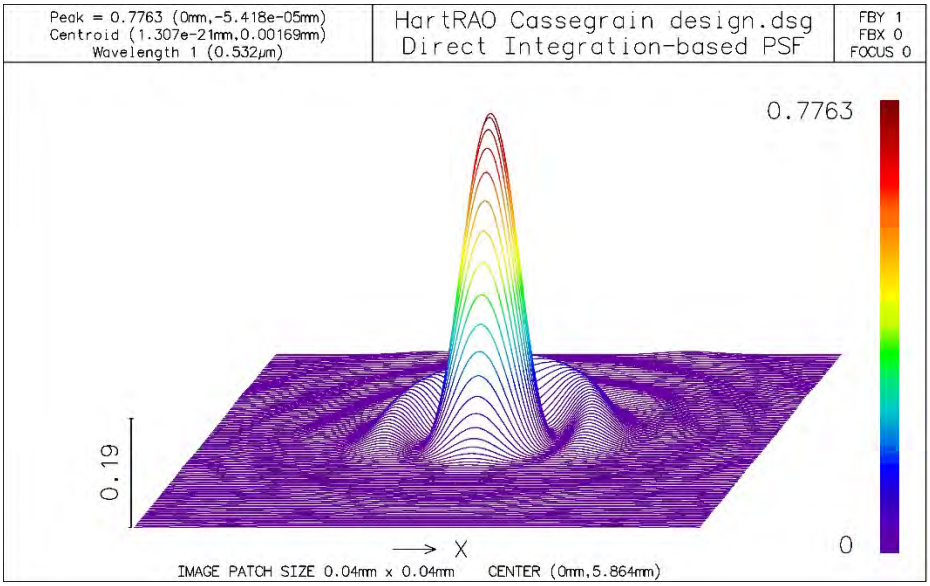

Figure 6-10: Point Spread Function for HartRAO LLR telescope for off-axis imaging. The Strehl ratio is 0.7763.

6.3.6 Effect of central obstruction on image quality

The Point Spread Function generated thus far takes into account the central obstruction in the light of the telescope (secondary mirror and spider vanes). The linear obstruction makes up about 30% of the diameter of the primary mirror, resulting in about 9% loss of light. If all obstruction conditions in the optical surface are removed, the ring intensities in the PSF are seen to decrease slightly. This is due to the fact that energy from the central peak is shifted to the other rings. This effect is much more visible with large obstructions. Figure 6-11 is a PSF generated under no obstructions.

Presence of the central obstruction results in a Strehl ratio increase by a factor of 0.0067. This affects the contrast in the image which will be slightly problematic for photographic observations. The loss of light will affect the overall throughput of the system by a factor dependent on the size of the annular aperture of the primary mirror. Removing the central obstruction will not necessarily result in a higher image quality since other aberrations will be introduced into the system. The loss of contrast introduced by the obstruction is a small trade-off compared to large spherical aberrations. The vanes of the spider have a width of approximately 2 mm and will therefore not result in significant changes in the image quality, introducing less than 1% obstruction.

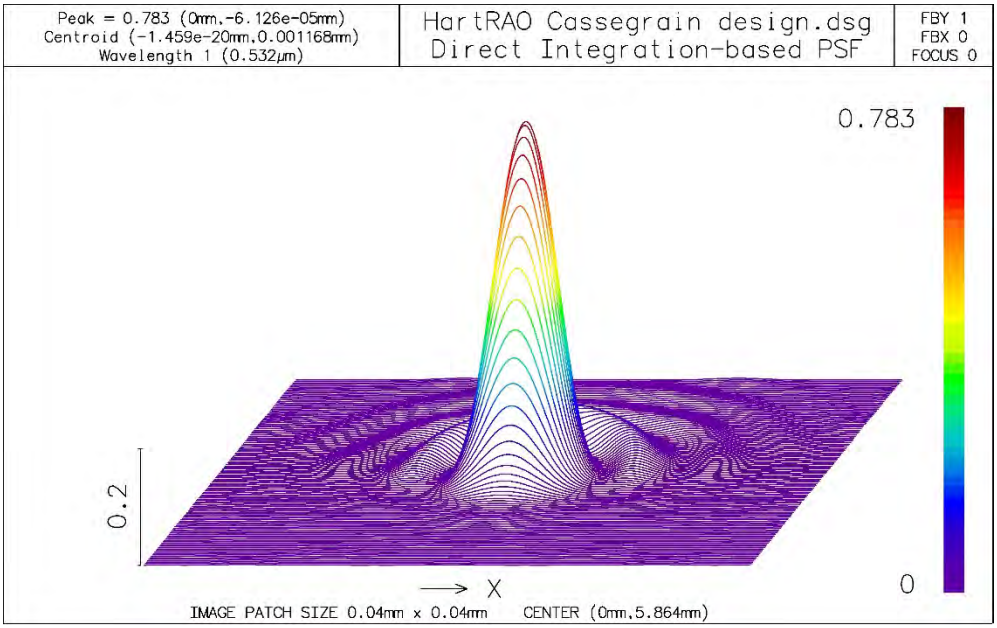

Figure 6-11: Point Spread Function, generated by OSLO, showing a change in intensity distribution when obstructions are removed from the HartRAO LLR telescope for off-axis measurements.

6.4 Transmission efficiency through proposed coudé paths

The total throughput of a telescope is calculated by taking into account the reflectivity of mirrors and the transmission of lenses along the coudé optical path. Reflection measurements were taken for the coudé dielectric mirrors. For the telescope mirrors, measurements used were obtained from Thorlabs for protected aluminium coatings. Transmission measurements were taken for the lenses in the telescope refractor. The refractor is composed of a 76 mm plano-concave lens and a 200 mm achromatic doublet made up of a bi-convex crown and plano-concave flint. The doublet serves to eliminate any chromatic aberrations in the optical system.

Both measurement types were taken under the same acquisition parameters in Ocean Optics Spectrasuite software. An integration time of 3.8 ms was used, averaging 25 scans with boxcar width set to 5. The high average number was used to preserve the resolution of the spectrometer. A non-unity correction was applied on the reflection measurements in order to calibrate the standard/reference used.

6.4.1 Reflectivity measurements

Reflectivity measurements of the dielectric mirrors satisfied the manufacture's specification of approximately 99% reflectivity in the visible spectrum as shown in Figure 6-12. The laser operation range for the LLR is 532 nm, so more emphasis was focussed at measurements at this wavelength. This was compared to a second infrared dielectric mirror which reflected very little

at 532 nm by absorbing approximately 80 percent of the light. Therefore, the visible dielectric mirror is ideal for use in the optical path as it will allow minimal loss of light in each reflection. Figure 6-13 illustrates how they both reflect throughout the visible and infrared parts of the spectrum.

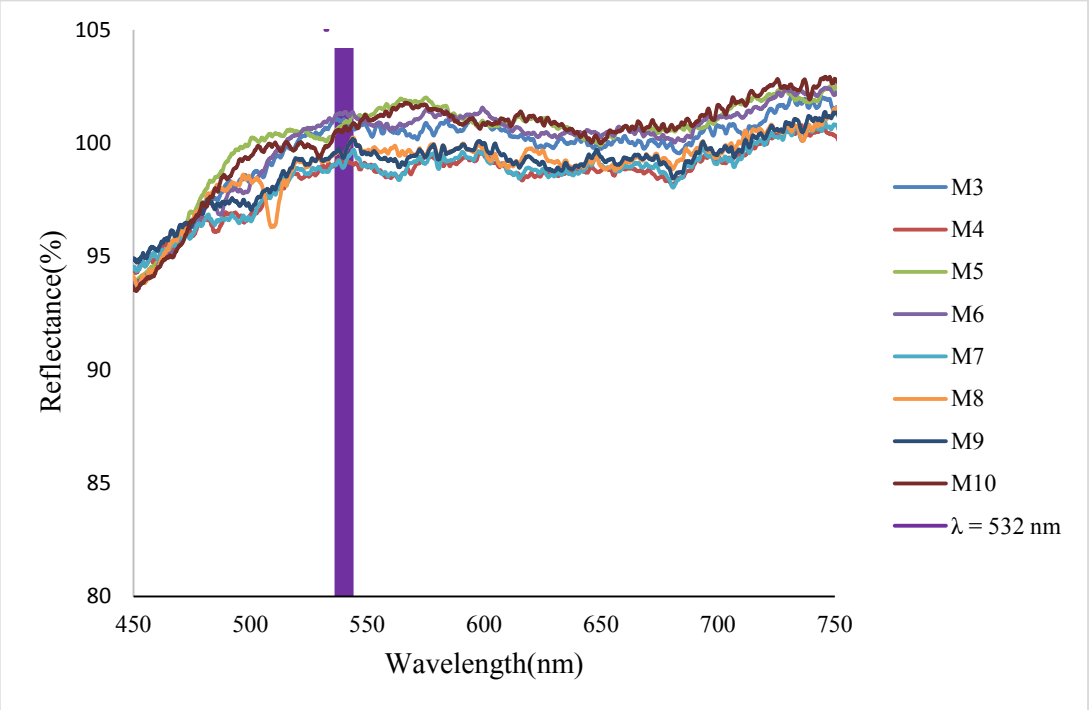

Figure 6-12: Reflection measurements of dielectric mirrors for the HartRAO LLR coudé path. All the mirrors yield at least 98% reflection at a wavelength of 532 nm. The shaded area represents the reflectivity of the mirrors at a wavelength of 532 nm.

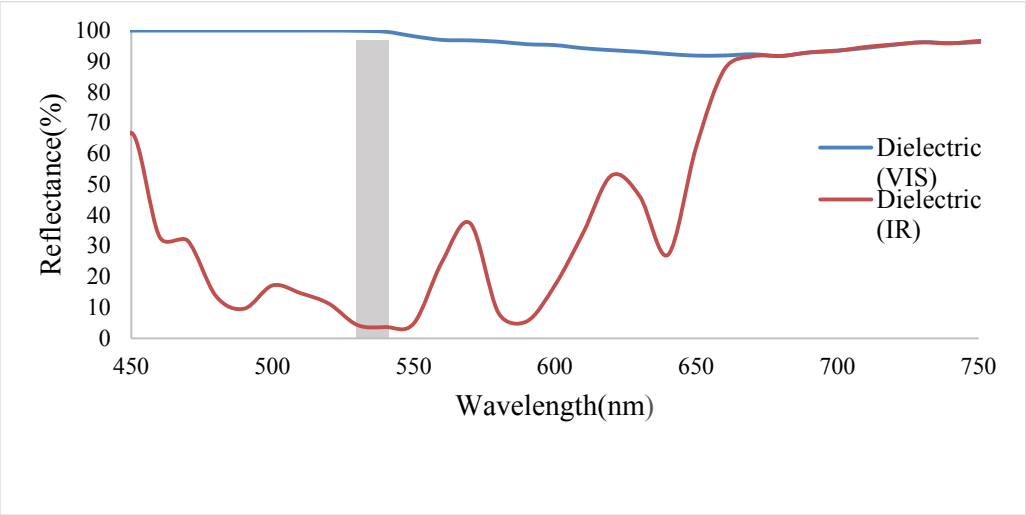

Figure 6-13: Comparison of how visible and infrared dielectric mirrors reflect at different parts of the spectrum.

6.4.2 Transmission Measurements

The collimating lenses had to be focussed before taking any transmission measurements. Keeping the lenses as perfectly still and collimated as possible, the transmission was measured, with air being used as a reference. Figure 6-14 and Figure 6-15 is a representation of the transmission measurements of both lenses.

The transmission efficiencies of the refractor lenses were compared to Thorlabs transmission measurements for the same type of lenses. It was found that the measurements compared well, with errors of approximately 1-2 %. The errors might be due to several factors, including absorption by the glass which was not taken into consideration when obtaining the measurements of our lenses. Generally, losses in coated lenses can be estimated at about 15 % due to reflections with an additional 1 % lost per 2.5 cm aperture.

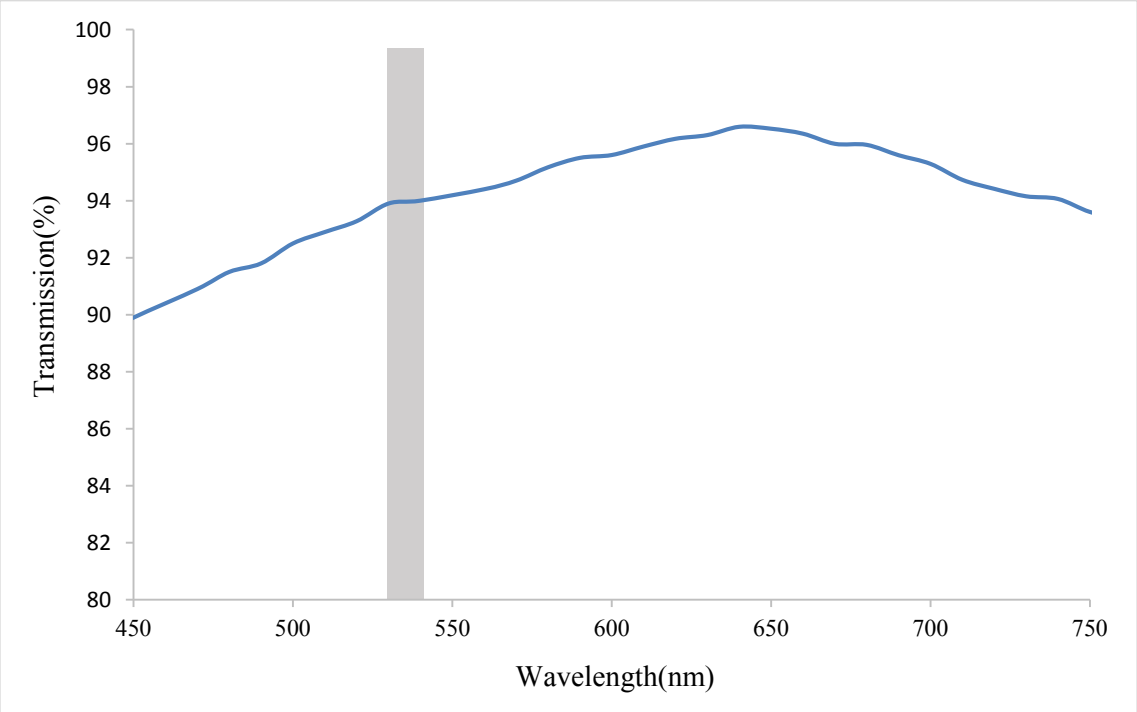

Figure 6-14: Transmission measurement of 76 mm projection lens.

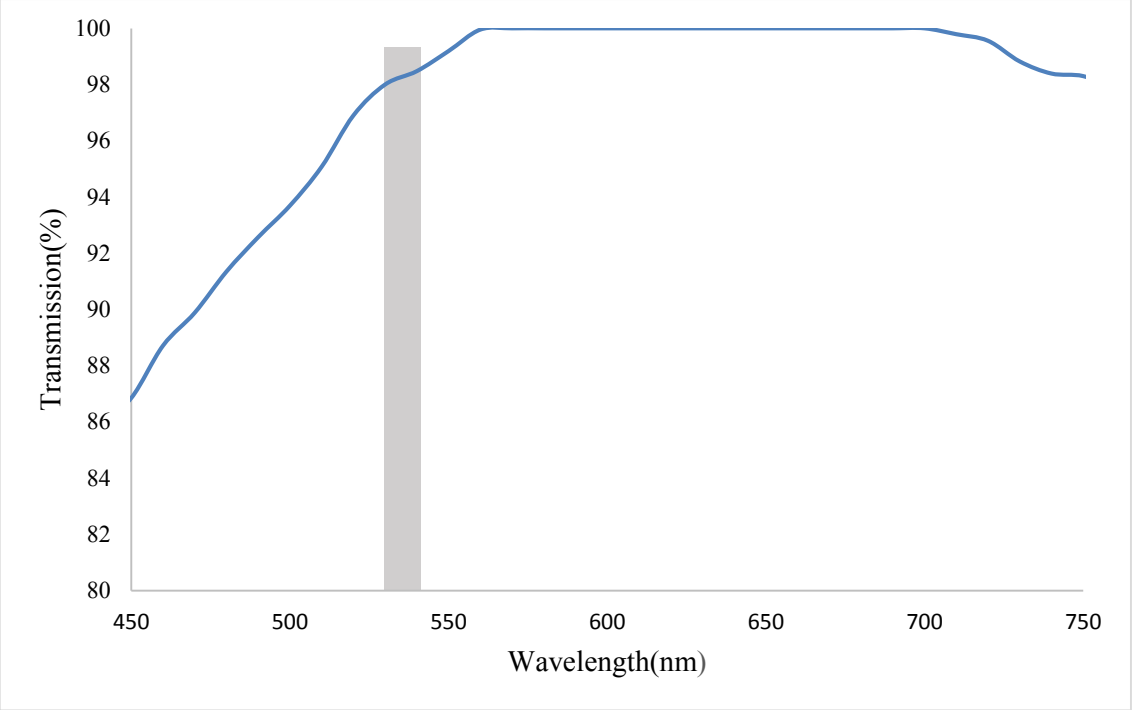

Figure 6-15: Transmission measurement of 200 mm doublet lens.

6.4.3 Telescope throughput

The telescope throughput, also called the system transmission was calculated by taking the product of lens transmissions and all mirror reflections in the transmission optical path. Each path results in different throughputs at different wavelengths. There is no single path that results in a higher throughput across the whole visible spectrum. However, yielding a total transmission of 90 %, path A results in a higher throughput at our operating wavelength of 532 nm as illustrated in Figure 6-16. This might be due to the fact that, even though Path A might have more mirrors, consequently higher reflectance losses, the light lost is still less than the loss from the aluminium coatings of the primary mirrors in Path B, which yields a system transmission of 81 %. Usually loss of light for fresh aluminium coatings is estimated at approximately 10 percent on the visible part of the spectrum. More losses can be expected in path B due to the central obstructions by the secondary mirror. A loss of about 9% was calculated for Path B, resulting in a final transmission efficiency of 71 %.

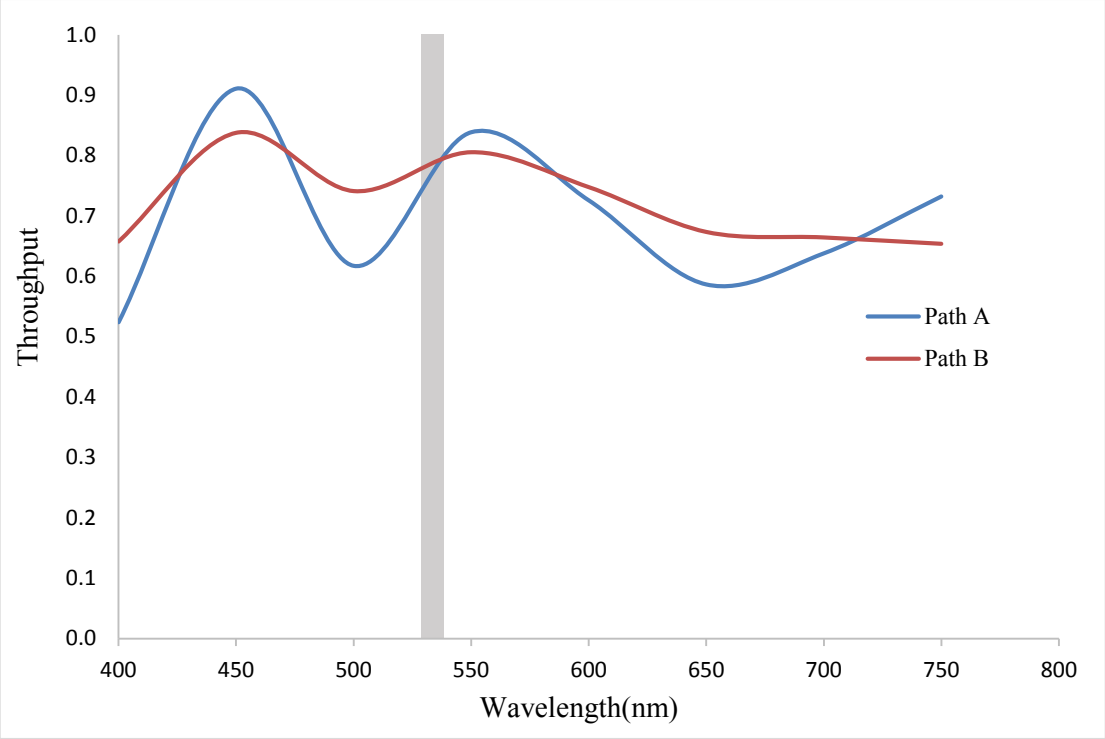

Figure 6-16: Expected throughput of telescope under different transmission paths.

6.5 Modelling and structural analysis of primary mirror

This section presents the Finite Element Analysis (FEA) results of the primary mirror. The analysis was performed on the 1-m diameter honeycomb mirror, with 100 mm thickness made of Zerodur glass ceramic. The mirror deformations were analysed under three different loading conditions, these being when the telescope is pointing at horizon, zenith and at an arbitrary tracking angle measured from zenith. The optical axis of the mirror is in the positive z-axis, while the mechanical elevation corresponds to the positive x-axis. The positive y-axis is defined by the right hand rule. In order to determine the structural efficiency of the mirror geometry, a comparison was made to a solid mirror with the same material properties. A second comparison was made to a honeycomb mirror fabricated from three different materials. From these, an assessment was made on the suitability of Zerodur in minimizing mirror deformations. The mechanical properties of the telescope mirrors are listed in Table 6-1.

6.5.1 Primary Mirror Geometry and mesh

The geometry of the mirror had to be accurately simulated in order to improve the accuracy of the results. The honeycomb structure properties such as the rib height, sheet thickness, and core diameter had to be modelled to the finest detail as these determine the stiffness of the mirror, hence impacts on its self-weight deflection. The honeycomb configuration of the cell geometry is depicted in Figure 6-17.

For highly accurate optics models, a parametric mesh is recommended over automatic meshing. Due to the volumes inside the geometry created by the cells, a hex dominant mesh was applied on the geometry. If the geometry was solid, a sweep mesh would have been the most appropriate method to mesh the radial diameter, however, due to the cells, this disqualifies the geometry from being 'sweepable'. The meshed body is displayed in Figure 6-18.

Table 6-1: Mechanical properties of mirrors of HartRAO LLR telescope.

Parameter	**Primary mirror**	**Secondary mirror**
Diameter	1000 mm	300 mm
Conic constant	-1	- 4.4568
Type	Honeycomb	Honeycomb
Thickness	112 mm	46 mm
Material	Zerodur ceramic glass	Zerodur ceramic glass
Mass	84 kg	12 kg

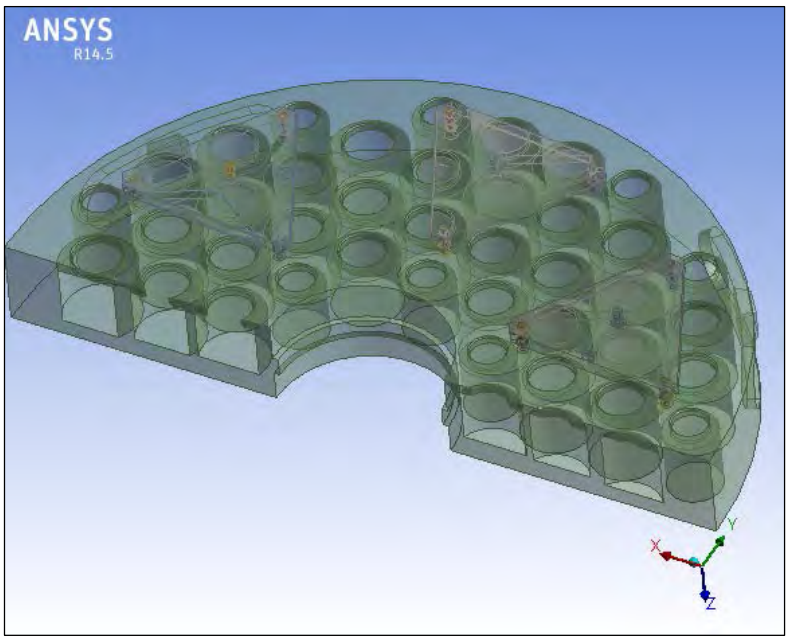

Figure 6-17: Cell configuration of the HartRAO LLR telescope honeycomb mirrors.

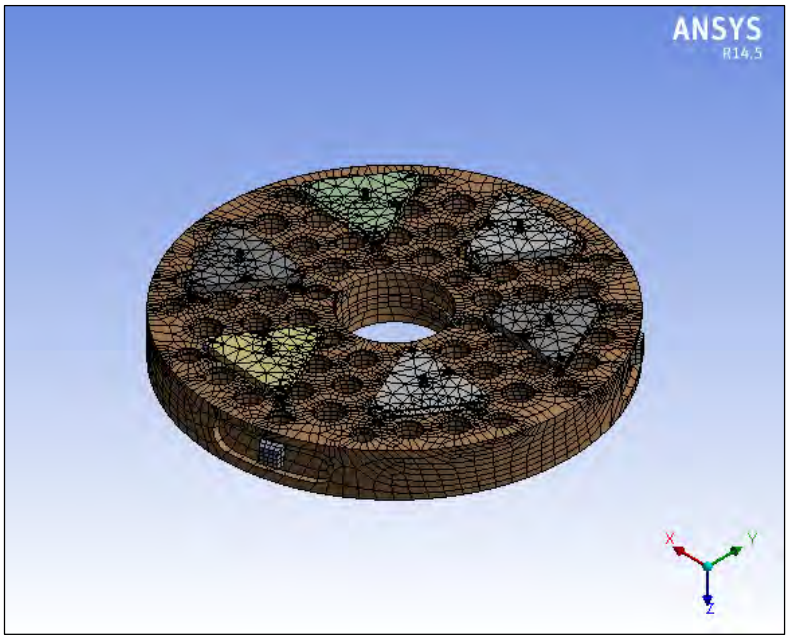

Figure 6-18: Hex dominant mesh of geometry.

6.5.2 Deformation due to axial gravity

When the telescope is pointing at zenith, all the weight of the mirror rests on the supports. The axial support serves to counter the weight of this mass. In order to model the deformations due to axial gravity, a gravity load is applied in the direction normal to the optical axis. All the axial supports were constrained to the mirror.

The load conditions due to axial gravity are as such:

$A_x = 0$ m/s^2

$A_y = 0$ m/s^2

$A_z = -9.8$ m/s^2

The resultant FE model (Figure 6-19) shows a mechanical deformation with a maximum of 95 nm. This is approximately 1/6th of a wavelength. The mirror can be said to be adequately supported as the deformations are well below the expected mechanical deformations for a sandwich structure of that weight. Least deformation occurs on areas not supported by the whiffle-tree support pads. The deformations due to axial gravity are the most important as most deformations are expected to occur along this direction.

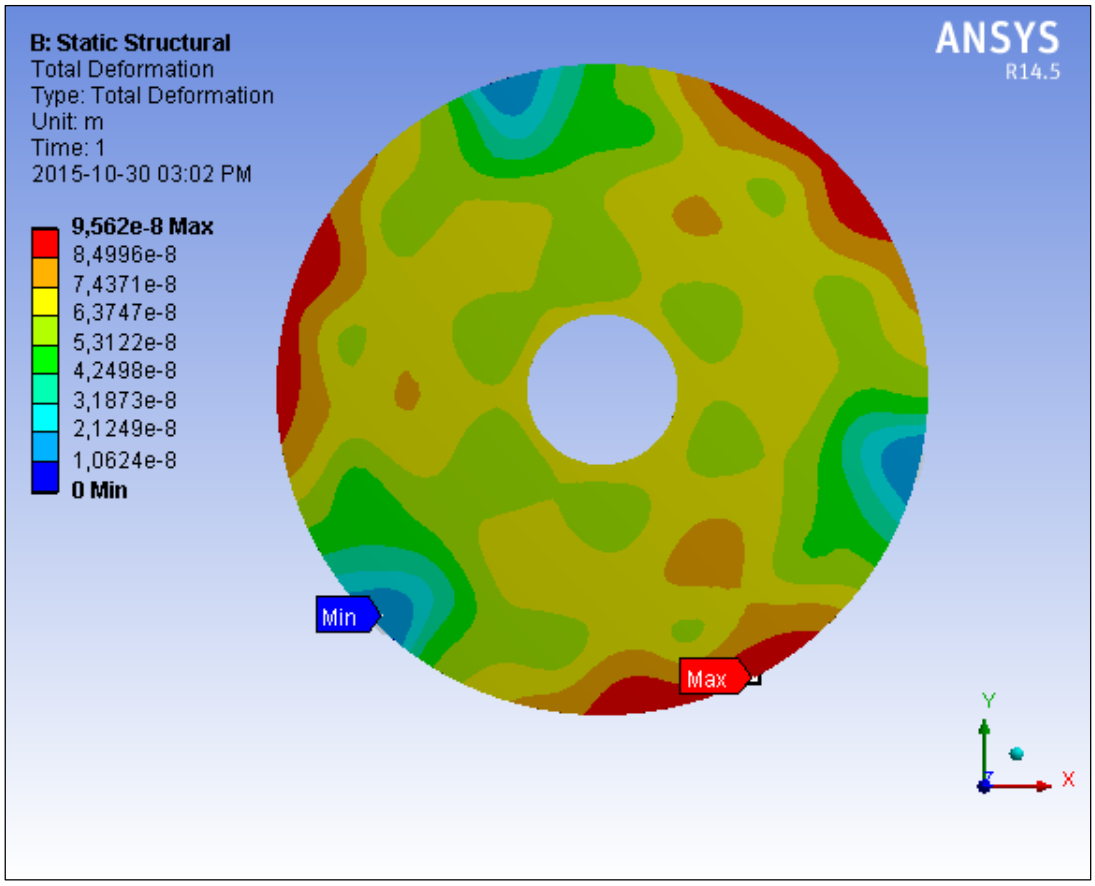

Figure 6-19: FE model of axial gravity deformations on primary mirror, the telescope is pointing at Zenith

6.5.3 Deformation due to lateral gravity

When the telescope is pointing towards the horizon, the lateral supports serve to minimize deformations due to lateral gravity. The lateral supports are spaced 120° from each other radially. The gravity load, in this case, is perpendicular to the optical axis of the mirror. The load conditions are as such:

$A_x = 0\ m/s^2$

$A_y = 9.8\ m/s^2$

$A_z = 0\ m/s^2$

The resultant deformation due to lateral gravity was simulated to be approximately 59 nm. The maximum deformation occurs at the edges of the mirror as seen in Figure 6-20 . Lateral supports are often not taken into great considerations as compared to axial supports due to the fact that surface deformations on the outer edges of the mirror have little effect on image quality.

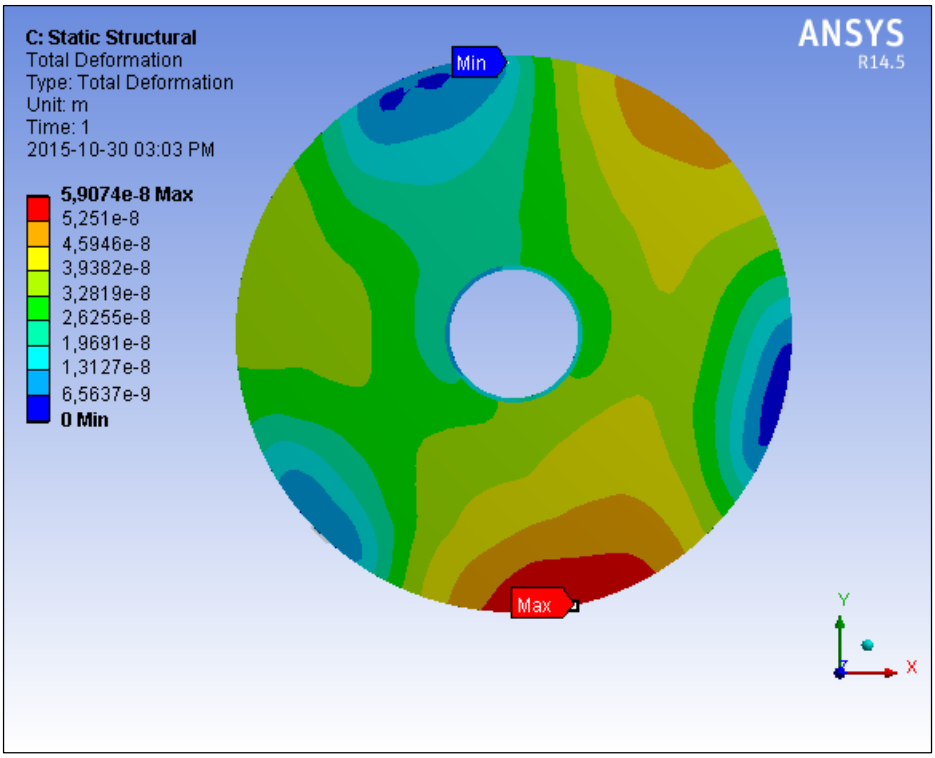

Figure 6-20: Finite element model revealing gravity deformations due to lateral gravity, here the telescope is pointing at the horizon. The positive x-axis corresponds to the telescope's mechanical elevation axis.

6.5.4 Deformation at an angle

A common operating angle range for telescope operations is usually between 0° - 60°. It is therefore necessary to determine the maximum deformation the mirror will experience at this range. The loading conditions at this angle are thus:

$A_x = 0\ m/s^2$

$A_y = g.\sin(60) = 8.495\ m/s^2$

$A_z = g.\cos(60) = -4.909\ m/s^2$

The mirror was constrained on the axial and radial supports along their respective direction of support. The FE model for specified loading condition is shown in Figure 6-21. The maximum mechanical deformation at this angle is 76 nm. This is still significantly below the expected deformation limit of a honeycomb structure of 84 kg. The maximum occurs on the lower edge of the mirror since this where moment forces tend to bend the mirror due to gravity. This is primarily the result of the non-uniform thickness of the concave mirror along its surface.

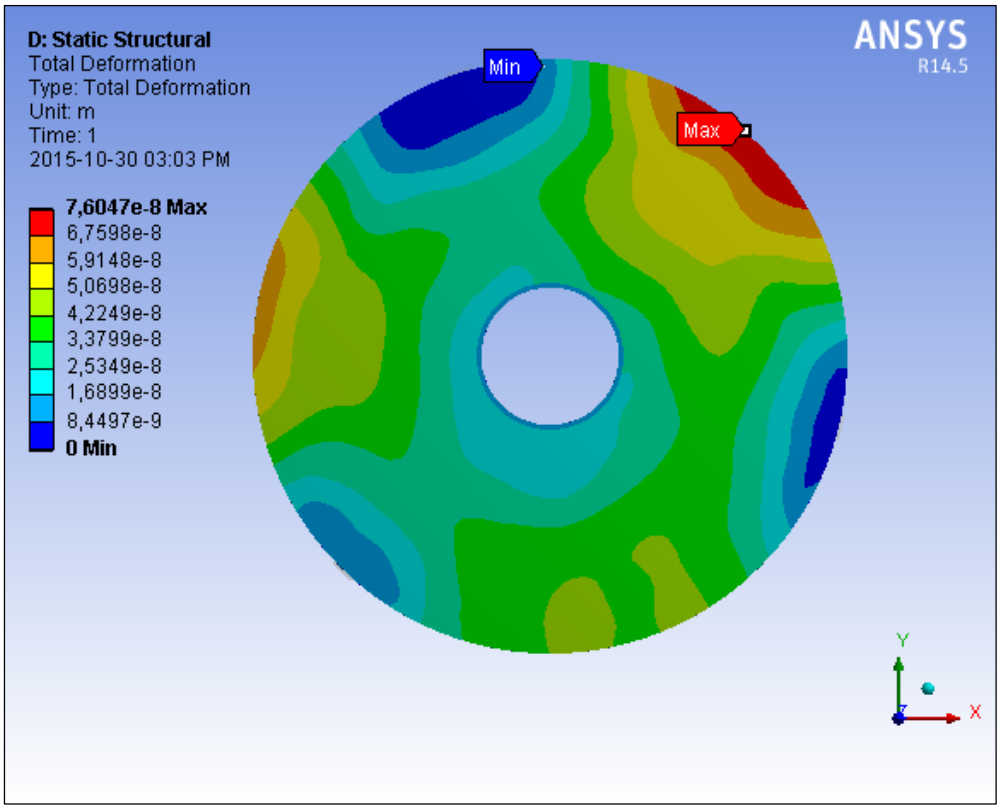

Figure 6-21: Finite element model portraying deformation of primary mirror when telescope is pointing at an angle of 60º.

6.5.5 Comparison to a solid mirror with the same material properties

Unlike lightweight mirrors, solid mirrors are often cost effective in fabrication and relatively easy to support. However, the larger weight induces large mechanical deformations on the mirror. The maximum deformation is approximately 110 nm under axial gravity as seen in Figure 6-22. The maximum deformation occurs on the outer edges of the mirror where the mirror is not sufficiently supported. The least deformation occurs on the axially supported locations on the mirror. The solid mirror introduces over 5 nm more deformations than if the mirror was honeycomb. It is for this reason that a honeycomb lightweight mirror is often the first choice in mirror blanks where structural efficiency is concerned (Valente and Vukobratovich, 1989).

6.5.6 Comparison to other materials with the same honeycomb geometry and same mass

Zerodur is known for its extremely low coefficient of thermal expansions and high chemical stability. In order to evaluate its efficiency when it comes to mechanical strength, a comparison was done with three high quality materials commonly used in mirror design. This comparison is presented in Table 6-2. With a mechanical deformation of 95 nm under axial gravity, Zerodur shows no significant difference mechanically but its low coefficient thermal of expansion will ensure minimal thermal deformations.

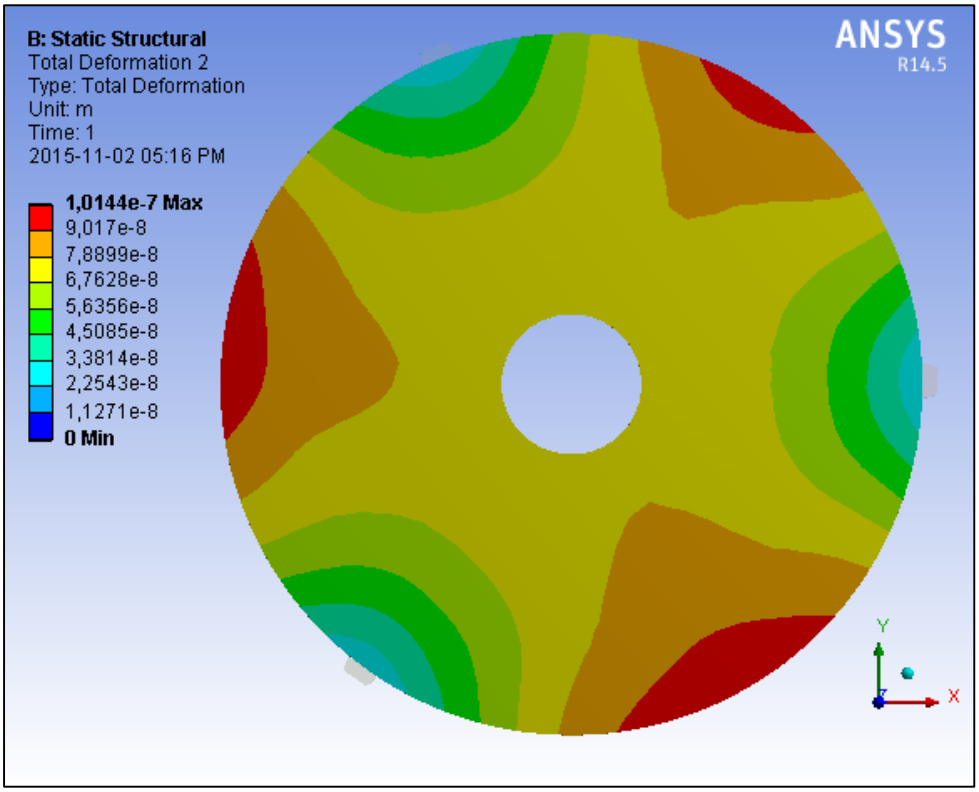

Figure 6-22: Finite element deformation model of a solid mirror made of Zerodur glass ceramic pointing at zenith, under the same whiffle-tree support mechanism.

Table 6-2: Mechanical deformations of honeycomb mirrors made from different materials (Zerodur's maximum mechanical deformation is 95 nm).

Material	**Mass density ($kg/m^{3)}$**	**Young's Modulus (GPa)**	**Poisson's ratio**	**Maximum deformation (nm)**
Pyrex Borosilicate	2230	63	0.2	91
ULE fused silica	2210	67	0.17	84
BK7	2510	82	0.2	79
Zerodur	2530	90	0.24	95

7
CONCLUSION

7.1 Summary

The purpose of the research was to determine and analyse important optical characteristics of the HartRAO Lunar Laser Ranging telescope for efficient optical performance. Optical performance of any telescope highly hinges on the quality of the primary mirror. Its surface accuracy, reflectivity and aperture are all important prerequisites to ensure that a telescope performs optimally, consequently resulting in a high photon return rate during Lunar Laser Ranging. A 'good' telescope is one that can deliver and receive as much light as possible without altering the characteristics of the beam. This is where a good coudé optical path becomes essential. An effective coudé path should consist of highly precise and clean transport optics. The optics should allow minimal loss of light throughout the path and should be able to withstand harsh varying outdoor temperatures. The effectiveness of the optical path is ascertained by the percentage throughput of the optical system. All these aspects were investigated to answer the question: What is the optimal combination of existing and additional optics to enable determination of the characteristics of a laser beam path of the HartRAO Lunar Laser Ranger to the extent that will allow optimum optical performance? All the aims of the research were determined through accurate simulations and calculations. Optical testing is more practical during the manufacture of the telescope and is often costly. Simulations are a suitable option when considering optimization of the system.

7.2 Optical design parameters of HartRAO telescope

In order to maximize the number of photons received when ranging, two things are key: large aperture and good image quality. At a diameter of 1 m, the HartRAO telescope is suitable for both transmitting and receiving light through the same aperture at a high photon return rate under good atmospheric conditions. The telescope can be characterized as moderate in photographic speed as determined by the focal ratio. It is suitable for observing every object in the sky including high power objects such as the Moon. The focal length of the telescope is considered large for a telescope of its diameter. This means that the magnification of the system is strong. This is particularly advantageous in Lunar Laser ranging applications which require high optical performance at a narrower field of view.

The telescope transmission depends immensely on the optics used in the optical path. Highly reflective mirror optics result in high light transmission. Central obscuration was seen to reduce the system transmission by at least 9% of the total light. The system transmission of the

telescope can be as high as 90% if an optical path with no obstructions is considered, but this option is not feasible for Lunar Laser Ranging which requires a large collection area to maximize the number of photons which can be received. The large transmission aperture will mean less beam divergence through the atmosphere, hence resulting in more photons being received. This transmission combined with the large aperture of the telescope increases the light gathering power of the telescope.

7.3 Image quality analysis

In addition to a large and efficient collection area, image quality plays a significant role in optimal Lunar Laser Ranging. The HartRAO telescope was determined to be diffraction limited for on axis performance. The resolution of the telescope was seen to decrease with the field angle of the telescope as determined by its CCD camera. All Cassegrain telescopes are notorious for being coma infected and the HartRAO telescope is no exception as was seen from the spot diagrams. However, this primary aberration was seen to be problematic only for large off-axis performance. The small field angle needed to observe to the Moon at a high resolution means that coma will be kept to a minimum. In some cases, coma can be present in the system if the optics of the telescope are not properly aligned. The additional use of a fast steering mirror can assist in perfectly collimating the system, thereby resulting in near perfect on-axis performance. The Point Spread Function resulted in a Strehl ratio of 0.99 and 0.78 for on-axis and off-axis performance respectively. Even on off-axis performance, the Strehl ratio indicates good optical performance. This implies that optical aberrations will form a very insignificant part of image quality imperfections which might be present in the system.

7.4 Structural analysis

The importance of the surface accuracy of the primary mirror cannot be over emphasized. As the telescope tracks across the sky, the mirror is subjected to gravitational effects which can cause surface deformations of the mirror, hence alter the surface accuracy. Large telescopes highly depend on the support system of the primary mirror. The support serves to counter the effects of gravity on the axial and lateral directions to ensure minimal deformations. The requirement is that these deformations be kept to a small fraction of the wavelength of light that the telescope is designed to use. In the simulations performed, the HartRAO telescope was able to meet these standards.

The honeycomb structure of the primary mirror blank is designed to reduce the weight of the mirror and consequently, increase its structural efficiency. It was seen that the mirror is subjected to most gravitational deformations when gravity acts along the axial support. It is for this reason that the mirror is supported in the axial direction along 18 points while only 3 points support it laterally. Finite element analyses revealed that the mechanical deformations

experienced by the mirror as the telescope moves from the horizon to zenith is significantly less than a quarter of the wavelength, at $\lambda = 532$ nm. This is evidence that the telescope is adequately supported to limit gravity induced deformations. This is indicative of the capability of the support system to maintain the nominal surface figure accuracy of the mirror to an acceptable limit that will not greatly affect the image quality of the telescope as a whole.

The task of Lunar Laser Ranging is one that requires a collaborative combination of its subsystems. The optical performance of the telescope is one part of this whole process, but the success of other subsystems would be deemed useless without a good quality telescope to successfully consummate the job. Taking into consideration the high system transmission of the telescope, the effective delivery system of the coudé path, adequate structural efficiency of the primary mirror system as well as the diffraction-limited performance of the system, the HartRAO telescope is capable of accomplishing its desired task of ranging to the Moon at high accuracy.

7.5 Future work and recommendations

Finite Element Analysis software expresses results in the form of mechanical displacements the structure experiences at arbitrary FE mesh nodes. Optical analyses are often expressed either in Peak-to-Valley (P-V) or RMS wavefront errors. This is statistically averaged deviations of the wavefront. In order to calculate the wavefront error from the FEM analysis data, post-processing software is required to fit Zernike polynomials on the data which can be understood by optical analysis software. Zernike polynomials express wavefront data in polynomial form for the interpretation of optical figure tests. The polynomials are similar to the types of aberrations often observed in optical tests. This further post-process could not be carried out in this work due to the expensive nature of software used to covert Finite Element Analysis data into Zernike polynomials for input into optical analysis software. As the LLR system is still under development, many optical tests could not be performed such as star calibrations and optical path length variations (LLR system delay stability). These and other avenues of investigation could form part of a more in-depth project, possibly part of a PhD study.

REFERENCES

1. Abdulkadyrov, M., Patrikeev, A., Belousov, S., Pridnya, V., Patrikeev, V., Ignatov, A., Polyanchikov, A., Semenov, A. and Sharov, Y. (2008). M2 secondary mirror manufacturing for VISTA project. In: *Advanced Optical and Mechanical Technologies in Telescopes and Instrumentation*. Proc. SPIE.

2. Allen, L., Angel, R., Mangus, J., Rodney, G., Shannon, R. and Spoelhof, C. (1990). *The Hubble Space Telescope Optical Systems Failure Report*. NASA.

3. Andersen, G. (2007). *The telescope*. Princeton, NJ: Princeton University Press.

4. Andersen, T. and Enmark, A. (2011). *Integrated modeling of telescopes*. New York: Springer Science+Business Media, LLC, pp. 92-101.

5. Angeli, G., Segurson, A., Upton, R., Gregory, B. and Cho, M. (2004). Integrated modeling tools for large ground based optical telescopes. SPIE, 5178, pp.49-62.

6. Beckers, J., Ulich, B., Shannon, R., Carleton, N., Geary, J., Latham, D., Angel, R., Hoflmann, W., Low, F., Weymann, R. and Woolf, N. (1981). *Telescopes for The 1980s.*[online] Mmto.org. Available at: http://www.mmto.org/node/442 [Accessed 3 Aug. 2012].

7. Bely, P. (2003). *The design and construction of large optical telescopes*. New York: Springer

8. Bender, P., Currie, D., Poultney, S., Alley, C., Dicke, R., Wilkinson, D., Eckhardt, D., Faller, J., Kaula, W., Mulholland, J., Plotkin, H., Silverberg, E. and Williams, J. (1973). The Lunar Laser Ranging Experiment: Accurate ranges have given a large improvement in the lunar orbit and new selenophysical information. *Science*, 182(4109), pp.229-238.

9. Bitzer, T. (1997). *Honeycomb Technology: Materials, Design, Manufacturing, Applications and Testing*. London, UK: Chapman and Hall, pp.11-15.

10. Born, M. and Wolf, E. (1999). *Principles of optics*. Cambridge: Cambridge University Press, pp.412-514.

11. Brown, D. (1979). The Prediction of On Site Telescope Performance. *The messenger*, 19(16).Cho, M. (2001). *Conceptual Design of Primary Mirror Segment Support System of the GSMT Point Design*. NOAO.

12. Burge, J. (1995). Measurement of a convex secondary mirror using a holographic test plate. In: *International Conference on Optical Fabrication and Testing*. Proc. SPIE.

13. Burge, J. (1997). Measurement of large convex aspheres. *Optical Telescopes of Today and Tomorrow*, 2871(362), pp.362-373.

14. Burge, J., Anderson, B., Benjamin, S., Cho, M., Smith, K. and Valente, M. (2001). Development of optimal grinding and polishing tools for aspheric surfaces. In: *Optical Manufacturing and Testing IV*. Proc. SPIE.

15. Burge, J., Anderson, D., Milster, T. and Vernold, C. (1994). Measurement of a convex secondary mirror using a holographic test plate. In: *Advanced Technology Optical Telescopes V*. Proc. SPIE.

16. Burge, J., Dettmann, L. and West, S. (1999). Null correctors for 6.5-m f/1.25 paraboloidal mirrors. In: *Fabrication and Testing of Aspheres*. OSA Trends in Optics and Photonics (Optical Society of America.

17. Burge, J., Kot, L., Martin, H., Zhao, C. and Zobrist, T. (2006). Alternate surface measurements for GMT primary mirror segments. In: *Optomechanical Technologies for Astronomy*. Proc. SPIE.

18. Center for Space Research, University of Texas., (2015). *McDonald Laser Ranging System*. [online] Csr.utexas.edu. Available at: http://www.csr.utexas.edu/mlrs/ [Accessed 12 Jun. 2012].

19. Cheng, J. (2009). *The principles of astronomical telescope design*. New York: Springer, pp.87-139

20. Ceravolo, P. (2003). *Using The Ross Null Test*. [online] Available at: http://www.ceravolo.com/testing/ross_null.pdf [Accessed 8 Apr. 2015].

21. Combrinck, L. (2005). *Proposed re-location and conversion of CNES SLR system to South Africa in collaboration with OCA and the greater ILRS community*. [online] Hartrao.ac.za. Available at: http://www.hartrao.ac.za/iisgeo/docs/LLR_proposal.doc [Accessed 15 Jul. 2012].

22. Combrinck, L. (2011). Development of a satellite and lunar laser ranger and its future applications in South Africa. In: *62nd International Astronautical Congress*. Cape Town: International Astronautical Federation.

23. Combrinck, L. (2012). Progress on the development of a satellite and lunar laser ranger in South Africa. In: *theory and model for the new generation of the lunar laser ranging data*. Bern: ISSI.

24. Degnan, J. (1993). Millimeter Accuracy Satellite Laser Ranging: a Review. *Contributions of Space Geodesy to Geodynamics: Geodynamics Series*, 25, pp.133-162.

25. Dierickx, P. (1992). Optical Performance of Large Ground-based Telescopes. Journal of Modern Optics, 39(3), pp.569-588.

26. Ding, L., Wu, Y., Li, S., Liao, Y. and Shu, Y. (2010). Phase retrieval in situ measurement for large aperture parabolic mirror. In: *5th International Symposium on Advanced Optical Manufacturing and Testing Technologies: Optical Test and Measurement Technology and Equipment*. Proc. SPIE.

27. Döhring, T., Hartmann, P., Jedamzik, R., Thomas, A. and Lentes, F. (2006). Properties of Zerodur Mirror Blanks for Extremely Large Telescopes. *SPIE*, 6148.

28. Döhring, T., Jedamzik, R., Thomas, A. and Hartmann, P. (2008). Forty Years of Zerodur Mirror Substrates for Astronomy: review and outlook. In: *Advanced Optical and Mechanical Technologies in Telescopes and Instrumentation*. SPIE

29. Fischer, R., Tadic-Galeb, B. and Yoder, P. (2008). *Optical System Design*. New York: McGraw-Hill.

30. Focke, J. (1965). Higher Order Aberration Theory. In: E. Wolf, ed., *Progress in Optics*, 1st ed. North Hollard, Amsterdam: Elsevier, pp.1-36.

31. Geary, J. (1993). *Introduction to Optical Testing*. Bellingham, Wash., USA: SPIE Optical Engineering Press, pp.25-49.

32. Genberg, V. (1996). Structural Analysis of Optics. In: A. Ahmad, ed., *Handbook of Optomechanical Engineering*, 1st ed. New York: CRC Press, p.255.

33. Greivenkamp, J. (2004). *Field Guide to Geometrical Optics*. Bellingham, Wash.: SPIE Press, pp.70-83.

34. Hecht, E. (2002). *Optics*. Reading, Mass.: Addison-Wesley, pp.253-268.

35. Hindle, J. (1931). A New Test for Cassegrainian and Gregorian Secondary Mirrors: (Plate 11.). *Monthly Notices of the Royal Astronomical Society*, 91(5), pp.592-593.

36. Hoeness, H., Mueller, R., Rodeck, E. and Siebers, F. (1989). Spin-cast ZERODUR Mirror Substrates of the 8 m Class and Lightweight Substrates for Secondary Mirrors. *Astrophysics and Space Science*, 160(1-2), pp.193-197.

37. Howard, J., Beaulieu, M. and Zielinski, R. (1983). A Non-obscuring, Easily-Calibrated Method for Testing Ellipsoids and Hyperboloids on a Fizeau Interferometer. In: *Optical Systems Engineering III*. Proc. SPIE.

38. Jiang, Z., Li, X. and Ji, B. (2012). Development of Testing Convex Hyperbolic Mirror using Hindle Method based on Stitching Technology. In: *Modern Technologies in Space- and Ground-based Telescopes and Instrumentation II*. Proc. SPIE 8450.

39. Keel, A. (2009). *Finite Element Analysis of Deformations and Applied Forces and Constraints in the 81-inch Primary Mirror of the TSU 2-m Telescope*. [online] Coe.tsuniv.edu. Available at: http://coe.tsuniv.edu/eaton/keel/fea_keel.htm [Accessed 16 Jul. 2014].

40. King, H. (1955). *The History of the Telescope*. Cambridge, Mass.: Sky Publishing Corp., p.75.

41. Korhonen, T., Keinanen, P., Pasanen, M. and Sillanpaa, A. (2008). Polishing and Testing of the 1.5 m SiC M1 Mirror of the ALADIN Instrument on the ADM-Aeolus Satellite of ESA. In: *Optical Fabrication, Testing, and Metrology III*. Proc. SPIE 7102.

42. Korhonen, T., Lappalainen, T. and Sillanpaa, A. (1991). Hartmann Interferometric Testing of Large Mirrors. In: *Advanced Optical Manufacturing and Testing II*. Proc. SPIE 1531.

43. Kugler, T. (2009). *Advanced Solutions for Laser Beam Delivery*.

44. Li, J., Xuan, B. and Sun, Y. (2012). Hindle test of SiC Convex Conic Hyperboloid. In: *6th International Symposium on Advanced Optical Manufacturing and Testing Technologies: Optical Test and Measurement Technology and Equipment*. Proc. SPIE 8417.

45. Li, Y. (2012). Modeling and Structural Analysis of Honeycomb Structure Mirror. In:

Modern Technologies in Space- and Ground-based Telescopes and Instrumentation II. Proc. SPIE

46. Lockwood, M. (2015). [online] Available at: http://Casseghttp://www.loptics.com/ATM/mirror_making/cass_info/cass_info.html [Accessed 26 Oct. 2014].

47. Lytle, J. (1970). A Suggested Procedure for Testing Large Cassegrainian Optical Systems. *Applied Optics*, 9(11), p.2497.

48. Madenci, E. and Guven, I. (2006). *The Finite Element Method and Applications in Engineering using ANSYS*. New York: Springer.

49. Mahajan, V. (1983). Strehl Ratio for Primary Aberrations in Terms of their Aberration Variance. J. Opt. Soc. Am., 73(6), p.860.

50. Malacara, D. (1978). *Optical Shop Testing*. New York: Wiley.

51. Malacara, D. and Malacara, Z. (2004). *Handbook of Optical Design, 2nd edtion*. New York: Marcel Dekker.

52. Malacara, D. (2007). *Optical Shop Testing*. Hoboken, N.J.: Wiley-Inter-science.

53. Martin, H., Burge, J., Cuerden, B., Miller, S., Smith, B. and Zhao, C. (2004). Manufacture of 8.4-m off-axis segments: a 1/5-scale demonstration. In: *Optical Fabrication, Metrology, and Material Advancements for Telescopes*. Proc. SPIE 5494.

54. McKechnie, T. (2010). Interferometric Test Method for Testing Convex Aspheric Mirror Surfaces. In: *Modern Technologies in Space- and Ground-based Telescopes and Instrumentation*. Proc. SPIE 7739.

55. McKechnie, T. (2012). *Test Method for Surface Figure of Large Convex Mirrors*. US 8089633 B2.

56. Merkowitz, S. (2010). *NASA Technical Reports Server (NTRS)*. [online]Ntrs.nasa.gov. Available at: http://ntrs.nasa.gov/archive/nasa/casi.ntrs.nasa.gov/20100015399.pd [Accessed 13 Jul. 2012].

57. Merrill, M. (2009). *Happy Living - How to test your telescope's optics*. [online] Happynews.com. Available at: http://www.happynews.com/living/space/test-telescopes-optics.htm [Accessed 5 May 2012].

58. Moaveni, S. (1999). *Finite Element Analysis*. Upper Saddle River, N.J.: Prentice Hall.

59. Morison, I. (2009). *Star Testing a Telescope*. [online] Society for popular astronomy. Available at: http://popastro.com/documents/PA_janmar2009_p1213_telescopetopics_startesting.pdf [Accessed 2 May 2013].

60. Murphy, T., Adelberger, E., Battat, J., Carey, L., Hoyle, C., LeBlanc, P., Michelsen, E., Nordtvedt, K., Orin, A., Strasburg, J., Stubbs, C., Swanson, H. and Williams, E. (2008). The Apache Point Observatory Lunar Laser-ranging Operation: Instrument Description and First Detections. *Publications of the Astronomical Society of the Pacific*, 120(863), pp.20-37.

61. Napier-Munn, T. (2008). A Mathematical Model to Predict the Resolution of Double Stars by Amateurs and their Telescopes. *Journal of Double Star Observations*, 4(4), pp.156-163.

62. Navarro, R. and Moreno-Barriuso, E. (1999). Laser Ray-tracing Method for Optical Testing. *Opt. Lett.*, 24(14), p.951.

63. Ned.ipac.caltech.edu, (2005). Astronomical Glossary. [online] Available at: http://ned.ipac.caltech.edu/level5/Glossary/Glossary_S.html [Accessed 20 Sep. 2013].

64. Nickola, M. (2012). Astronomical Seeing Conditions as Determined by Turbulence Modelling and Optical Measurement. Masters. University of Pretoria.

65. O'Donoghue, D., Atad-Ettedgui, E., Balona, L., Bigelow, B., Booth, J., Botha, L., Buckley, D., Brink, J., Charles, P., Clemens, J. and Christians, A. (2008). The image quality of the Southern African Large Telescope (SALT). In: *Advanced Optical and Mechanical Technologies in Telescopes and Instrumentation*. Proc. SPIE 7018.

66. O'Shea, D. and Harrigan, M. (1995). Aberration curves in lens design. In: M. Bass, ed., *Handbook of optics*, 2nd ed. New York: McGraw-Hill, Chapter 33.

67. Ocean Optics, (2009). *Spectrasuite spectrometer Operating software*. Dunedin, FL: A Halma group company, pp.148, 150.

68. Optics.synopsys.com, (2015). Synopsys Optical Solutions Group. [online] Available at: http://optics.synopsys.com/#SpotDiagrams [Accessed 26 Jun. 2015].

69. Palunas, P., MacQueen, P., Booth, J., Calder, R., Fowler, J., Shetrone, M., Odewahn,

S., Segura, P., Wesley, G., Damm, G., Martin, J. and Odoms, P. (2006). Imaging Performance of the Hobby-Eberly Telescope. Ground-based and Airborne Telescopes. In: *Ground-based and Airborne Telescopes*. Proc. SPIE 6267.

70. Paquin, R. (1999). Materials for Optical Systems. In: A. Ahmad, ed., *Opto-mechanical Engineering Handbook*, 3rd ed. Boca Raton: CRC Press.

71. Parks, R. and Shao, L. (1988). Testing large hyperbolic secondary mirrors. *Optical Engineering*, 27(12).

72. Porter, A. (1990). Hartmann Testing with a CCD. In: *CCDs in Astronomy*. A.S.P. Conf.

73. Pradeep Kumar, K., Maruthi, B. and Krishnamurthy, T. (2013). Design and Analysis of Three Axis Gimbal Mount for testing a Large Size Light Weight Mirror of a Space Borne Telescopic Optics. *International journal of research in aeronautical and mechanical engineering*, 1(4), pp.16-36

74. Ridpath, I. (1997). *A dictionary of astronomy*. Oxford: Oxford University Press, p.453.

75. Robbert, C., Yoder, Jr., P. and Montagnino, L. (1979). A Typical Error Budget for Testing High-Performance Aspheric Telescope Mirror. In: *Contemporary Optical Systems and Components Specifications*. Proc. SPIE 0181.

76. Roddier, C. and Roddier, F. (1993). Wave-front Reconstruction from Defocused Images and the Testing of Ground-based Optical Telescopes. *J. Opt. Soc. Am. A*, 10(11), p.2277.

77. Sacek, V. (2006). *Amateur Telescope Optics*. [online] Telescope-optics.net. Available at: http://www.telescope-optics.net/ [Accessed 10 Jul. 2015].

78. Samain, E., Mangin, J., Veillet, C., Torre, J., Fridelance, P., Chabaudie, J., Fïraudy, D., Glentzlin, M., Pham Van, J., Furia, M., Journet, A. and Vigouroux, G. (1998). Millimetric Lunar Laser Ranging at OCA (Observatoire de la Cote d'Azur). *Astronomy and Astrophysics Supplement Series*, 130(2), pp.235-244.

79. Schott, (2011). *Zerodur® Zero Expansion Glass Ceramic*. mainz: SCHOTT AG.

80. Schroeder, D. (1987). *Astronomical optics*. San Diego: Academic Press.

81. Simpson, F., Orland, B. and Michel, J. (1974). Testing Convex Aspheric Lens Surfaces with a Modified Hindle. Arrangement. *Optical Engineering*, 13, p.101

82. Schleuter. W., Soltau, G., Dassing, R. and Hopfl, R. (1984). The Concept of a new Wettzell Laser Ranging System with dual capability. In: *5th International Workshop on Laser Ranging Instrumentation*. International Laser Ranging Service.

83. Shannon, R. (1997). *The art and science of optical design*. Cambridge, U.K.: Cambridge University Press, pp.553-566.

84. Smith, W. (2000). *Modern optical engineering*. 3rd ed. New York: McGraw-Hill.

85. Structural analysis in the design of optical mirrors. (2015). [online] Available at: http://oce.jpl.nasa.gov/practices/2305.pdf [Accessed 28 Feb. 2015].

86. Suiter, H. (1994). *Star testing astronomical telescopes*. Richmond, Va., USA: Willmann-Bell.

87. Telescope-optics.net, (2015). *Main functions of a telescope*. [online] Available at: http://www.telescope-optics.net/functions.htm [Accessed 12 Jun. 2014].

88. Texereau, J. (1957). *How to make a telescope*. New York: Inter-science Publishers.

89. Tiziani, H., Reichelt, S., Pruss, C., Rocktaeschel, M. and Hofbauer, U. (2001). Testing of aspheric surfaces. In: *Lithographic and Micromachining Techniques for Optical Component Fabrication*. Proc. SPIE 4440.

90. Turyshev, S. (2009). *From quantum to cosmos*. Singapore: World Scientific.

91. Vukobratovich, D. (1997). Opto-mechanical Design Principles. In: A. Ahmad, ed., *Handbook of Opto-mechanical Design*, 1st ed. Boca Raton: CRC Press LLC, p.Chapter 2.

92. Vukobratovich, D. (2007). Lightweight mirror design. In: A. Ahmad, ed., *Handbook of Opto-mechanical Engineering*, 1st ed. New York: CRC Press, pp.125-148.

93. Vukobratovich, D. and Vukobratovich, S. (2008). *Introduction to Opto-mechanical Design*.

94. Williams, J. and Dickey, J. (2002). Lunar Geophysics, Geodesy, and Dynamics. In: *13th International Workshop on Laser Ranging*. Washington, D. C.

95. Williams, J., Turyshev, S., Baran, R., Birnbaum, K., Currie, D., Folkner, W. and Gutt, G. (2007). *Lunar Science and Lunar Laser Ranging*. The National Academies Planetary

Science Decadal Survey.

96. Wilson, R. (1976). The ESO Optics Group and some Recent Achievements. *Messenger*, 6(5).

97. Wodaski, R. (2002). *The new CCD astronomy*. Duvall, WA: New Astronomy Press, pp.166-174.

98. Wyant, J. and Bennett, V. (1972). Using Computer Generated Holograms to Test Aspheric Wavefronts. *Applied Optics*, 11(12), p.2833.

99. Wyant, J. and Creath, K. (1992). Basic Wavefront Aberration Theory for Optical Metrology. *Applied Optics and Optical Engineering*, 6, pp.1-53.

100. Wyant, (1992). Optical Systems Technology for Space Astrophysics. In: *Integrated technology planning*. NASA, pp.1-7.

101. Yang, H., Song, J., Lee, Y., Lee, H., Lee, J. and Lee, I. (2005). Real-time measurement of the small aspheric surface. In: *Optical Manufacturing and Testing VI*. Proc. SPIE 5869.

102. Yoder, P. (2005). *Opto-Mechanical Systems Design*. Hoboken: CRC Press.

103. Yoder, P. (2006). *Opto-mechanical systems design*. Bellingham, Wash.: SPIE Press

104. Yong-soo, K. (2001). Developing an Optical Testing Method for Space Telescopes. *Journal of the Optical Society of Korea*, 5(3), pp.70-75.

105. Zhao, C., Burge, J., Zehnder, R. and Martin, H. (2005). Testing an off-axis parabola with a CGH and a spherical mirror as null lens. In: *Optical Manufacturing and Testing VI*. Proc. SPIE 5869.